Multiferroicity In Bismuth Layer Structured Materials

Zheng Li

A thesis submitted for the degree of Doctor of Philosophy

School of Engineering and Materials Science,

Queen Mary, University of London,

London, UK

September 2016

Declaration

The candidate confirms that the research included within this thesis is my own work or that where it has been carried out in collaboration with, or supported by others. The work of other people is duly acknowledged below and my contribution indicated.

This thesis fully complies with the regulations set by the Queen Mary, University of London.

Abstract

Multiferroics (MF) have attracted much research attention due to the coexistence of ferroelectric and magnetic ordering as well as magnetoelectric (ME) coupling. At present there are very few room temperature single phase MF except $BiFeO_3$. Multiferroic properties of Aurivillius compound $Bi_5FeTi_3O_{15}$ were reported at 80 K. The magnetization of $Bi_5FeTi_3O_{15}$ was significantly improved by substituting parts of Fe cations by Co cations. $Bi_5FeTi_3O_{15}$ showed ferromagnetic order above room temperature. The magnetic cations Fe/Co in B-site contribute to the both ferroelectric and ferromagnetic properties, which could possibly induce strong magnetoelectric effect. Aurivillius materials are layered structured materials with formula $(Bi_2O_2)^{2+}(A_{m-1}B_mO_{3m+1})^{2-}$. The polarization of Aurivillius materials is mainly in *a-b* plane. High dense and textured ceramics were fabricated by a two-step spark plasma sintering (SPS) method to improve the polarization of ceramics. The multiferroic properties of Aurivillius materials with different octahedral layers (m=2, 3, 4 and 5) were investigated. All these materials showed ferroelectric and ferromagnetic order at room temperature except $Bi_3Nb_{1.125}Fe_{0.125}Co_{0.125}Ti_{0.75}O_9$ (m = 2). $Bi_{3.25}La_{0.75}Nb_{0.25}Fe_{0.125}Co_{0.125}Ti_{2.5}O_{12}$ (m = 3) was identified to be single phase. Although a small amount of secondary phases ($CoFe_2O_4$/Co_2FeO_4) were found in $Bi_{4.25}La_{0.75}Fe_{0.5}Co_{0.5}Ti_3O_{15}$ (m = 4) and $Bi_{5.25}La_{0.75}FeCoTi_3O_{18}$ (m = 5), the intrinsic multiferroicity of the main Aurivillius phase was confirmed by the magnetic controlled ferroelectric domain switching. Clear ME couplings were observed in these materials,

where the magnetic ions Fe/Co contribute to ferroelectric polarization and magnetic moment simultaneously. This discovery could guide the design of room temperature single phase MFs with strong ME coupling for sensors and memories applications.

Acknowledgement

First of all, I would like to thank my supervisor Dr. Haixue Yan for his great knowledge, patience and guidance during my PhD studies. His patient guidance enabled me to be an independent researcher in an unfamiliar field. I would also like to thank Prof. Mike John Reece, my secondary supervisor. He provides very helpful convenience for my experiments.

I would also thank to Dr. Qinghui Jiang, Dr. Zhipeng Gao, Dr. ChenChen, Dr. Vladimir Koval, Dr. Amit Mahajan and Dr. Giuseppe Viola for their discussions and help with my experiments and Papers.

I am appreciating Dr. Isaac Abrahams and Dr. Rory Wilson for their help with the XRD experiments and XRD Rietveld refinement.

I would to thank Prof. Chenglong Jia and Prof. Cewen Nan for the guidance of the study of magnetic physics and performing of the first principle modelling.

I am also very grateful to the help provided by members of our ceramics group: Dr. Salvatore Grasso, Dr. Ruth Mckinnon, Kan Chen, Chuying Yu, Hangfeng Zhang, Nan Meng and Xiaojing Zhu.

Lastly, I would like to thank my parents for their supporting and encourages in these four years.

Notation

T_c Curie temperature

T_N Neel temperature

T_f Freezing temperature

μ_B Bohr magneton

E Electric field

P Polarization

P_s Spontaneous polarization

P_r remanent polarization

Δx_i atomic displacement

V volume of the unit cell

t tolerance factor

d_{33} vertical piezoelectric constant

ω_0 attempt angular frequency of the dipoles

T_0 equivalent temperature of activation energy

k Boltzmann`s constant

P_l orbital angular momentum

δ_s spin angular moment

μ_0 vacuum permeability

μ_l orbital magnetic moment

μ_s spin angular momentum

i	*current*
e	electron charge
l	orbital magnetic quantum
s	spin angular momentum
J	total angular momentum
ħ	Planck constant
δ_s	spin angular moment
γ	gyromagnetic ratio of angular momentum
χ_m	magnetic susceptibility
M	magnetization
M_r	remanent magnetization
H	magnetic field
Φ	magnetic flux
H	Hamiltonian
H_{DM}	Hamiltonian of Dzyaloshinskii–Moriya
J_d	direction exchange integral
ε_{ij}	relative permittivity
μ_{ij}	relative permeability
α_{ij}	Magnetoelectric coupling coefficient

Table of Contents

Chapter I Introduction

The control of bistable polarization states in ferroelectrics is the underlying basis of using two spontaneous polarisation “up” and “down” states to record the binary code “0” and “1” which was firstly proposed by J.R. Anderson who worked in Bell labs at 1952.[1] Ferroelectric (FE) random access memory (FRAM) exhibits fast-write and non-volatile characters. But they are limited by the need for destructive read and reset operation.[2,3] Magnetoresistive random access memory (MRAM) was developed since 1990s. MRAM consist of two parallel magnetic layers separated by a thin insulating layer in nano scale. One of the magnetic layers is a permanent magnetic layer in which the magnetization fixed in one direction and the other on is ferromagnetic (FM) layer in which the magnetization can be changed by external magnetic field. The two different states of the magnetic layers with magnetization in parallel or antiparallel shows different resistances which can be used to record the binary code “0” and “1”. MRAM obtains fast-read speed without an additional re-write operation compared to FRAM. However power costs are higher than that of FRAM during write operation. Materials that show simultaneously more than one ferroic characteristics such as coexistence of ferroelectric and magnetic ordering are currently gaining more and more attention. These properties give rise to the development of various kinds of materials and design of multifunctional devices application such as development of multiferroic memory devices with fast-low power electric write operation and non-destructive magnetic read operation.[4]

There are very few single phase multiferroic materials in nature since ferroelectricity and magnetism tend to exclude each other.[5] N. Hill found that electrons of transition metal in 3d orbital which are necessary for magnetism could reduce the tendency for off-centre ferroelectric distortion. This behaviour is in contradiction with the ferroelectricity which is related to the hybridization of empty 3d orbital of centre cations such as Ti^{4+} and 2p orbital of oxygen.[5] Many efforts have been devoted for new room temperature magnetoelectric multiferroics due to a strong desire to fabricate materials with novel functions.[6] Two requirements are necessary to be satisfied in the commercial device: room temperature multiferroic behaviour and strong coupling between ferroelectric and magnetic properties.[4] The initial researches focused on $BiFeO_3$ (BFO) a lead free multiferroic material. BFO shows ferroelectric order (T_c = 1100 K) and antiferromagnetic order (T_N = 640 K) at room temperature.[7] However, the high leakage current, tendency to fatigue and secondary phase in the grain boundary restrict its application. Consider of the large leakage current of $BiFeO_3$, Aurivillius multiferroics which can be considered as inserting $BiFeO_3$ layer into bismuth layer structured ferroelectrics (BLSFs) exhibit good insulativity and have been proposed to fabricate new room temperature multiferroic materials.[8,9] $Bi_5FeTi_3O_{15}$ (BFTO) has been successfully synthesised by combination of $BiFeO_3$ with a bismuth layer structured ferroelectrics, $Bi_4Ti_3O_{12}$ (BIT). BFTO presents ferroelectric and antiferromagnetic order below 80 K.[10] The magnetization of BFTO can be remarkably improved by substituting parts of Fe^{3+} by Co^{3+} and magnetic Curie temperature increase to 618 K.[11] To date, room temperature multiferroic behaviour has been

reported in BLSFs with $m \geq 4$. However, there are still debates about the origin of the ferromagnetism. Although the second phase may has contribution to the magnetism, the intrinsic multiferroic character of the main phase was supported by the magnetic control of ferroelectric domain switching in $Bi_6Ti_{2.8}Fe_{1.52}Mn_{0.68}O_{18}$.[12] Therefore, this thesis is to develop single phase multiferroic Aurivillius materials and investigate their dielectric, ferroelectric and ferromagnetic properties.

In this research, multiferroelectric behaviour of $(Bi_2O_2)^{2+}(A_{m-1}B_mO_{3m+1})^{2-}$ with different octahedral layers (m=2, 3, 4 and 5) has been studied. We propose to substitute parts of Fe by Co to improve magnetism. The origin of weak ferromagnetism of BFTO is the indirect super exchange coupling of Fe^{3+} cations (Fe^{3+}-O-Fe^{3+}). Doping Co^{3+} cations cannot directly improve the ferromagnetic property of BFTO because the magnetic moment of Co^{3+} is smaller than Fe^{3+}(the magnetic moment of Co^{3+} and Fe^{3+} are $4.9\mu_B$ and $5.92\mu_B$, respectively), but the superexchange interaction between Co^{3+} and Fe^{3+} cations (Co^{3+}-O-Fe^{3+}) contribute to the improvement of ferromagnetism.[11]

Due to highly anisotropic plate-like grain shape of BFTO, the main directions of polarization and magnetisation are in a-b plane. Grain-oriented textured ceramics have been already successfully prepared using a two-step Spark Plasma Sintering (SPS) method.[13,14] The two-step method was used to fabricate textured bulk ceramics and obtain better ferroelectric and magnetic properties than that of random oriented ceramics. Moreover, in order to research the coupling between ferroelectric and ferromagnetic, in-situ neutron diffraction of BLSFs with external magnetic field and

ferroelectric domains changes under magnetic field were also investigated.

A brief introduction of the basic theory of ferroelectricity, magnetism and multiferroelectricity is given in Chapter 2. A review of the common multiferroelectrics and Aurivillius phase multiferroelectrics is also included in this chapter. Chapter 3 is the details of experiments of this research. Chapters 4, 5, 6 and 7 showed the experimental results and discussion of multiferroic BLSFs with different octahedral layers (m=2, 3, 4 and 5), respectively. In Chapter 8, the main conclusions of this research are given including a comparison of multiferroic behaviour in BLSFs with different octahedral layers. Plans for future work are also outlined.

Chapter II Literature Review

2.1 Background of Ferroelectrics

The key issue of ferroelectrics is spontaneous polarization (P_s) which is tightly related to the crystal structure. All crystals can be divided into 32 crystal point groups by using different symmetry elements, such as centre of symmetry, axes of rotation, mirror planes and their combinations. Among the 32 crystal point groups, only 10 of them exhibit spontaneous polarization, which are defined as polar point groups. These 10 point groups belong to non-centrosymmetric point groups which is necessary for the existence of piezoelectricity. The spontaneous polarization varied with the change of temperature due to the temperature dependence of atomic configuration, which is defined as pyroelectricity. The difference between ferroelectrics and pyroelectrics is that the spontaneous polarization can be switched by applying an external electric field. Thus, all ferroelectrics are pyroelectrics and piezoelectrics, but not in reverse way.[15-17]

Ferroelectric is an important kind of functional material. Until now, a number of materials have been found to obtain ferroelectric properties. The main ferroelectric oxide families are: perovskite oxides ABO_3 ($BaTiO_3$), $LiNbO_3$ group, Aurivillius phase layer structured group ($Bi_3Ti_4O_{12}$) and tungsten bronze group ($Ba_xSr_{5-x}Nb_{10}O_{30}$). Ferroelectrics have been widely used in many commercial applications such as: ignitor, capacitors, random access memories, transpolarizers and piezoelectric sensors.[4,18,19] $SrBi_2Ta_2O_9$ and $Bi_{3.25}La_{0.75}Ti_3O_{12}$ which belong to Aurivillius layer structured ferroelectrics are excellent candidates of non-volatile ferroelectric random-access

memories.[20,21] Thus, Aurivillius layer structured ferroelectrics were researched as the base materials in this work.

All of ferroelectrics obtain the characteristics including: Curie Point (T_c), Spontaneous Polarization (P_s), Ferroelectric domain switching proved by Ferroelectric hysteresis loops.

2.1.1. FE Curie point

Most ferroelectric materials transform from a high-temperature centrosymmetric (paraelectric) phase into a low-temperature non-centrosymmetric (ferroelectric) phase at T_c. Dielectric, elastic, thermal and other properties of the material commonly become abnormal around the Curie point. This is different for 1st and 2nd order transitions. Figure 2.1 shows the data measured on $BaTiO_3$ ceramic. It shows spontaneous polarization along c axis in tetragonal phase under T_c and none spontaneous polarization in cubic phase above T_c. The dielectric permittivity changes with temperature obey the Curie-Weiss law above the T_c.

Some ferroelectrics such as $BaTiO_3$ have several ferroelectric phase transitions and the direction of P_s change during each phase transition (Fig. 2.2). But only the first transition temperature from cubic paraelectric phase to tetragonal ferroelectric phase is called Curie point. In $BaTiO_3$, P_s is along [001], [011] and [111] in tetragonal, orthorhombic and rhombohedral phase, respectively.

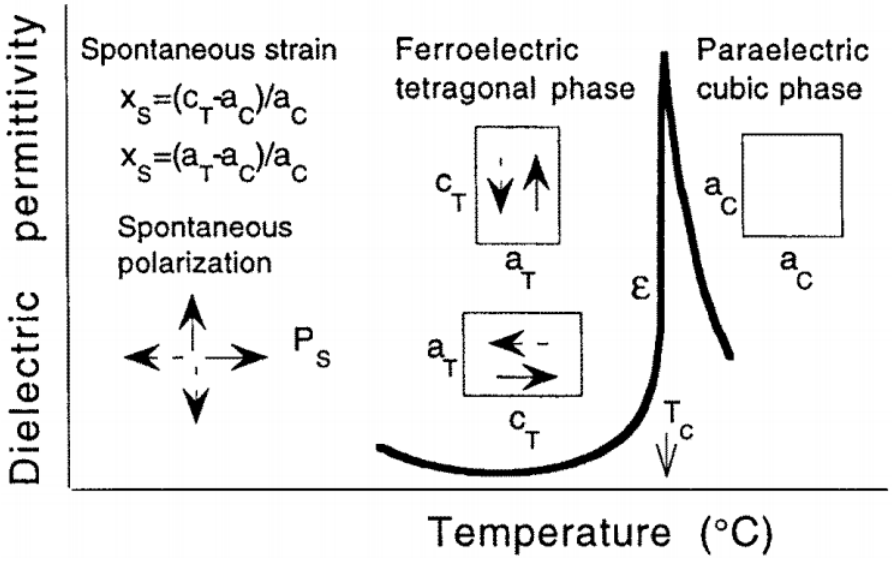

Fig 2.1 Temperature dependence of dielectric permittivity of ferroelectric $BaTiO_3$ near Curie temperature. a_C is the lattice parameter of cubic phase, a_T and c_T are the lattice parameters of tetragonal phase. x_S is the strain along the *a*-axis or *c*-axis.[22]

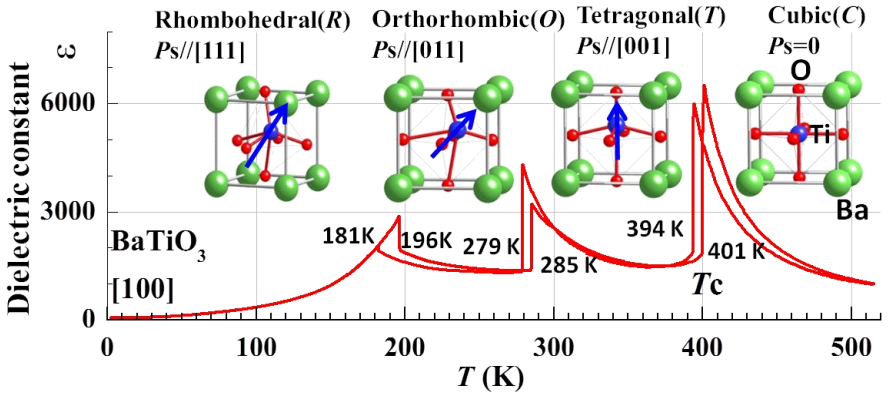

Fig. 2.2 Ferroelectric phase transition of $BaTiO_3$ single crystal during heating and cooling.[23]

2.1.2. Ferroelectric domain

Ferroelectric domain is a region with spontaneous polarizations in the same direction. Spontaneous polarizations in ferroelectric crystal are normally not uniformly aligned

throughout the whole crystal. For example, the crystal structure of $BaTiO_3$ changes from cubic to tetragonal during the ferroelectric transition and the P_s is along c axis of tetragonal (Fig. 2.2). The three a_c axes in cubic are the same and the P_s could arise from any of them during the phase transition. The crystal contains many domains in which the spontaneous polarization along in the same direction. The region between two domains is named domain wall (Fig. 2.3). Ferroelectric domain walls are in the order of 1- 10 nm which are much narrower than domain walls in ferromagnetic materials.[22] In order to achieve the lowest free energy of the system, two kinds of domain walls are formed. The walls which separate domains with oppositely orientated polarization are called 180 ° walls. The other walls which separate regions with mutually perpendicular polarization are called non-180 ° or 90 ° walls. The 180 ° domains can help to reduce the energy caused by depolarization field which is formed during the phase transition at T_c.

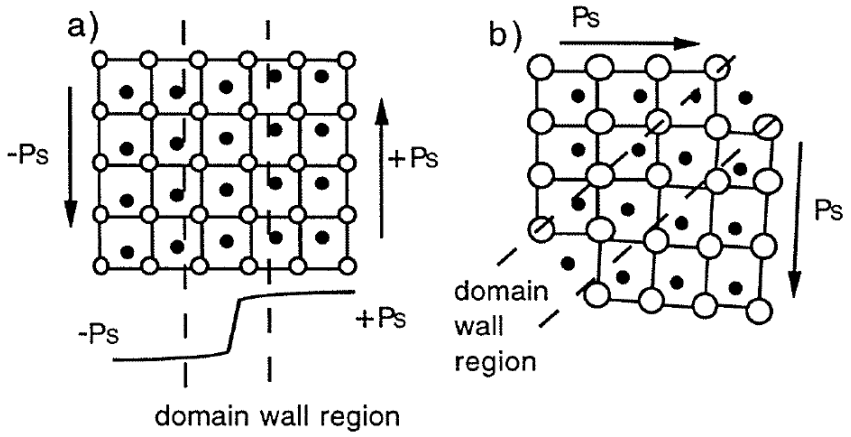

Fig. 2.3 Illustration of (a) 180 ° and (b) 90 ° ferroelectric domains and domain-wall regions in a tetragonal perovskite ferroelectric.[22]

The non-180 ° or 90 ° walls can help to reduce the strain energy caused by the lattice distortion during the phase transition and depolarization field. In 2011, the 180 ° and 90 ° domain walls were observed in atomic-resolution in $PbZr_{0.2}Ti_{0.8}O_3$ film by C.L. Jia (Fig. 2.4).[24]

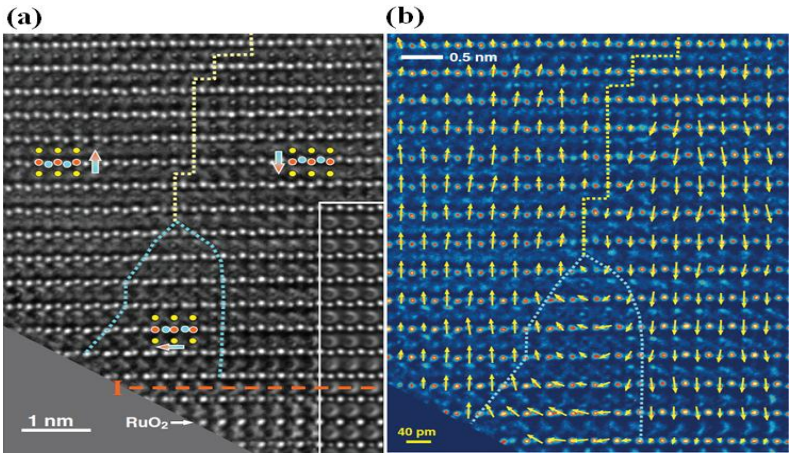

Fig. 2.4 (a) Atomic-resolution image of a flux-closure structure with continuous rotation in $PbZr_{0.2}Ti_{0.8}O_3$ film. I is the interface between $PbZr_{0.2}Ti_{0.8}O_3$ and substrate. Yellow line is the 180 ° domain wall and blue line is 90 ° domain wall. (b) Map of atomic displacement vector. The arrow is the displacement of Zr-Ti atoms.[24]

2.1.3. Ferroelectric hysteresis loops – domain switching

The direction of spontaneous polarization in each domain can be reserved by applying an electric field; the relationship between polarization intensity *P* and electric field *E* is not linear but like a hysteresis loop, as show in Fig. 2.5 Domains which polarization have the same directions with the external electric field grow up and domains with the

reversed direction become small, which makes polarization intensity increasing with the increase of external electric field (from A to D). Finally, most domains are aligned and polarization becomes saturated. Extending DC, the intercept with *y* axis is a spontaneous polarization. The P_s in polycrystalline materials is smaller than that of a single crystal due to the different orientations of grains. When electric field decreases to zero, some domains switch back and the polarization at $E = 0$ is the remnant polarization P_r.

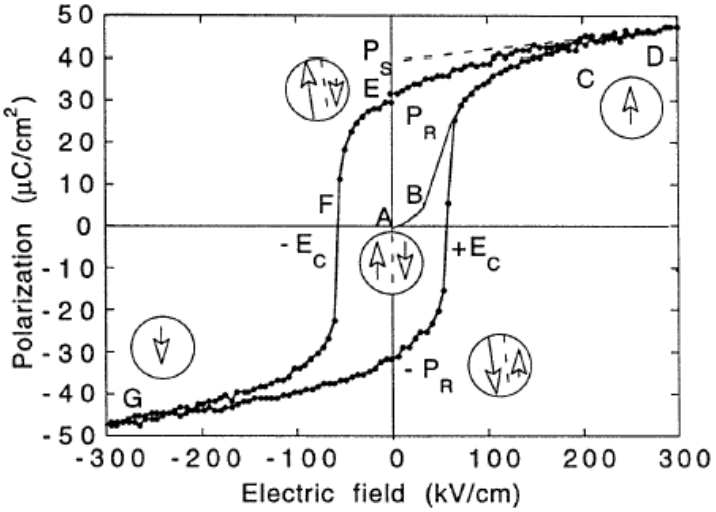

Fig. 2.5 Ferroelectric hysteresis loop. Circles with arrows represent the polarization state of the material at the indicated fields.[22]

Then electric field increase in reserved direction. The electric field that makes polarization decrease to zero is coercive field E_c. The macro polarization reserved at E_c. The $\pm P_r$ are stable in zero electric field, which do not need external field to keep it.

2.2 Background on magnetism

2.2.1 Macro-magnetism of bulk material

The magnetism of material originates from the orbital movement and spin of unpaired electrons. Thus, according to the interaction of the electrons, materials can be divided into the following groups:

1. Diamagnetism and paramagnetism

There are no unpaired electrons in the diamagnetic materials. The procession of the electronic orbits of the atoms about the external magnetic field direction will induce a small magnetic moment reserves to the external magnetic (Fig. 2.7a). As a consequence, the magnetic susceptibility χ_m which is related to the magnetization M and magnetic field H is negative and the value is about -10^{-6}.

$$\mathrm{M} = \chi_m H \tag{1}$$

The relative permeability μ_r is:

$$\mu_r = \chi_m + 1 \tag{2}$$

Paramagnetic materials are the materials with unpaired electrons but no exchange interaction between them. Due to the thermal motion, the magnetic moment of atoms will orient in random direction (Fig. 2.7b). The magnetic susceptibility χ is about 10^{-5}-10^{-2}.

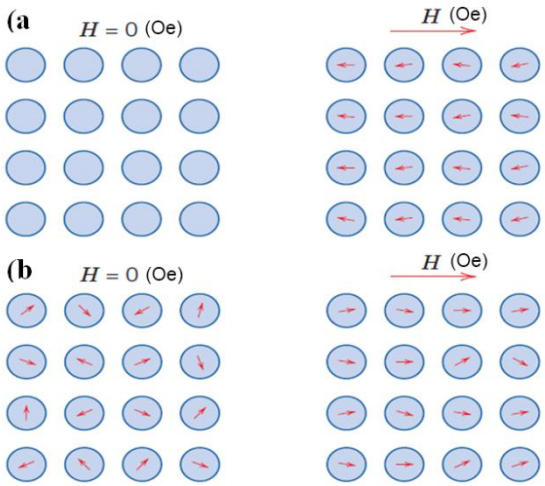

Fig. 2.7 The atomic dipole configuration with and without a magnetic field of (a) diamagnetic materials, (b) paramagnetic materials.[25]

2. Ferromagnetism, antiferromagnetism and ferrimagnetism

The magnetic moment of ferromagnetism (χ_m~10-10^5), antiferromagnetism (χ_m~10^{-3}) and ferrimagnetism (χ_m~10-10^5) are in order due to the direct exchange interaction or indirect exchange interaction.[26] The magnetic moments of ferromagnetics aligned in parallel which leads to a magnetic spontaneous polarization (Fig. 2.8a). The magnetic moments of antiferromagnets aligned in anti-parallel which leads to no net magnetization. However, the magnetic moments of some antiferromagnets are not perfectly aligned in anti-parallel resulting in a small residual magnetization. This magnetism is named as canted antiferromagnetism. The magnetic moments of ferrimagnetics aligned in anti-parallel too. However, the two magnetic moments in anti-parallel are not equal resulting in a residual magnetization. The magnetic susceptibilities of the phase of ferromagnetic, antiferromagnetic and ferromagnetic above T_C/T_N obey the Curie-Weiss law (Fig. 2.8)

$$\chi = \frac{C}{T - T_c} \quad (3)$$

Magnetic materials exhibit magnetic field dependent of magnetization hysteresis loop (*M-H*) analogies to the *P-E* loop in ferroelectrics (Fig. 2.9).

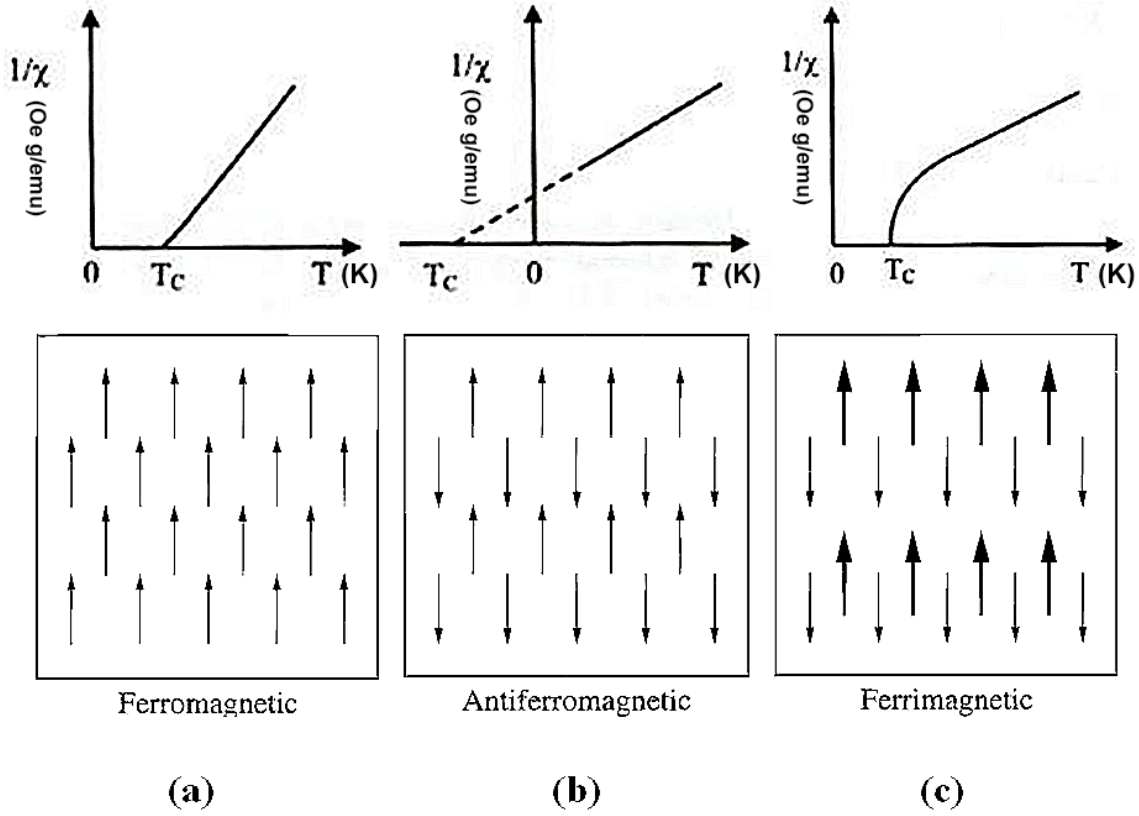

Fig. 2.8 Temperature dependence of inverse magnetic susceptibility and the magnetic moment in (a) ferromagnetic, (b) antiferromagnetic and (c) ferromagnetic material.[26]

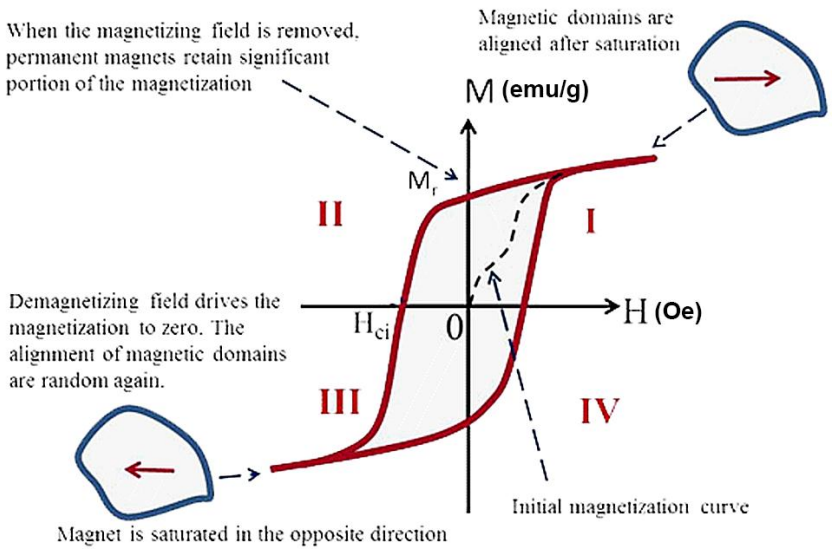

Fig. 2.9 Magnetic field-magnetization hysteresis loop of a ferromagnetic polycrystalline.[25]

2.2.2 Direct exchange

The ferromagnetism and antiferromagnetism of metals are mainly caused by the direct exchange interaction between the neighboured metal atoms. The Hamiltonian (*H*) is generalized between the nearest-neighbour atoms (Heisenberg model):

$$H = -2J_d S_1 \cdot S_2 \qquad (4)$$

Where S_1 and S_2 are the total spin quantum number of the neighboured atoms, J_d is the direction exchange integral.[27]

2.2.3 Indirect exchange interaction

The magnetism of magnetic oxide is due to the indirect exchange interactions which include superexchange interaction and double exchange interaction. Unlike the transition metals and alloys, the transition-metal cations in insulators are separated by

the anions with no magnetic moment. For example, in magnetic oxide, the electrons are localized and only a few 3d electrons are coupled through direct exchange interaction. Thus, the magnetization of magnetic metal oxide cannot be explained by the Heisenberg model. Most of the transition-metal 3d-orbitals are hybridized with oxygen 2p-orbitals and the 3d-orbitals of neighboured cations are able to couple through oxygen. There are two types of indirect exchange interaction: superexchange interaction and double exchange interaction.

Superexchange interaction:

A typical superexchange interaction is showed in MnO (Fig. 2.10). There is no magnetic moment due to the full 2p orbitals of oxygen in ground state (Fig. 2.10a). The oxygen can be turned into active state (Fig 2.10b) based on experiment and theory calculation. One of the 2p electrons such as P' leaps into the neighboured 3d orbital of Mn^{2+} and residual single P electron can couple with d_2 electron of the other Mn^{2+} through direct exchange interaction. During this process, the spin of the electrons follow the rules below:

1. P' electron obeys the Hund`s rule and the spin keeps the same direction during the transition;

2. The spin of P' and P are in anti-parallel;

3. The coupling between P and d_2 electrons is based on direct exchange integral (anti-parallel for $J_d<0$, parallel for $J_d>0$)

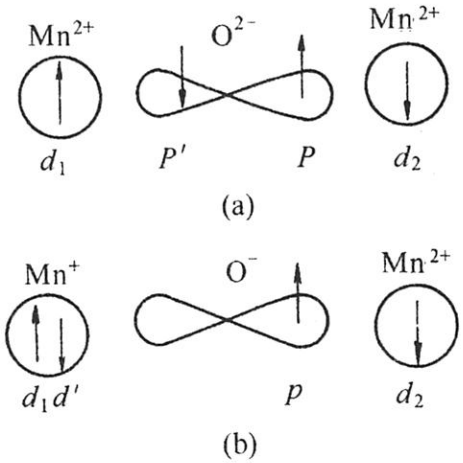

Fig. 2.10 Superexchange interaction in MnO.[28]

Thus, the spin of d_1 is able to couple with d_2 through the transition of P' electron. Generally, the direct exchange integral (J_d) is negative for oxygen anions and transition-metal cations. So we can have the following conclusions:

1. Compounds exhibit antiferromagnetic or ferrimagnetic behaviour when the 3d orbitals of cations are in or over half filled.

2. Compounds exhibit ferromagnetic behaviour when the 3d orbitals of cations are less than half filled.

Magnetism in many transition metal oxides has been explained by this rule. However, it cannot explain the magnetism of some other magnets; for example, Cr_2O_3 is antiferromagnetic which should be ferromagnetic based on this rule. Then, this rule was corrected by Goodenough and Kanamori by considering the orbital splitting and symmetry in crystal field.[29,30] The direct exchange integral between the oxygen anions and transition-metal cations is negative if there is no overlap between the 2p orbital of

oxygen and 3d orbital of magnetic metal cations (orthogonal), otherwise J_d is positive (none-orthogonal). Figure 2.11 shows all the none-orthogonal state of 2p and 3d orbitals in 180 ºalong y axis.

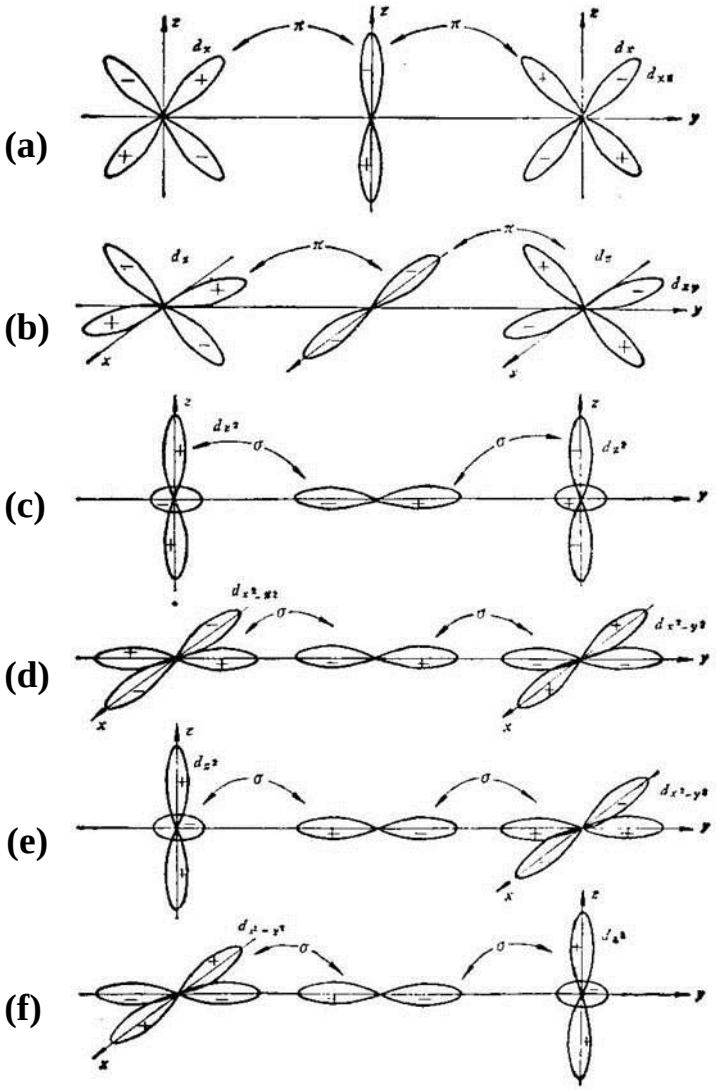

Fig. 2.11 None-orthogonal states of 2p and 3d orbitals in 180 ºalong y axis. (a) d_{yz}-p_z-d_{yz}, (b) d_{xy}-p_x-d_{xy}, (c) dz^2-p_y-dz^2, (d) dx^2-y^2-p_y-dz^2, (e) dz^2-p_y-dx^2-y^2, (f) dx^2-y^2-p_y- dz^2. [31] ("π" bond represent the coupling between t_{2g} orbitals (d_{xy}, d_{yz}, and d_{zx}) and 2p orbitals, "δ" bond represent the coupling between e_g (dz^2 and dx^2-y^2) orbitals and 2p orbitals, "+" and "-" represent the two directions of electron spin in one orbital).

In addition, the state of 3d-2p orbital is more complicated by considering the none-180 º symmetry of the crystal. Table 2.1 shows the all states of the 2p-3d orbitals. For example, there is overlap between dz^2 and p_y when the orbitals align along x axis (non-orthogonal) which is showed in Fig. 2.11c. If dz^2 and p_y align along x or z axis, there is no overlap between them (orthogonal).

Table. 2.1 the state of the 2p-3d orbitals.[31]

		+ orthogonal		- non-orthogonal	
d		p_x	p_y	p_z	s
z^2	X	$-(\sigma)$	+	+	$-(\sigma)$
	Y	+	$-(\sigma)$	+	$-(\sigma)$
	Z	+	+	$-(\sigma)$	$-(\sigma)$
x^2-y^2	X	$-(\sigma)$	+	+	$-(\sigma)$
	Y	+	$-(\sigma)$	+	$-(\sigma)$
	Z	+	+	+	+
xy	X	+	$-(\pi)$	+	+
	Y	$-(\pi)$	+	+	+
	Z	+	+	+	+
yz	X	+	+	+	+
	Y	+	+	$-(\pi)$	+
	Z	+	$-(\pi)$	+	+
zx	X	+	+	$-(\pi)$	+
	Y	+	+	+	+
	Z	$-(\pi)$	+	+	+

Double exchange interaction:

Double exchange interaction is the interaction between the magnetic transition ions with different spin amount through the media of oxygen anion. Fig. 2.12 shows the double exchange interaction in $La_{1-x}A_xMnO_3$ (A=Ca, Sr or Ba).[32] One electron of 2p orbital of

O^{2-} jumps into the 3d orbital of Mn^{4+}. The vacant 2p orbital of O^{2-} can be filled by one 3d electron from Mn^{3+}. According the partially filled 3d orbitals of Mn^{3+} and Mn^{4+}, the spin of the 2p electron which jumps into 3d orbital of Mn^{4+} is parallel to the spin of 3d electrons of Mn^{4+} and 3d electron which jumps into 2p orbital of oxygen. Thus, the magnetic moments of Mn^{3+} and Mn^{4+} are coupled through the media of O^{2-}.

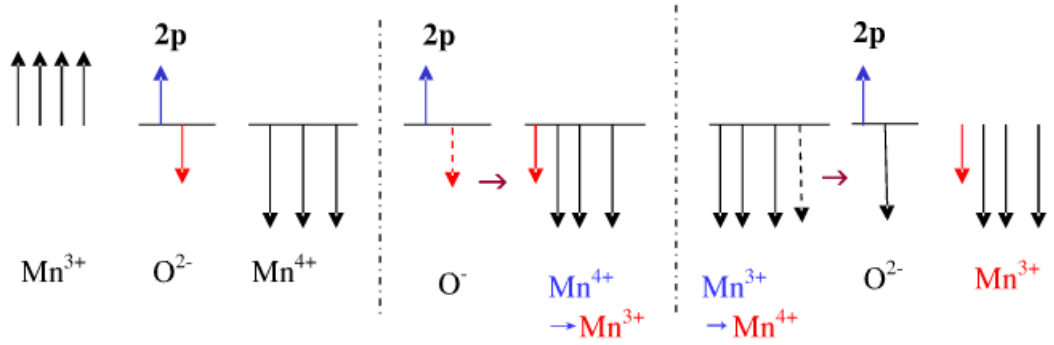

Fig. 2.12 Double exchange interaction in $La_{1-x}A_xMnO_3$.[32]

2.3 Multiferroic

2.3.1 Classification of single phase multiferroics

Multiferroics are the single phase crystals simultaneously exhibiting two or more primary ferroic order at the same temperature and can be interact with each other (Fig. 2.13). Magnetism in multiferroics is either from the interaction between local magnetic moments of transition metal cations or rare earth cations. However, the FE polarization originates from variant mechanisms. According to the origin of electric polarization and magnetization, the multiferroics can be divided into the two types. Type-I multiferroics are the materials in which magnetism and ferroelectricity come from different sources.

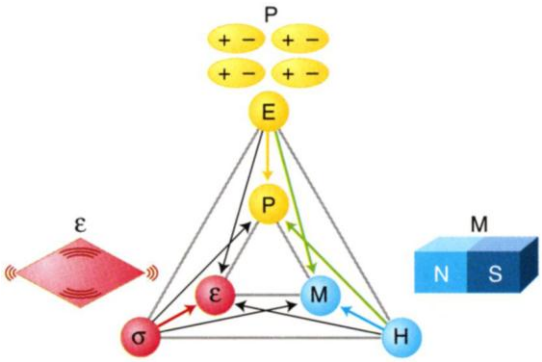

Fig. 2.13 Phase control in ferroics and multiferroics. The electric polarization P, magnetization M, and strain ε can be controlled by electric field E, magnetic field H and stress σ, respectively. The coexistence of at least two ferroic orders leads to additional interactions.[33]

Type-II multiferroics are the materials with ferroelectricity caused by the magnetic order.[34] The displacement of magnetic cations in B-site of Aurivillius phase materials contribute to parts of the ferroelectric polarization. Thus, multiferroic Aurivillius phase materials are a mixture of Type-I and Type-II multiferroics.

Type-I multiferroics

Type-I multiferroics normally exhibit large electric polarization and high FE Curie temperature. Based on the origin of ferroelectricity, type-I multiferroics can be divided in the following groups:

1. Ferroelectric displacement of B-site cations with d^0 electrons

A large number of ABO_3 multiferroics are designed by using magnetic ions to replace parts of the B-site cations such as $BaTi_{1-x}Fe_xO_{3-\delta}$ and $Pb(Fe_{1/2}Nb_{1/2})O_3$ (PFN).[35,36] The

FE polarization of this kind of materials comes from the displacement of the central cations with respect to the oxygen octahedra. The weak magnetism is from the canted antiferromagnetic order based on the superexchange interaction of Fe^{3+}-O-Fe^{3+}. However, these materials all have low magnetoelectric effect. Studies on ferroelectric and magnetic properties of several Pb-based perovskites of general formula $Pb(B`B``)O_3$ have been reported (Table.2.2). Further researches have been reported to achieve novel room temperature multiferroics based on solid solutions including relaxor multiferroics and ferroelectrics such as $(1-x)Pb(Fe_{1/2}Nb_{1/2})O_3$(PFN)-$xPb(Zr_{0.2}Ti_{0.8})O_3$, $0.8Pb(Fe_{2/3}W_{1/3})O_3$(PFW)-$0.2PbTiO_3$ and $(1-x)Pb(Fe_{1/2}Ta_{1/2})O_3$(PFT)-$xPb(Zr_{0.53}Ti_{0.47})O_3$.[37-39].

Table 2.2 The ferroelectric Curie temperature and magnetic Neel temperature of Pb_2FeXO_6 (X = Ta, Nb. W), and ferroelectric Curie temperature of $PbZr_{1-x}Ti_xO_3$.[40]

	$Pb(Fe_{1/2}Nb_{1/2})O_3$	**$Pb(Fe_{2/3}W_{1/3})O_3$**	**$Pb(Fe_{1/2}Ta_{1/2})O_3$**	**$Pb(Zr_{1-x}Ti_x)O_3$**
T_C	380 K	180 K	310 K	620 K
T_N	140-150 K	380 K	150 K	-

The room temperature crystal structure of 0.4PFT/0.6PZT is orthorhombic (*Pmm2*). Magnetic field control of ferroelectric domain in PFT/PZT at room temperature has been reported by D.M. Evans et al (Fig. 2.14).[41] Fig. 2.14 a and b are the lateral PFM images of PFW/PZT scan in two directions. The directions of in-plane polarization are

showed in four colours in Fig. 2.14 c by combining Fig. 2.14 a and b. These ferroelectric domain areas changed under an external magnetic field perpendicular to the plane. However, the magnetoelectric effects of PFW/PZT and PFT/PZT are not bilinear $\alpha_{ij}P_iM_j$ coupling which is an indirect interaction through magnetostriction and electrostriction.[42] The ME coupling coefficient is about $1*10^{-7}$ s/m.

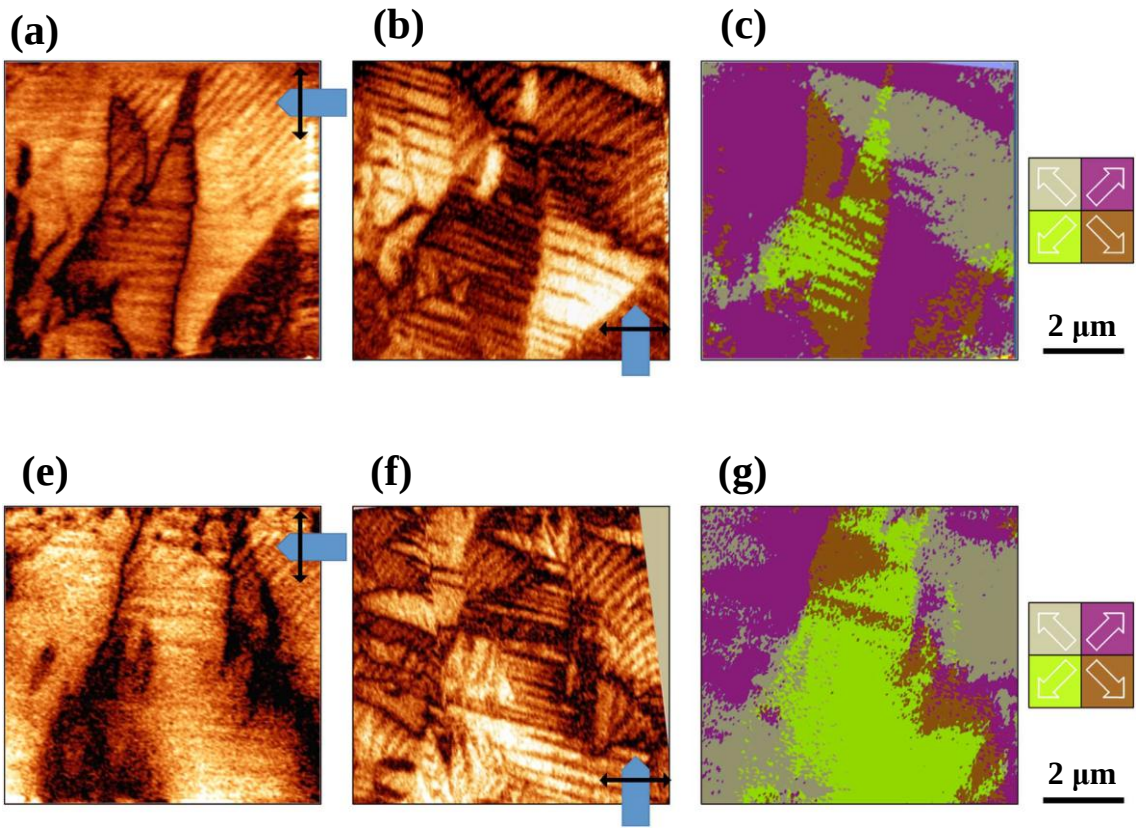

Fig. 2.14 Magnetic field control of ferromagnetic domain at 295 K. (a) and (b) lateral PFM images scanned in two directions, and (c) in-plane polarization without magnetic field. (e) and (f) lateral PFM images scanned in two directions, and (g) in-plane polarization under 18 kOe magnetic field. [41]

2. Ferroelectricity - 6S lone electron pairs

Unlike $BaTiO_3$, the polarization in parts of oxide perovskites is mainly attributed to the

long pair (s^2 orbital) of A-site cations, which is dominant in the multiferroics such as $PbMnO_3$, $PbFeO_3$, $BiMnO_3$ and $BiFeO_3$.[43-47] To date, $BiFeO_3$ is the most well-known room temperature multiferroic material with T_N ~ 643 K and T_c ~ 1103 K.[7] The room temperature crystal structure is rhombohedral (*R3c*) and the electric polarization mainly comes from the movement of Bi^{3+} cations with respect to the distorted FeO_6 octohedra along [1 1 1] (Fig. 2.15a). Large remnant polarization (P_r ~ 60 μC/cm^2) has been reported in bulk sample (Fig. 2.15b).[48] The ME coefficient are measured up to 3 V cm^{-1} Oe^{-1} in thin film at room temperature.[7]

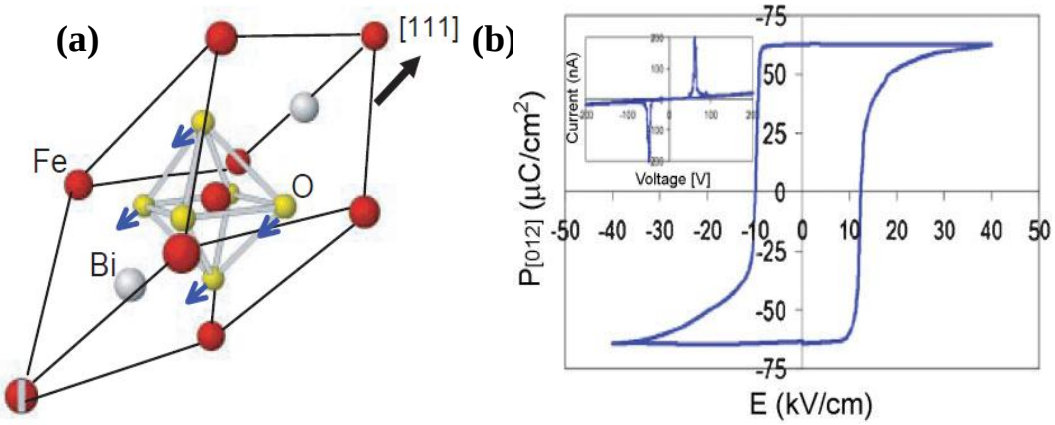

Fig. 2.15 (a) Unit cell of $BiFeO_3$ in bulk sample, (b) P-E loops of $BiFeO_3$ in bulk sample[7,48]

The canted antiferromagnetic order of BFO originates from superexchange interaction of Fe^{3+}-O-Fe^{3+}. Below Neel temperature, the canted antiferromagnetic spins (blue and green arrows in Fig. 2.16) give rise to a net magnetic moment (purple arrows) which is a cycloid magnetic order along [1 0 -1]. The net magnetic moment is contained within the plane defined by propagation vector [1 0 -1] and polarization vector [1 1 1] and the

repeat period is 64 nm (Fig. 2.16).

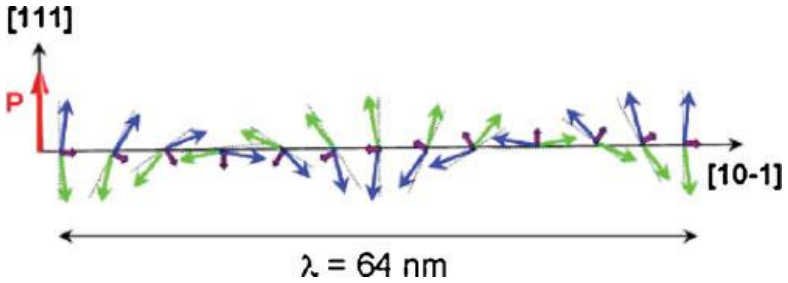

Fig. 2.16 Schematic of spin cycloid in $BiFeO_3$.[49]

Recently, ferroelectric and ferromagnetic domains have been found in the same area for the first time in ceramic composite of $(BiFe_{0.9}Co_{0.1}O_3)_{0.4}$-$(Bi_{1/2}K_{1/2}TiO_3)_{0.6}$ (Fig. 2.17).[50] The dark area and the bright area in Fig. 2.17a and Fig. 2.17b are the ferromagnetic and ferroelectric domains of the single phase multiferroic cluster, respectively. Ferroelectric domains can be changed by different magnetic fields which indicate the direct magnetoelectric coupling (Fig. 2.18). The ferromagnetic domains can be switched by electric field which indicate the converse magnetoelectric coupling (Fig. 2.19). Both strong direct magnetoelectric coupling and converse magnetoelectric coupling are reported in the multiferroic clusters, which confirm the intrinsic multiferroic behaviour.

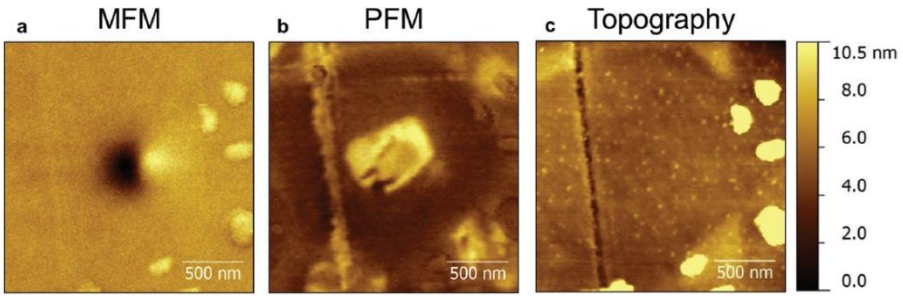

Fig. 2.17 MFM and PFM images of a multiferroic cluster.[50]

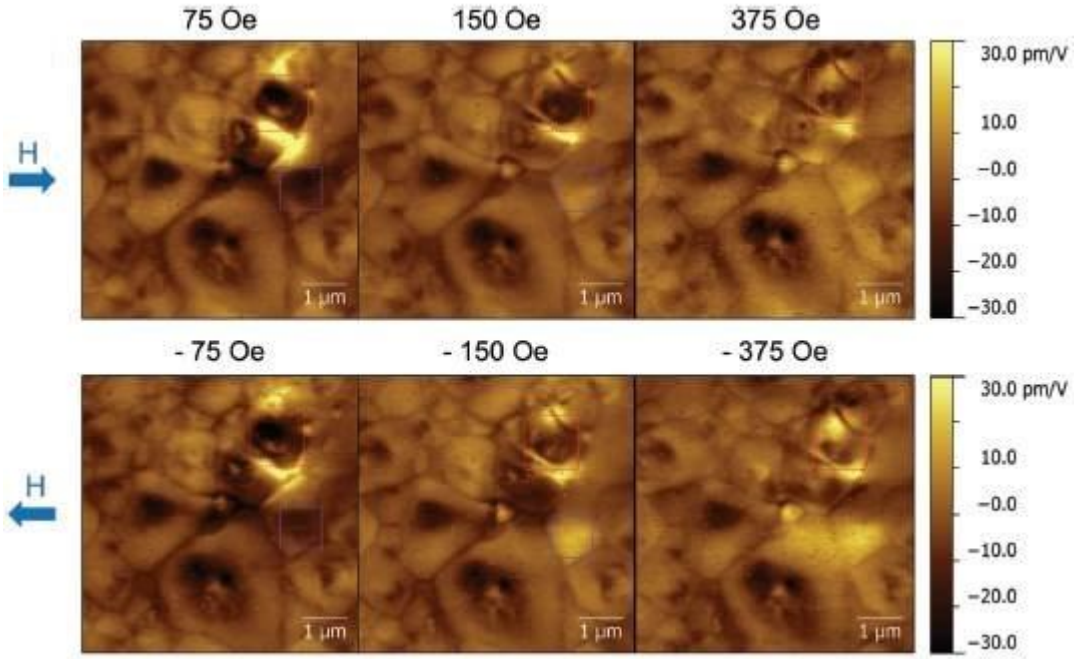

Fig.2.18 PFM images under different in-plane magnetic field.[50]

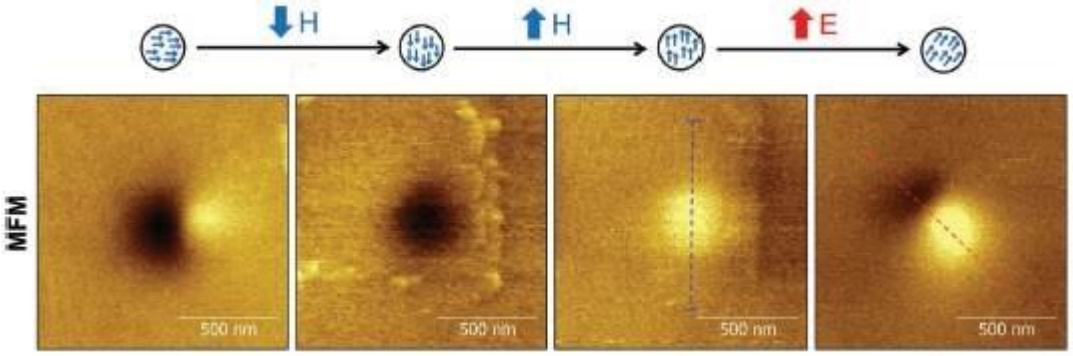

Fig. 2.19 MFM images under out-of-plane magnetic field and electric field. The magnetic domain can be switched by magnetic field and electric field.[50]

3. Geometric ferroelectricity

The ferroelectricity in $YMnO_3$ and $HoMnO_3$ are mainly from the tilting of the MnO_5 biprism which is shown in Fig. 2.20.[51] The polarization caused by the movement of the off-cantering of Mn^{3+} is very small that can be neglect. The ferroelectric phase

possesses $P6_3cm$ symmetry below 1270 K and a polarization about 5.5 μC cm^{-2} is induced along the hexagonal z axis.[52] $YMnO_3$ undergoes a strong change of atomic displacement without breaking the high temperature symmetry ($P6_3cm$) at the antiferromagnetic transition temperature (T_N~80 K). However, these atomic displacements are larger by two orders of magnitude than in any magnetic materials, which produces a coupling between the antiferromagnetic moment and ferroelectric polarization.[53]

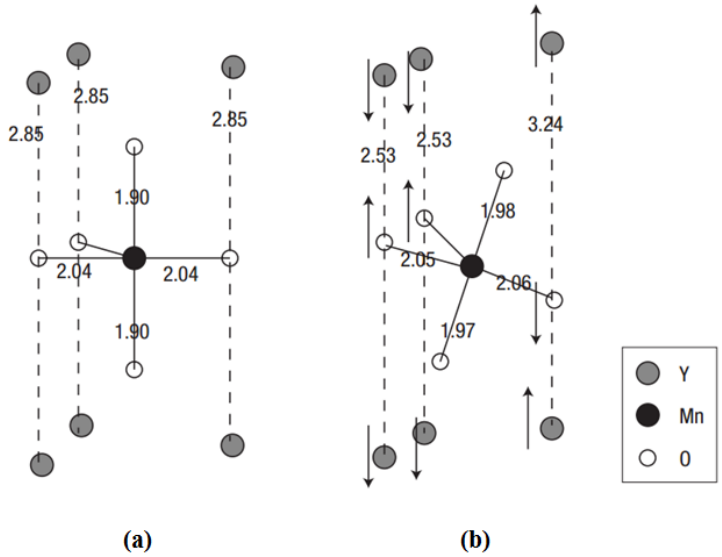

Fig. 2.20 Schematic of the origin of ferroelectricity in $YMnO_3$ (a) paraelectric phase, (b) ferroelectric phase.[51]

Strong magnetoelectric effect has been calculated in $Ca_3Mn_2O_7$ in which the magnetization can be switched 180 °by electric field. Two kind of distortions, Rotation distortion X_2^+(Fig. 2.21b) and tilting distortion X_3^-(Fig. 2.21c), occurred with decrease of temperature.[54,55] $Ca_3Mn_2O_7$ undergoes a ferroelectric transition from *I4/mmm* to $A2_1am$ at 280 K. The calculated polarization is about 5.5 μC cm^{-2} in *a*-*b* plane. The

antiferromagnetic Neel temperature of $Ca_3Mn_2O_7$ is about 115 K and the magnetic moment is along c axis due to crystal anisotropy.[54]

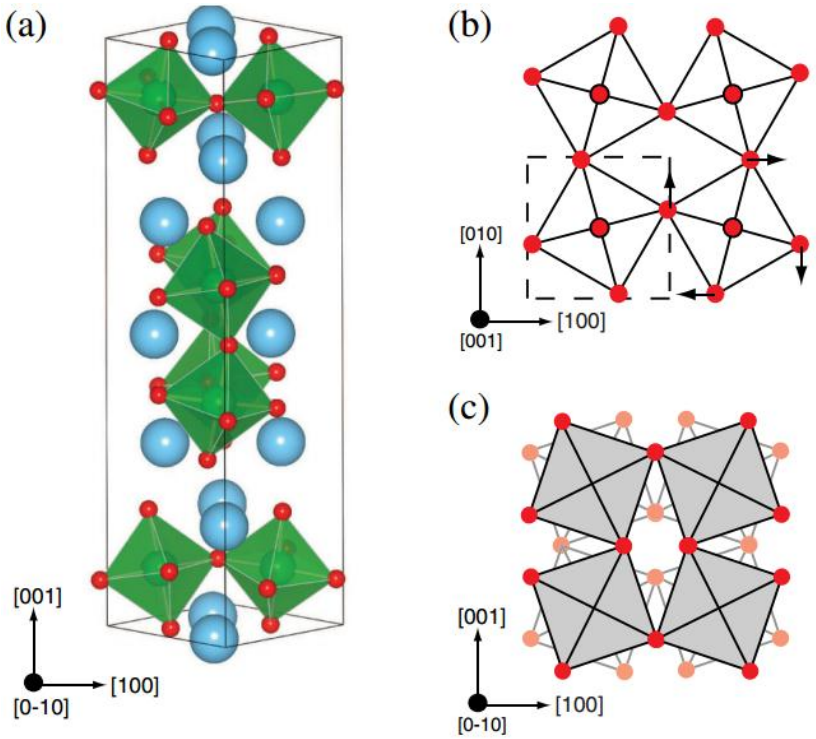

Fig. 2.21 Lattice distortion of $Ca_3Mn_2O_7$, (a) crystal structure of ferroelectric phase, the green part is MnO_6 octahedral, blue atom is Ca^{2+} (b) octahedral rotation. (c) octahedral tilting. All axes refer to the coordinate system of the *I4/mmm* parent structure[54]

4. Ferroelectricity from charge order

The cations with different valence are able to rearrange in order in compounds such as Fe_3O_4, $R_{1-x}Ca_xMnO_3$, $RNiO_3$ (R = Ho, Lu, Pr and Nd) and $LuFe_2O_4$.[56-62] $LuFe_2O_4$ is a hexagonal layer structured material. The charge order occurred when the temperature below 320 K.[62] Each layer is divided into a Fe^{2+} and Fe^{3+} rich layer which is showed in Fig. 2.22 b. The ground state is in antiferroelectric order (Fig. 2.22 a) and can be

changed into ferroelectric order under electric field with decrease of temperature. The magnetic Curie temperature is about 240 K. The ferrimagnetic order is determined by the competition between Fe^{3+}-Fe^{3+} superexchange and Fe^{2+}-Fe^{3+} double exchange which could induce a triangular frustrated system. As a consequence, One Fe^{3+} spin is parallel and the other two Fe^{3+} spins are antiparallel to Fe^{2+} (Fig. 2.23b). The ferrimagnetic magnetization is along *c*-axis below 240 K.

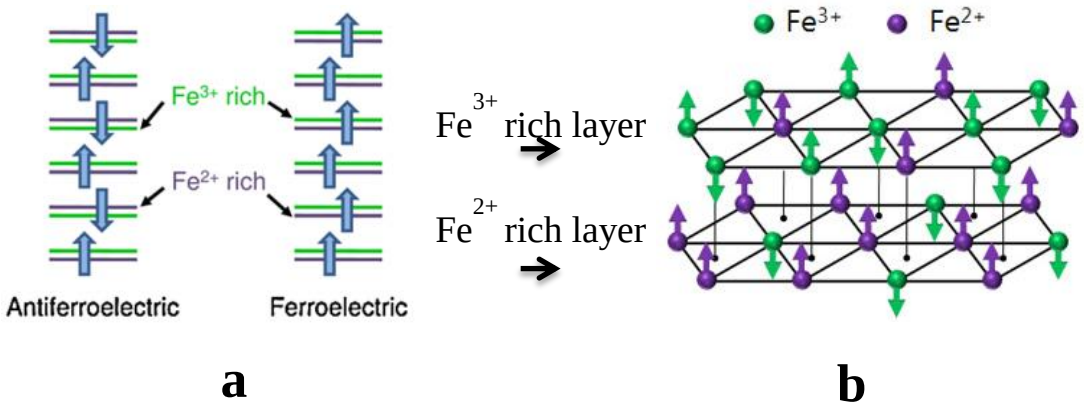

Fig. 2.22 (a) Fe^{2+} (Fe^{2+}/Fe^{3+}- 2:1) and Fe^{3+} (Fe^{2+}/Fe^{3+}- 2:1) rich double layer with charge order, (b) ferromagnetic spin structure of Fe^{2+} and Fe^{3+} in the double layer.[62]

Type-II multiferroics

The ferroelectricity of type-II multiferroics is induced by the magnetic order and normally the ferroelectric polarization can be switched by the external magnetic field. According to the type of magnetic order, the type-II multiferroics can be divided into the follow two groups:

1. Collinear magnetic structure

Magnetic order in this group is aligned in collinear direction. For example, the bond lengths of Co^{2+}-O-Mn^{4+} chains are the same in paramagnetic phase. The spins of Ca_3CoMnO_6 show an antiferromagnetic order at 16 K originate from the superexchange interaction between Co^{2+} and Mn^{4+} ($J_{Co\text{-}Mn}$), adjacent Co^{2+} ($J_{Co\text{-}Co}$) and adjacent Mn^{4+} ($J_{Mn\text{-}Mn}$) due to the short Co-Mn distance. The three interactions satisfied the condition, $J_{Co\text{-}Co} + J_{Mn\text{-}Mn} > J_{Co\text{-}Mn}$, which makes the spin order structure of ↑↑↓↓ (Fig. 2.23) more stable than the spin order structure of ↑↓↑↓.[63] The movement of cations in the Co^{2+}-O-Mn^{4+} chains with ↑↑ and ↑↓ spin order is different, which breaks the inversion symmetry of the chains. As a consequence, an electric polarization about 90 μC/m^2 is induced along the chain.[63]

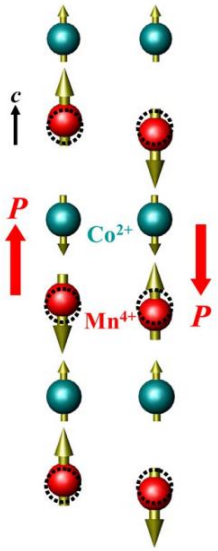

Fig. 2.23 Ising chains with the ↑↑↓↓ spin order and alternating ionic order of Ca_3CoMnO_6.[63] P is electric polarization

2. Non-Collinear magnetic spin structure

The second type of magnetic induced ferroelectricity is found in the materials with

non-collinear magnetic structures. The magnetic induced ferroelectricity was firstly reported in $TbMnO_3$.[64] Figure 2.24a shows the magnetic and ferroelectric phase transition of $TbMnO_3$. The magnetic spins of $TbMnO_3$ are in collinear spin-density wave order (incommensurate antiferromagnetic order) below the T_N~42 K due to the superexchange interaction of Mn^{3+}-O-Mn^{3+} (Fig. 2.24b). The collinear antiferromagnetic spin-density wave order of Mn^{3+} spins does not break the spatial inversion symmetry (*Pbnm*). Then, the collinear spin order turn to be a spiral spin order (commensurate antiferromagnetic order) at 28 K which induces a polarization along *c*-axis (Fig. 2.24c) and the details will be explained in Fig. 2.26.

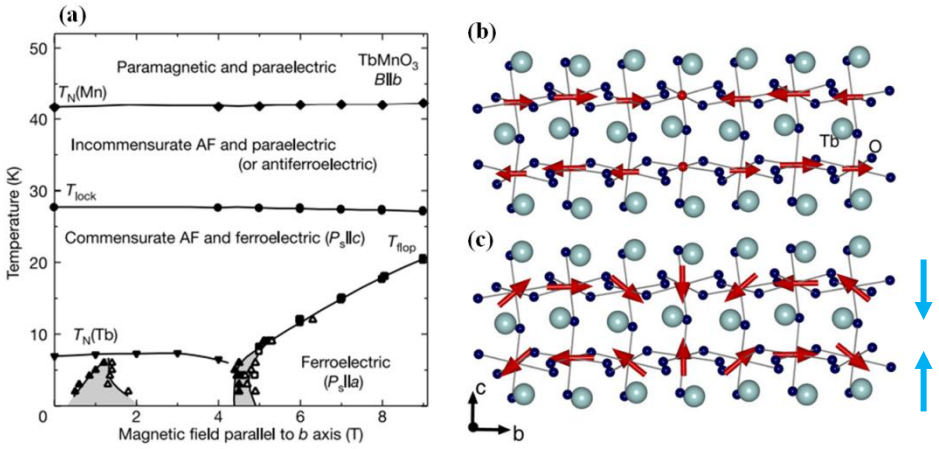

Fig. 2.24 (a) Magnetic and ferroelectric phase transition of $TbMnO_3$, (b) the spin-density wave ordering of the Mn^{3+} spins in the paraelectric phase below T_N = 42 K, and (c) the cycloid ordering in the ferroelectric phase below T_c = 28 K. (red arrow is the magnetic moment, blue arrow is the electric polarization)[64]

The antiferromagnetic phase transition at 7 K is attributed to the magnetic ordering of Tb^{3+}. The ferroelectric polarization can be changed from *c*-axis to *a*-axis when apply

an external magnetic field parallel to the *b*-axis (Fig. 2.25).

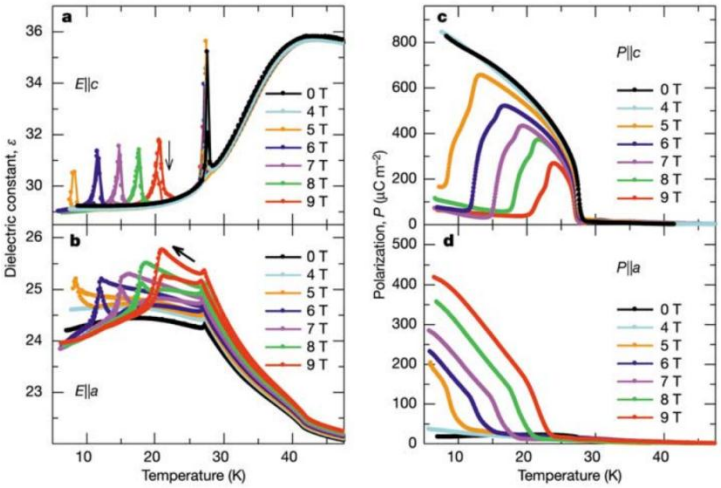

Fig. 2.25 Electric polarization flop induced by magnetic fields in $TbMnO_3$. Temperature profiles of dielectric constant at 10 kHz (a and b) and of electric polarization along the *c* and *a* axes (c and d), respectively. Magnetic fields are along *b* axis.[65]

Then, the similar behaviours were found in $DyMnO_3$ and $TbMn_2O_5$.[66,67] In order to explain this none-collinear magnetic order induced ferroelectricity, Katsura, Nagaosa and Balatsky proposed a model named as spin-current model or KNB model (Fig. 2.26a):[68]

$$\mathrm{P} = A_0 e_{ij} \times (S_i \times S_j) \qquad (5)$$

where *P* is electric polarization, constant A_0 is determined by the spin exchange and spin-orbit interaction, e_{ij} is the vector connecting neighbouring spins S_i and S_j. According to the equation above, the polarization is dependent on the clockwise or counter clockwise spin order. Generally, the non-collinear magnetic structures can be divided in the four types (Fig. 2.26 b-e).[34]

In addition, lattice distortion is observed by Kimura et al when spins turned into spiral ordering, which can also induce ferroelectricity. However, it is neglected in spin-current model. Then, the Dzyaloshinskii–Moriya (DM) model (Fig. 2.27) was proposed by Sergienko and Dagotto:[69]

$$H_{DM} = D_{ij} \cdot (S_i \times S_j) \quad (6)$$

where D_{ij} is DM vector proportional to $\mathbf{x} \times \boldsymbol{r}_{12}$, x is the shift of the oxygen ion from this line and r_{12} is a unit vector along the line connecting the neighboured magnetic ions 1 and 2 (Fig. 2.27 a). This model is a correction to the superexchange interaction by considering the spin-orbit coupling. The DM interaction is common in none-collinear magnetic order. For example, the weak ferromagnetism of $LaCu_2O_4$ is caused by the DM interaction (Fig. 2.27b).[70] According to the formula (15), the DM interaction of magnetic cations in clockwise or counter clockwise spin order will push the oxygen ions in the direction perpendicular to the chain of Mn^{3+}-O-Mn^{3+} (Fig. 2.27c).[69] Thus, the ferroelectricity in magnetic materials with spiral spins order origin from the contribution of polarization in both spin-current model and DM model. However, it is still not clear which model is in dominated.

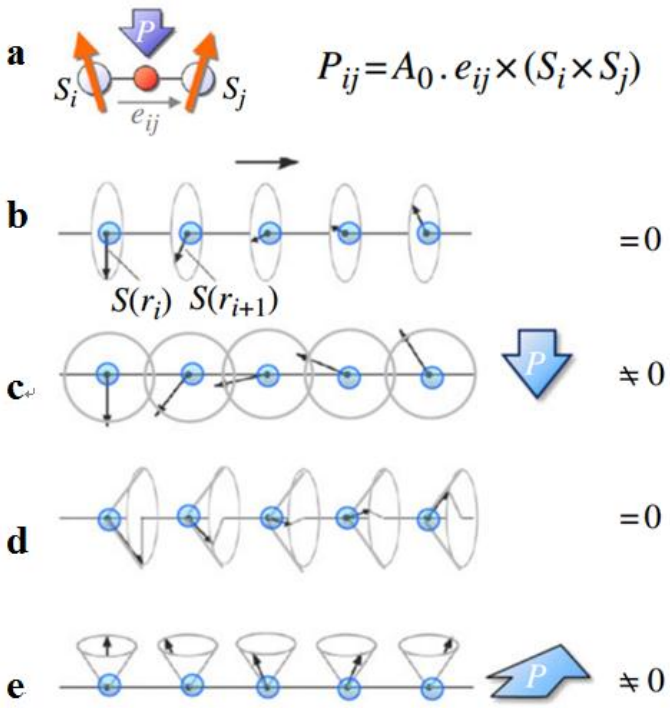

Fig. 2.26 Schematic illustrations of types of none-collinear spin order (a) spin-current model, (b) proper screw, (c) cycloidal, (d) longitudinal-conical and (e) transverse-conical magnetic structures.[34]

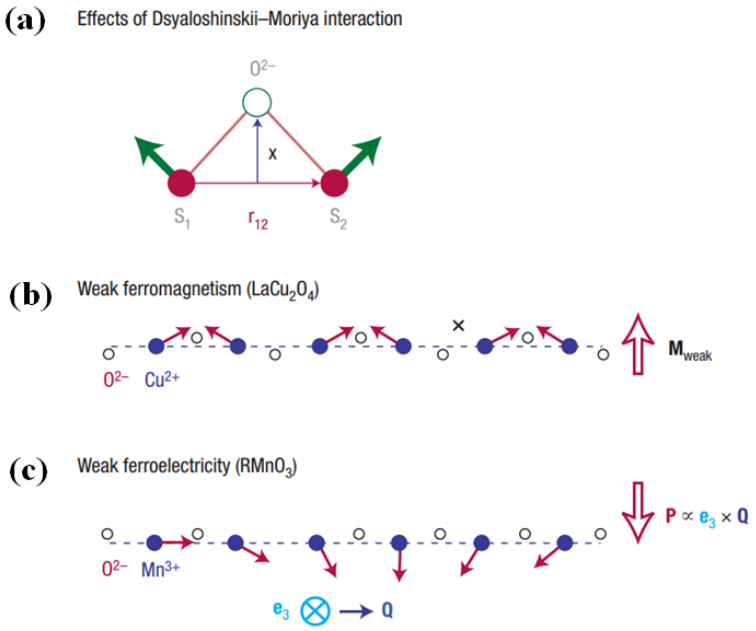

Fig. 2.27 (a) DM interaction, (b) Weak ferromagnetism in $LaCu_2O_4$ results from the DM interaction. (c) DM interaction in RMnO3 with spiral spin state, which induce polarization perpendicular to the chain.[71]

2.4 Aurivillius phase structured materials

Bismuth layer structure ferroelectric materials (BLSFs) were found by Aurivillius in 1949 and named as Aurivillius phase materials. Some of BLSFs exhibit excellent polarization fatigue resistance, long polarization retention and very low leakage currents, which make them to be excellent candidate of non-volatile ferroelectric random access memories. $SrBi_2Ta_2O_9$ and $Bi_{3.25}La_{0.75}Ti_3O_{12}$ are outstanding materials for ferroelectric random-access memory (FRAM).[3,20,21]

2.4.1 General formula and crystal structure

The general chemical formula of Aurivillius phases is $Bi_2A_{m-1}B_mO_{3m+3}$, or more conveniently $(Bi_2O_2)^{2+}(A_{m-1}B_mO_{3m+1})^{2-}$, where the A site can be occupied by large 12-fold-coordinated cations such as Na^+, K^+, Ca^{2+}, Sr^{2+}, Pb^{2+}, Ba^{2+}, Ln^{3+}, Bi^{3+}, Y^{3+}, U^{4+}, Th^{4+}, … etc., and the B site by 6-fold-coordinated cations such as Fe^{3+}, Cr^{3+}, Ga^{3+}, Ti^{4+}, Nb^{5+}, Ta^{5+}, Mo^{6+}, W^{6+}, …etc.[72] The integer *m* corresponds to the number of sheets of corner-sharing BO_6 octahedra forming the perovskite blocks. The bismuth layer structure ferroelectrics consist of alternative stacks of $(Bi_2O_2)^{2+}$ layer and perovskite-like $[A_{m-1}B_mO_{3m+1}]^{2-}$ blocks along the crystallographic *c*-axis, for example, $Bi_4Ti_3O_{12}$ as shown in Fig. 2.28.[73]

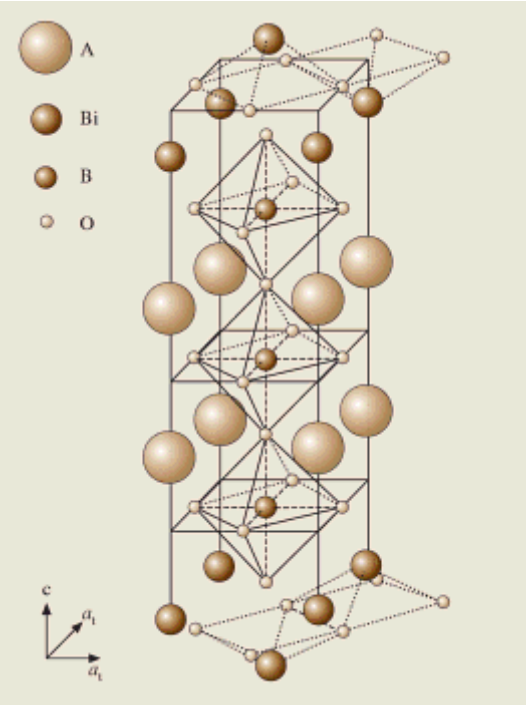

Fig. 2.28 Schematic diagram of half of the unit cell of crystal structure of an Aurivillius compound with m = 3. The cell axes shown are those corresponding to tetragonal structure above T_c.[73]

2.4.2 Phase transition and spontaneous polarization

Most of the Aurivillius phases are tetragonal (space group I4/mmm) above their Curie points (T_c) (Fig. 2.29) and orthorhombic when the materials are cooled below T_c (Fig. 2.30).[74,75] The lattice distortion appeared during the phase transition. Generally, the lattice distortion of BLSFs include the rotation about *a* and *c*-axis (Fig. 2.31) and atomic movement in (100) and (001) plane (Fig. 2.32). As a result of rotation about the c axis, the unit cell doubled in *a*-*b* plane and the lattice parameter *a* and *b* of the room temperature orthorhombic cell are approximately $\sqrt{2}$ times and at 45° to the prototype tetragonal lattice parameters (approximately 0.38 nm).[76]

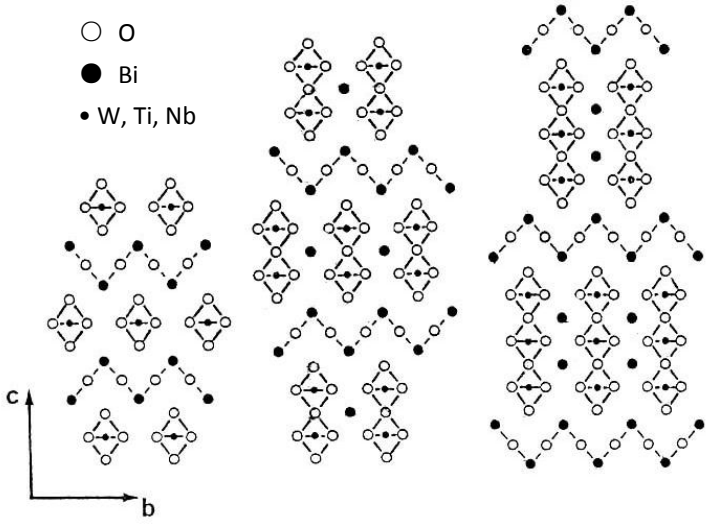

Fig. 2.29 Paraelectric phase of Bi_2WO_6 (m=1); Bi_3TiNbO_9 (m=2); $Bi_4Ti_3O_{12}$ (m=3).[74]

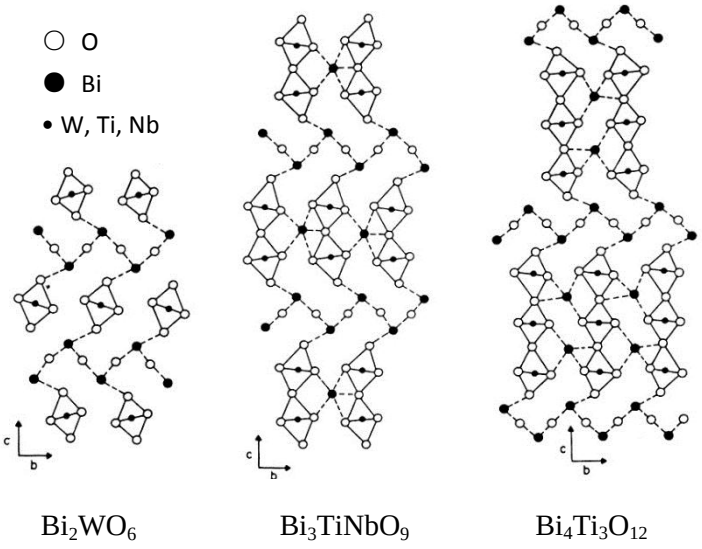

Fig. 2.30 Ferroelectric phase of Bi_2WO_6 (m=1); Bi_3TiNbO_9 (m=2); $Bi_4Ti_3O_{12}$ (m=3).[75]

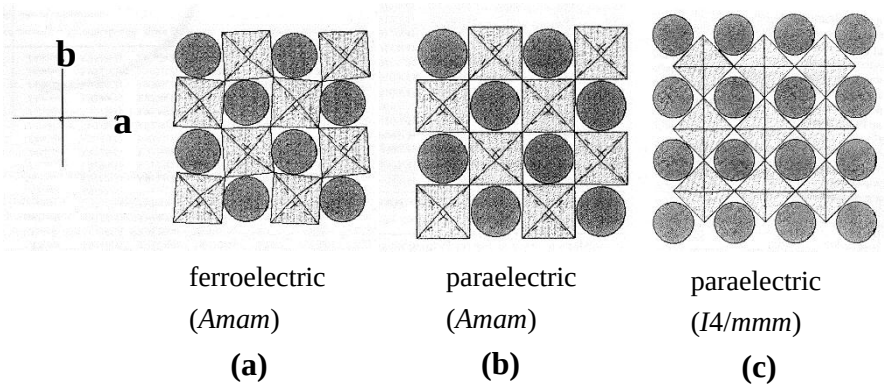

Fig. 2.31 Oxygen octahedral rotation during the ferroelectric-paraelectric phase transition.[77]

The spontaneous polarization arises from both the rotation of the oxygen octahedra and displacements of the ions. However, the polarization caused by displacement of ions along *a*-axis is in dominated.[78,79] For examples, the polarization is along *a*-axis in even layers of BLSFs such as $SrBi_2Ta_2O_9$.[80] The displacements of ions along *a* axis respect to the paraelectric phase cause the spontaneous polarization. Conversely, the displacement along *b* and *c*-axis do not contribute to the polarization due to the presence of glide and

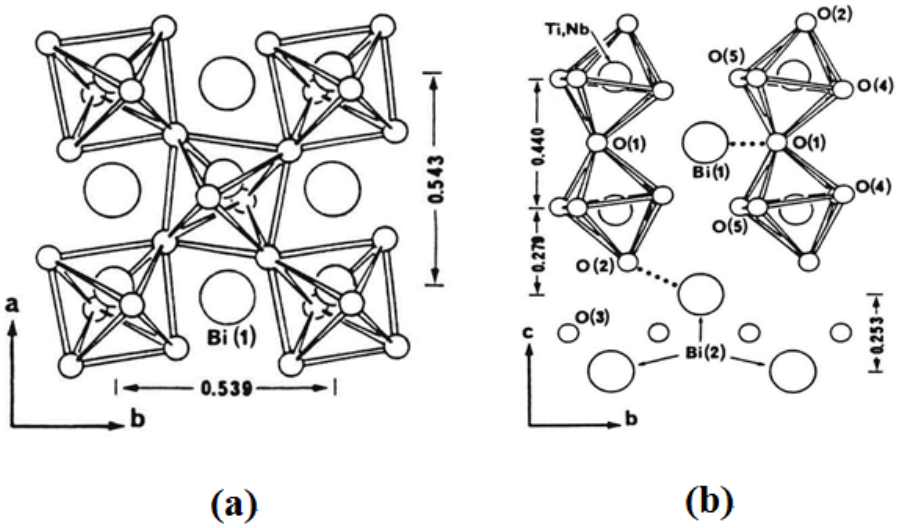

Fig. 2.32 (a) Atomic movement in (001) plane: the Nb, Ti atoms are shifted along the polar axis *a*, (b) atomic movement in (100) plane: elongation of Bi(1)−O(1) bond and Bi(2)−O(2) along c axis.[75]

mirror planes which showed in Fig. 2.33.[81] For odd layers of BLSFs, there is an additional small component of polarization along the *c*-axis, for example, 4 μC/cm^2 along the *c*-axis in $Bi_4Ti_3O_{12}$.[82]

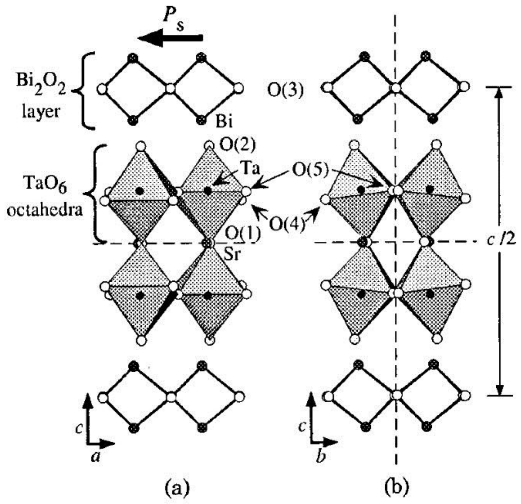

Fig. 2.33 (a) *a*−*c* and (b) *b*−*c* projections of the crystal structure of $SrBi_2Ta_2O_9$. Dashed lines perpendicular to the *b* and *c* axes represent glide and mirror planes, respectively.[81]

Different from the perovskite ferroelectric, the structural cause of ferroelectricity is not only the off-centre displacement of B-site atoms but also the *a*-axis displacement of Bi atoms in the perovskite A sites with respect to the chains of TiO_6.[83] Thus, the spontaneous polarization of BLSFs can be calculated using AKJ model:[84,85]

$$P_s = \sum_i \frac{m_i \Delta x_i Q_i e}{V} \quad (7)$$

where m_i is the site multiplicity, Δx_i is the atomic displacement along the a-axis from the corresponding position in the tetragonal structure, $Q_i e$ is the ionic charge of the ith constitute ion, and V is the volume of the unit cell. The spontaneous polarization of $CaBi_2Nb_2O_9$ and Bi_3NbTiO_9 has been calculated using this model (Fig. 2.34) which matches the experiment data in references very well.[84,86]

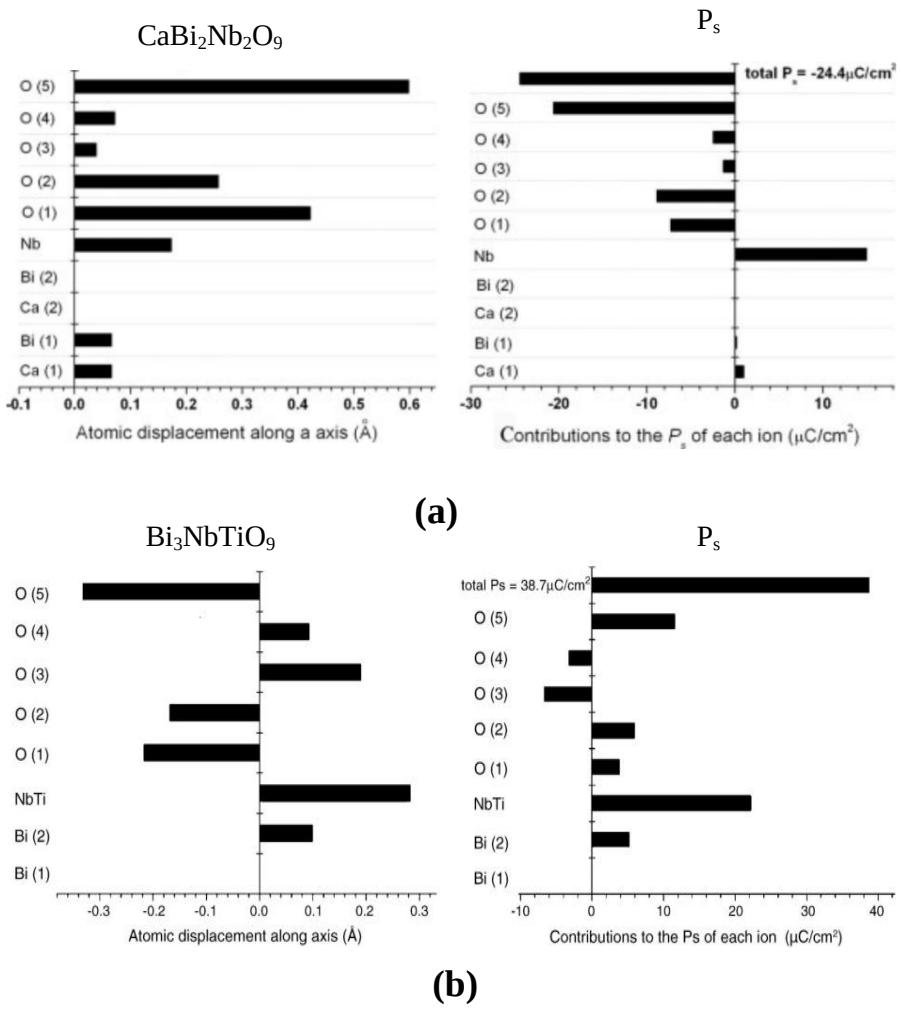

Fig. 2.34 Schematic graph of: ion displacement and contribution to the total spontaneous polarization Ps of each ion of (a) $CaBi_2Nb_2O_9$ and (b) Bi_3NbTiO_9.[84,85]

2.4.4 Curie temperature

The Curie temperatures of BLSFs are related to the lattice distortion which can be described by the tolerance factor: $t = (r_A+r_O)/[\sqrt{2}\,(r_B+r_O)]$, where r_A, r_B and r_O are the radius of A-site, B-site and oxygen ions. The smaller the tolerance factor is, the larger the lattice distortion and the higher Curie point of the BLSFs are. The Curie points of

$Me^{2+}Bi_2TaO_9$, $Me^{2+}Bi_2NbO_9$ and $Me^{2+}Bi_4Ti_4O_{15}$ (Me = Ba, Sr and Pb) increase with the decrease of radius of A-site ions which is showed in Fig. 2.35.[87]

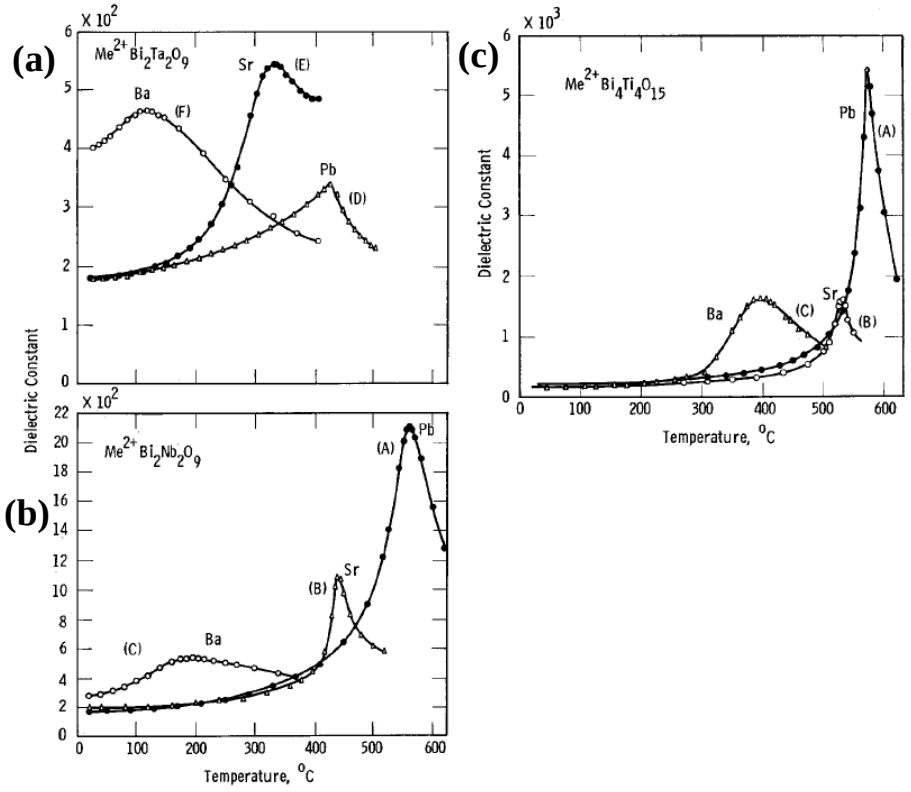

Fig. 2.35 Temperature dependent of dielectric constant of (a) $Me^{2+}Bi_2TaO_9$, (b) $Me^{2+}Bi_2NbO_9$, (c) $Me^{2+}Bi_4Ti_4O_{15}$, Me = Ba, Sr and Pb.[87]

2.4.3 Domain structure

For the even layer of BLSFs, the space group changed from paraelectric *F4/mmm* to ferroelectric $A2_1am$ in which three symmetry elements (the fourfold axis, twofold axis, and translation vector (1/2 1/2 0)) are lost. Therefore, there should exist five types of domain walls, namely: (1) the 90 °domain wall, (2) 180 ° domain wall, (3) antiphase

boundary (APB), (4) APB combined with 90 °domain wall, (5) APB combined with 180 ° domain wall. Most of these domain walls have already been identified in $SrBi_2Ta_2O_9$ by TEM (Fig. 2.36).[88]

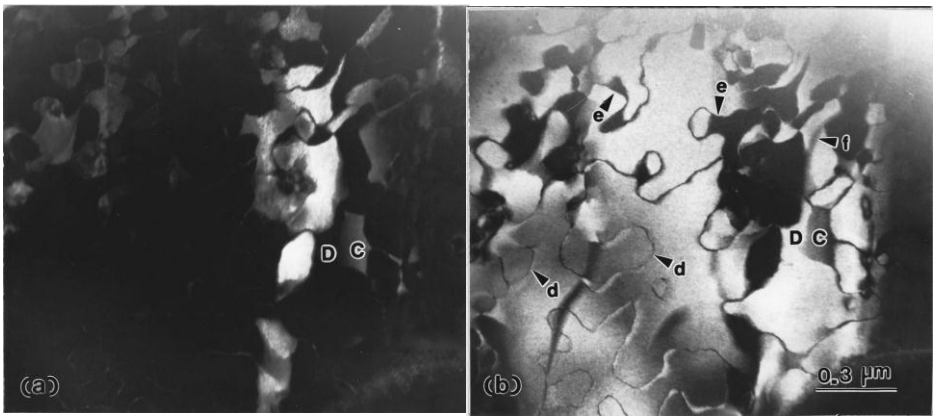

Fig. 2.36 Two dark-field images obtained from two (300) superlattice reflections showing the APB marked by ‘‘d,’’ 180° domain wall by ‘‘f,’’ APB combined with the 90° domain wall by ‘‘e,’’ and the 90° domain wall between the two regions C and D in $SrBi_2Ta_2O_9$.[88]

For odd layers of BLSFs, the additional polarization along c axis makes the domain walls more complex compare to the domain walls in even layers of BLSFs. For examples, the polarization along *a* axis and *c* axis of single crystal $Bi_4Ti_3O_{12}$ are about 50 $\mu C/cm^2$ and 4 $\mu C/cm^2$, respectively. The figure 2.37 shows all the possibilities of domain walls in $Bi_4Ti_3O_{12}$.[89]

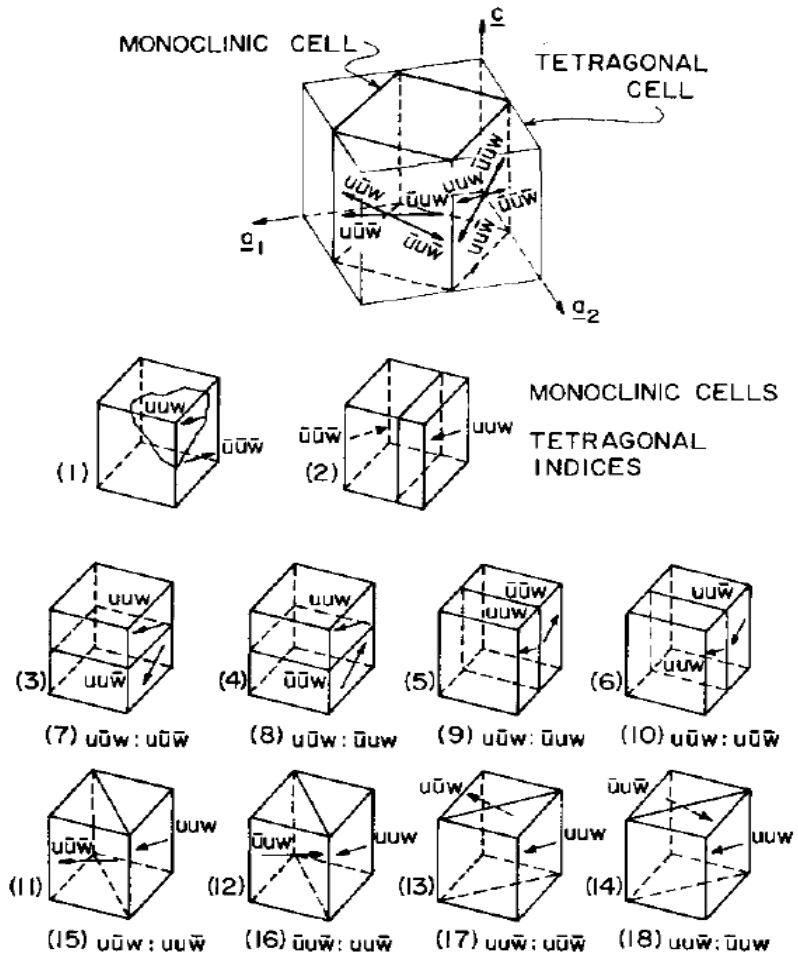

Fig. 2.37 Domain wall possibilities of $Bi_4Ti_3O_{12}$. 1-2:180 °domains walls, 3,4,7,8 and 11-18: 90 °domains parallel to a-b plane, 5,6,9,10: 90 °domains parallel to a(b)-c plane.[89]

The ferroelectric 90 ° domains and 180 ° domains were also found in $Bi_4Ti_3O_{12}$ single crystal using piezoelectric force microscopy (Fig. 2.38).

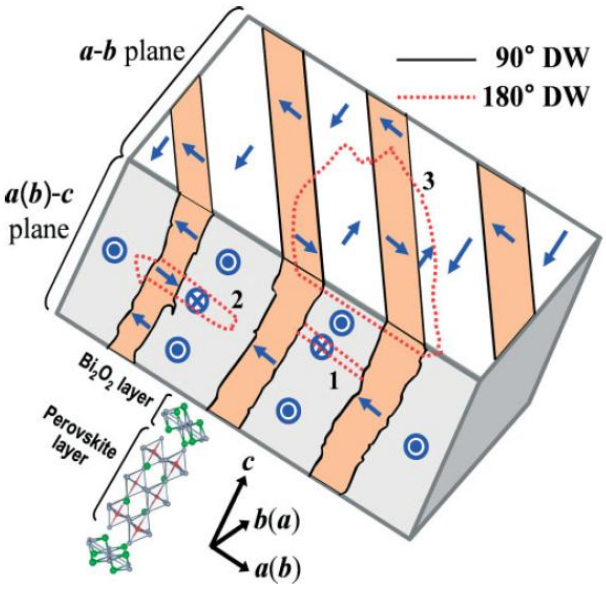

Fig. 2.38 Schematic image of the 3D domain structure in BIT singe crystal. "1", "2", and "3" indicate 180° domains.[90]

2.4.4 Relaxor behaviours in BLSFs

Relaxor ferroelectrics have two different characters compare to normal ferroelectrics. One is the broad T_m (defined as the temperature of the max dielectric permittivity) peak of the temperature dependent of permittivity. The other one is frequency dispersion of T_m. The temperature (T_m) of the dielectric constant shifted to higher temperature with the increase of frequency (ω), which is a character of relaxor behaviour. The relationships of ω, T_m and T_f can be fitted using Vogel-Fulcher equation:

$$\omega = \omega_0 \exp\left(\frac{-T_0}{T_m - T_f}\right) \quad (8)$$

where ω_0 is the attempt angular frequency of the dipoles, T_0 is the equivalent temperature of activation energy ($E_a = kT_0$, where k is the Boltzmann`s constant) for the relaxation process, T_f is freezing temperature.[86] It is generally considered that the

relaxor behaviour is due to the fluctuation of chemical compositions and local polar nanoregions (PNR) which can be explained by the random site model and superparaelectric model.[91,92] The fluctuation of chemical compositions is caused by the random distribution of different ions in the same site. As a consequence, local areas in nano scale with different chemical compositions obtain different Curie temperatures, which caused the wide scale of transition temperature and PNR. The polarizations of PNR are unstable in high temperature due to the thermal fluctuation. When temperature decreases below a freezing temperature (T_f), the polarizations of PNR are stable and can be changed to micro domain with DC field. The relaxor behaviour is widely researched in $Pb(B'_xB''_{1-x})O_3$ perovskite structure materials such as $Pb(Mg_{1/3}Nb_{2/3})O_3$.[93] The relaxor behaviour is also observed in BLSFs such as $BaBi_2Nb_2O_9$, $PbBi_2Nb_2O_9$, $Bi_{4-x}La_xTi_3O_{12}$ (x>1), $BaBi_4Ti_4O_{15}$, $Ba_2Bi_4Ti_5O_{18}$ et al, which is attribute to the cation disorder between Bi^{3+} ions of Bi_2O_2 layers and A-site ions (Ba^{2+}, Pb^{2+} and La^{3+}).[94-99] Figure 2.39 shows the temperature dependent of dielectric permittivity of $BaBi_2Nb_2O_9$, $BaBi_4Ti_4O_{15}$ and $Ba_2Bi_4Ti_5O_{18}$.

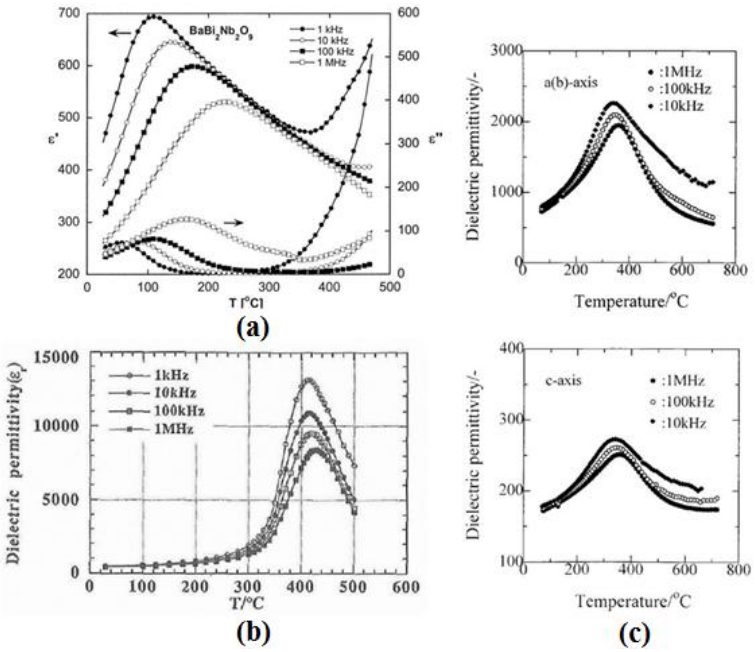

Fig. 2.39 Temperature dependent of dielectric permittivity of (a) $BaBi_2Nb_2O_9$, (b) $BaBi_4Ti_4O_{15}$ and (c) $Ba_2Bi_4Ti_5O_{18}$.[97-99]

2.4.5 Anisotropic ferroelectricity in textured BLSFs

The grain shape of BLSFs is disk-like and the direction of thickness is along *c*-axis. Additional, the polarization of BLSFs is mainly in *a*-*b* plane. Therefore, most of the contribution of polarization in conventional sintered BLSFs ceramics is cancelled due to the random orientation of the disk-like grains (Fig. 2.40a), which lead to a much smaller polarization compare to the single crystal. In order to obtain large polarization, textured BLSFs can be prepared by SPS (Fig. 2.40b and c).

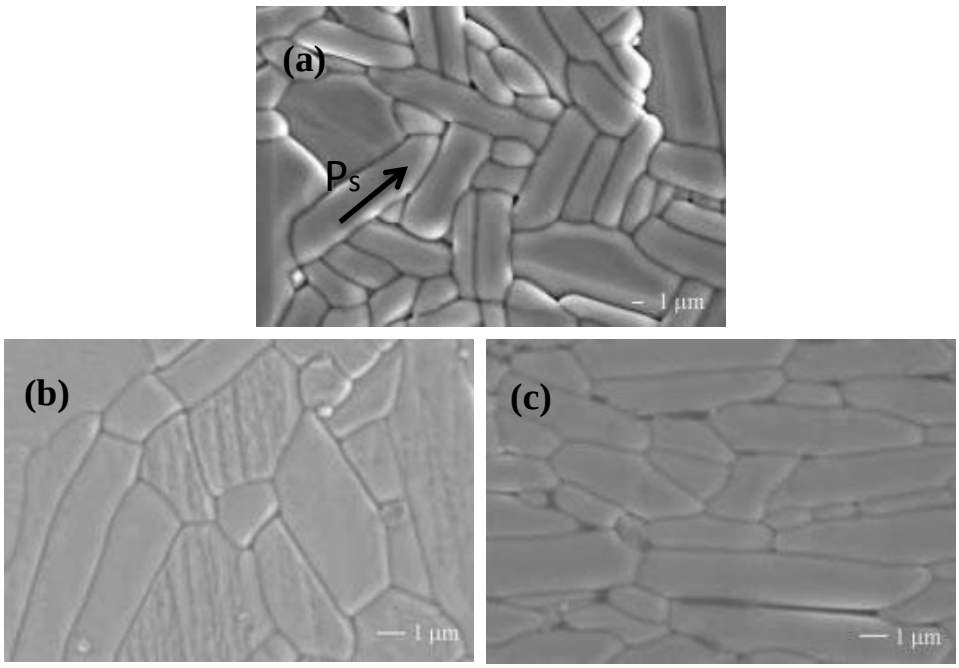

Fig. 2.40 SEM images of $CaBi_2Nb_2O_9$ (a) conventional sintered sample, (b) normal of surface parallel to SPS force direction [//] and (c) normal of surface perpendicular to SPS force direction [⊥].[84]

Figure 2.41 shows the *I-E* and *P-E* loops of textured $Bi_{3.25}La_{0.75}Ti_3O_{12}$. The peaks in *I-E* loops indicate the ferroelectric domain switch. The P_s[⊥] ~ 19.1 μC/cm^2 is much larger than the P_s[//] ~ 3μC/cm^2. The dielectric permittivity ε[⊥] and D[⊥] are larger than ε[//] and D[//], which shows a highly anisotropic character (Fig. 2.42).[100] The piezoelectric constant d_{33}[⊥] is much larger than d_{33}[//] (Fig. 2.43).

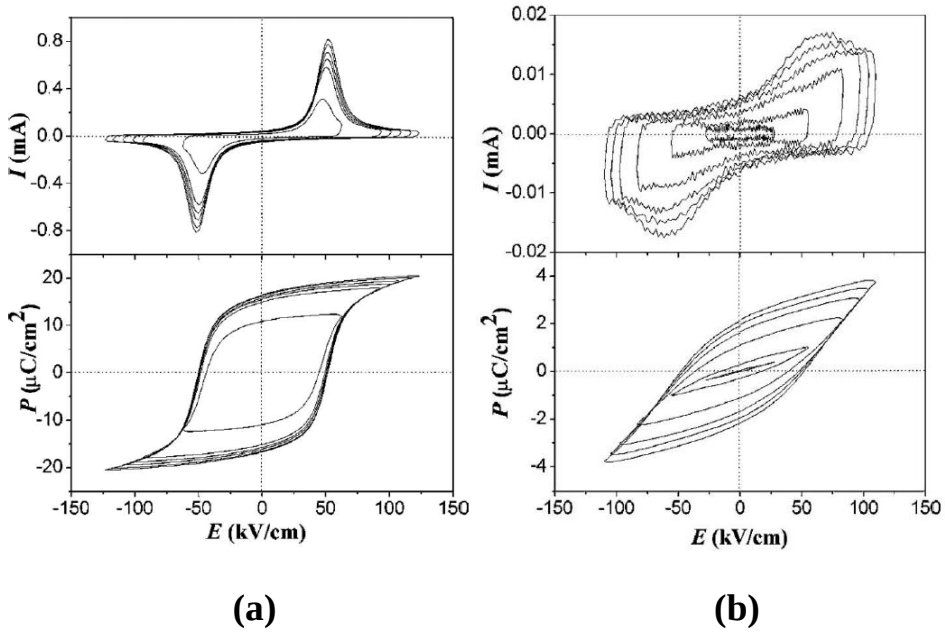

Fig. 2.41 *I*−*E*, *P*−*E* hysteresis loops of grain-orientated BLT ceramics at various electric fields at 10 Hz: (a) [⊥], (b) [//].[100]

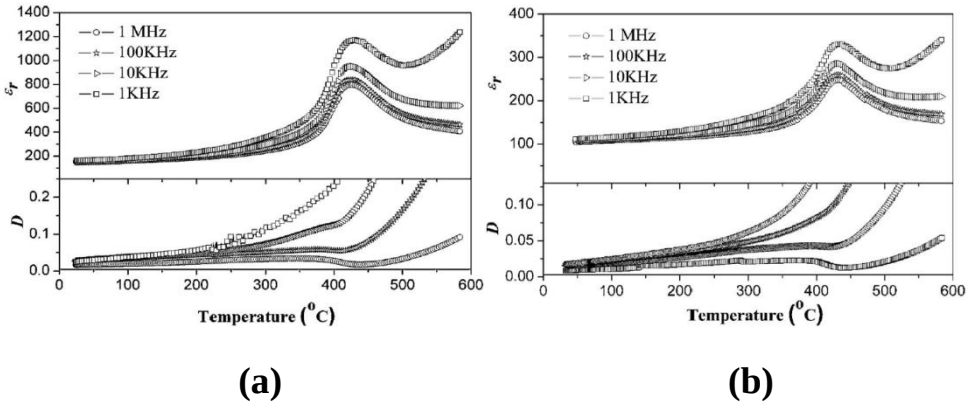

Fig. 2.42 Temperature dependant of dielectric permittivity and loss of BLT: (a) [⊥], (b) [//].[100]

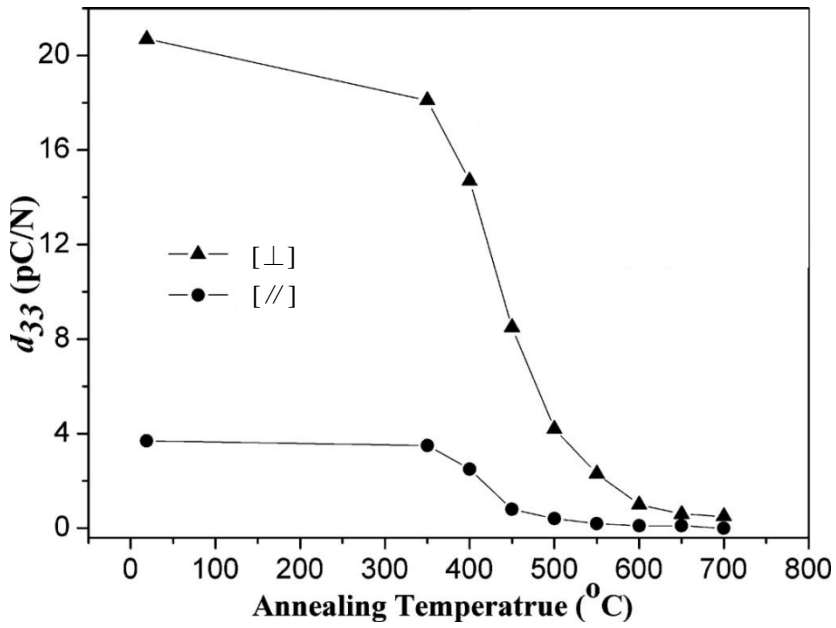

Fig. 2.43 Temperature dependence of d_{33} of BLT in [⊥] and [//] directions.[100]

2.5 Bismuth layer structured multiferroics

In1967, the simultaneous ferroelectric and antiferromagnetic behaviour are reported in $Bi_5FeTi_3O_{15}$ (m=4), $Bi_6Fe_2Ti_3O_{18}$ (m=5) and $Bi_9Fe_5Ti_3O_{27}$ (m=8) by combining one mole of $Bi_4Ti_3O_{12}$ and m moles of $BiFeO_3$.[101] The Neel temperature increases with the layer numbers m, for example $Bi_5FeTi_3O_{15}$ (T_N ~ 80 K) and $Bi_6Fe_2Ti_3O_{18}$ (T_N ~ 160 K).[102] Then magnetoelectric effect of $Bi_5FeTi_3O_{15}$ is reported about 0.1 mV $cm^{-1}Oe^{-1}$ at 77 K.[10] The antiferromagnetic is caused by the superexchange interaction of Fe^{3+}-O-Fe^{3+}. In 2009, the magnetization is significantly improved by replacing parts of Fe^{3+} ions by Co^{3+} ions due to the ferrimagnetic exchange of Fe^{3+}-O-Co^{3+}. The measured M_r is about 3.9 memu/g and the magnetic Curie temperature is also increase to 345 °C (Fig. 2.44).[11]

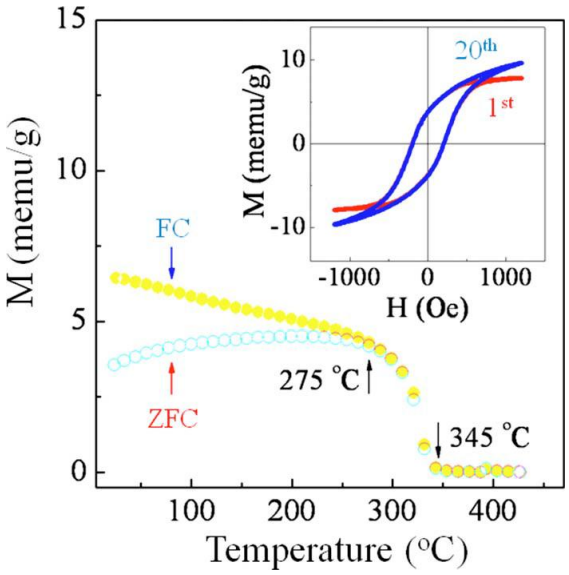

Fig. 2.44 FC and ZFC magnetization curves of the BFCT sample.[11]

It is reported that La substitution can help to decrease the ferroelectric coercive field of $Bi_4Ti_3O_{12}$ and improve the magnetization of $BiFeO_3$ by increasing the canting angle of Fe^{3+}-O-Fe^{3+}. Then, $Bi_{3.25}La_{0.75}Ti_3Fe_{0.5}Co_{0.5}$ is prepared by Mao et al. The M_r is about 25.5 memu/g and magnetic Curie temperature is 487 K (Fig. 2.45).[103]

In the following years, room temperature multiferroic behaviours have been reported in other BLSFs with transition metal ions (Cr^{3+}, Mn^{3+} and Co^{3+}) substitutions.[104-106] However, there is still debate about the origin of the magnetism which may be come from the very small parts of magnetic second phase that are below the resolution of XRD. The second phase is reported to be the mixture Co_2FeO_4 and $CoFe_2O_4$ ($Co_{3-x}Fe_xO_4$) spinel ferrites (Fig. 2.46).[107] The dark regions are the secondary phase and the different elements content are marked by the different colour lines. Until 2013, a magnetic control of ferroelectric domain switch at room temperature are reported in film of $Bi_6Ti_{2.8}Fe_{1.52}Mn_{0.68}O_{18}$, which proves the intrinsic multiferroic of BLSFs.[12] Parts of

the ferroelectric domains (marked by the circle) are totally changed by applying an in-plane external magnetic field (Fig. 2.47).

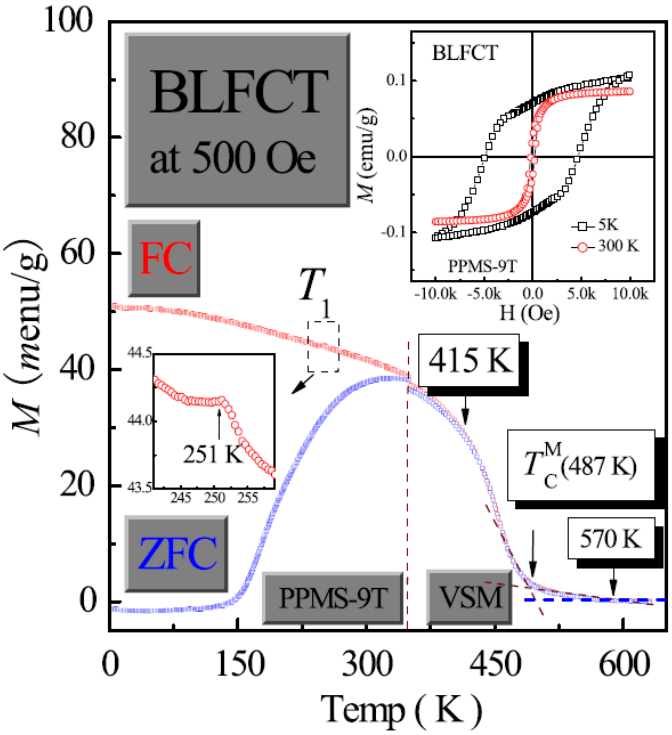

Fig. 2.45 FC and ZFC magnetization curves of the BLFCT samples, Inset: field dependence of magnetization at 5K and 300K for BLFCT samples.[103]

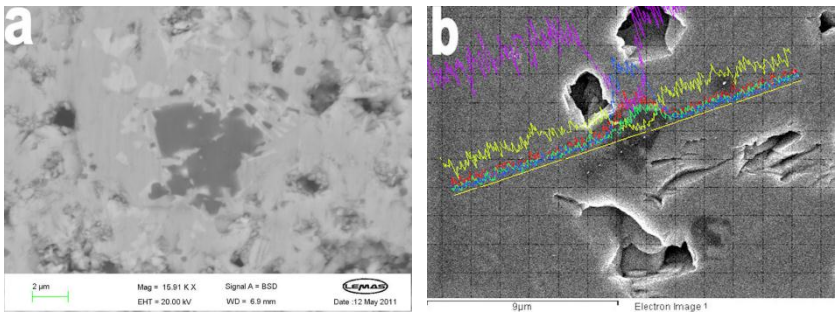

Fig. 2.46 EDS image of Second phase in the BFCT ceramics prepared by (a) conventional method and (b) molten salt method (the colour lines are the signals of EDX,).[107]

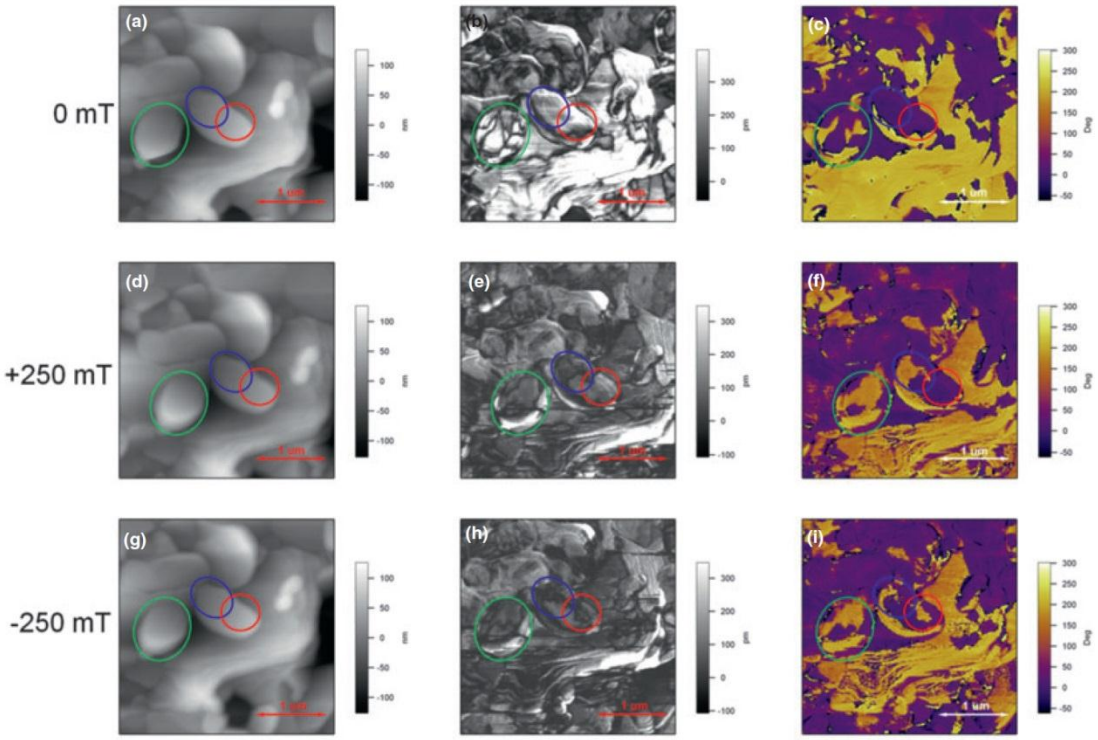

Fig. 2.47 Representative images of B6TFMO thin films: (a) topography; (b) vertical PFM amplitude; and (c) vertical PFM phase under 0 mT (0.9 Oe) H field; (d) topography; (e) vertical PFM amplitude; and (f) vertical PFM phase under +250 mT (+2501 Oe) H field; and (g) topography; (h) vertical PFM amplitude; and (i) vertical PFM phase under 250 mT (2501 Oe) H field.[12]

Chapter III Experiment and Procedure

A number of characterization methods including XRD, neutron diffraction; SEM, PFM, P-E measurement, T_c measurement, and SQUID-VSM were applied to measure the crystal structures, microstructures, ferroelectric, dielectric and magnetic properties. The details of those characterization methods will be given in the later sections.

3.1 Spark plasma sintering

The raw powders were mixed using ball milling machine. Then, the mixture powders were calcined at box furnace in the air. The calcined powders were sintered using SPS furnace showed in Fig. 3.1a. Two-step SPS sintering method was used to prepare the textured samples (Fig. 3.1b). In the first step the powders were enclosed by carbon paper and put into a Φ20mm graphite die. After that the Φ20mm bulk sample was put into a Φ30mm and sintered at the temperature 100 °C higher than the temperature in first step. In this step, the grains would grow and orient perpendicular to the press direction. Then the textured bulk samples were annealed in air at the temperature which was 100 °C lower than the sintering temperature to remove the carbon contamination and oxygen defects caused by the reduced atmosphere during SPS sintering.

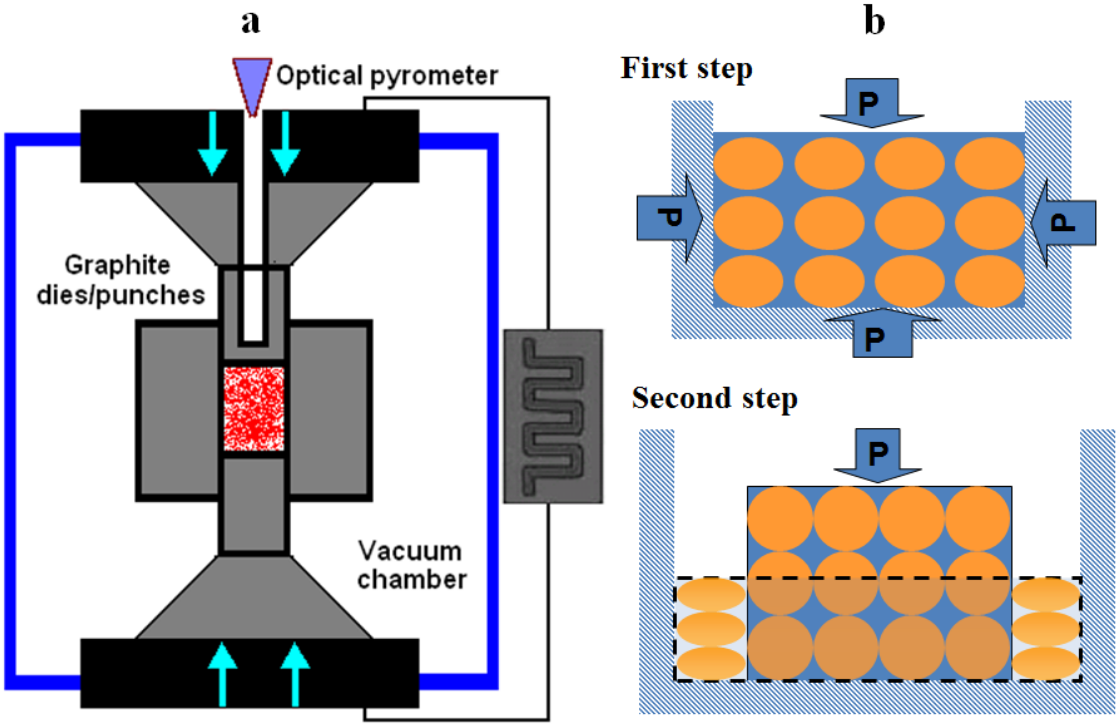

Fig. 3.1 (a) Schematic of SPS furnace, (b) fabrication of texture ceramics using two step SPS method

3.2 Characterisations

3.2.1 Crystallographic structure characterisation

X-ray diffraction (XRD) is widely used to identify the crystal structure and phase of materials. The theory of XRD is based on Bragg`s law:

$$2d\sin\theta = n\lambda$$

Where:

d = Distance between the diffracting planes

θ = incident angle

n = integer

λ = wavelength of the beam

In this work, all the XRD data were measured by PANalytical X`Pert Pro diffract meter with a Cu-Kα radiation (λ = 1.5418 Å). The crystal structure parameters were refined by the Rietveld method using the General Structure Analysis System (GSAS) softer ware.[108]

The Lotgering orientation factor was used to estimate the texture structure of the materials:

$f = \frac{P-P_0}{1-P_0}$, $P = \frac{\sum I(0\ k\ 0)}{\sum I(h\ k\ l)}$, and $P_0 = \frac{\sum I_0(0\ k\ 0)}{\sum I_0(h\ k\ l)}$

where P and P_0 are the fraction of intensities of all *(0 k 0)* planes to that of all diffraction peaks in the oriented samples and random oriented samples, respectively.[109]

The measurement principle of neutron diffraction is also based on the Bragg Equation which is similar to the XRD. However, Neutron diffraction showed more advantages on magnetic structure of materials based on the neutron scattering compare to XRD. This method is also more sensitive to the light elements due to the interaction between neutrons and atomic nucleus. Neutrons have a spin and are able to interact with magnetic moments. Therefor neutron diffraction can be used to identify the magnetic structure of materials. In this work, all neutron diffraction data were measured in ISIS WISH and HRPD instruments.

3.2.2 Density measurement

The densities of the bulk samples were measured based on the Archimedes principle. The density was calculated using the following equation:[110]

$$\rho = \frac{m_1 \rho_0}{m_2 - m_3}$$

Where m_1 is the mass of the dry sample in air; m_2 is the mass of the sample after soaking in water; m_3 is the mass weighed while the sample is immersed in water; ρ_0 is the density of water. Normally $m_1 = m_2$ for samples with nearly fully dense or only closed pores.

3.2.3 Microstructure characterization

(i) Scanning electron microscopy (SEM)

The surface morphology of the grain orientated ceramics was measured using a scanning electron microscopy (FEI Inspect-F, Hillsboro, OR, USA). The bulk samples for SEM measurement were polished using silicon paper and diamond suspension, and then thermally etched at 20 to 100 °C below their sintering temperature for 10 to 20 min to etch the grain boundary. All the samples were coated with gold (for SEM) or carbon (for EDX) to make them conductive.

(ii) Piezoresponse force microscopy (PFM)

PFM was used to measure the ferroelectric domain structure based on the piezoelectricity character of ferroelectric material. PFM is performed in a contact mode

using a conducting AFM probe which enables to apply an AC bias-voltage on sample. When the tip is in contact with the sample surface, the local electrostriction is detected as the first-harmonic component of the cantilever deflection $\Delta z = d_{33} V_{AC} \cos(\omega t + \theta)$, where d_{33} is the vertical piezoelectric constant and V_{AC} is the applied AC voltage. The phase θ is used to record the orientation of electric polarization in vertical direction. When the electric polarization of the sample is in the same direction (P^+) with the applied electric field, θ = 0, which is showed in Fig. 3.2a. Conversely, when the electric polarization is in the opposite direction with the electric field, θ = 180 (Fig. 3.2b). The ferroelectric domains were measured using NT-MDT (Ntegra systems) atomic force microscope.

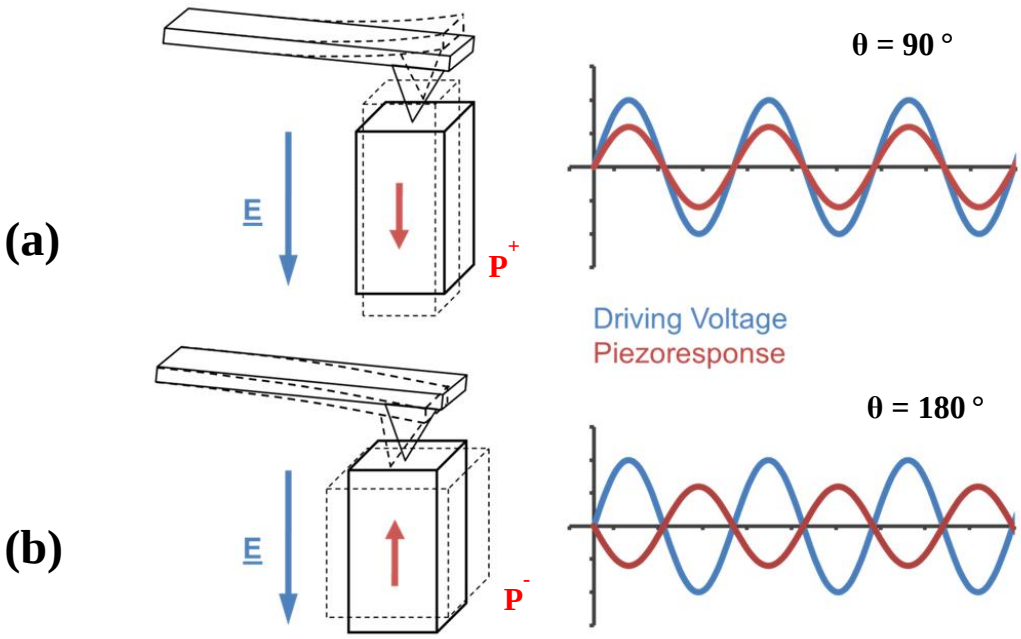

Fig. 3.2 A schematic demonstrating the piezoresponse of the electric polarizations (a) P^+, (b) P^-.

3.2.4 Electrical measurement

The textured bulk disk-like samples were cut into slices and coated with platinum paste (Gwent Electronic Materials Ltd, C2011004D5) as electrodes and burned at 900 °C for 30 min.

Figure 3.3 shows the schematic graph of the setup of the high temperature dielectric and loss measurement. The temperature dependence of dielectric constants and losses of ceramics were measured using an LCR meter (Agilent 4284A) which is connected to a high temperature tube furnace (Leton, LTF 16/--/180, T_{max} = 1600 °C). The accuracy of the temperature was calibrated using a reference sample with a known Curie temperature (T_c = 1210 °C) such as $LiNbO_3$.

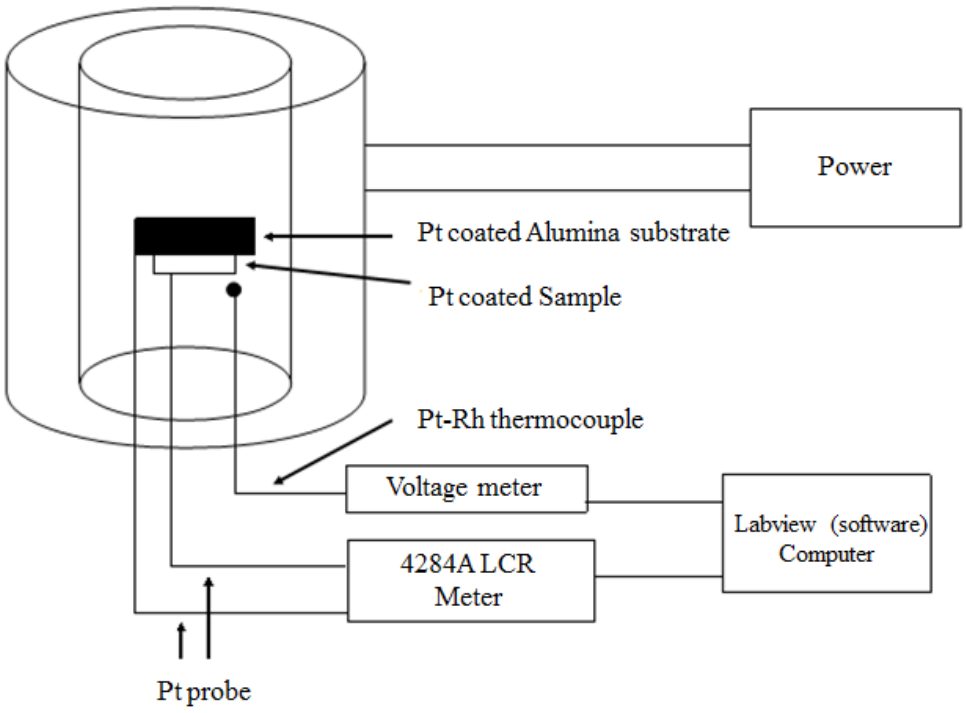

Fig. 3.3 Schematic graph of the setup of the high temperature dielectric and loss measurement

Ferroelectric polarization-electric field (P-E) and current-electric field (I-E) hysteresis loops were measured using a ferroelectric hysteresis measurement tester (NPL, UK) Samples were measured in silicon oil environment at room temperature under a triangular wave voltage up to 10 kV in 10 Hz. The *P-I-E* data were collected using software programmed by NPL.

The samples used for piezoelectric constant d_{33} were poled in silicon oil which can be heat up to 200 °C under various DC electric fields up to 20 kV. The d_{33} of the poled samples were measured using a quasi-static d_{33} meter (ZJ-3B PIEZO d_{33} meter, Institute of Acourstics Academia Sinica, China).

3.2.5 Magnetic measurement

Superconducting quantum interference device (SQUID) is a very sensitive magnetic meter which can be used to measure extremely small signal based on the theory of Josephson Effect. Josephson junction is consisting of two superconductors connected by an ultra-thin insulator. In Josephson junction, the electron can pass through the barrier due to the quantum tunnelling effect. The voltage of the junction is zero when the current is below a critical value (I_c) which is very sensitive to the external magnetic field. The critical current varies periodically with increase of the external magnetic field. Direct current SQUID (DC SQUID) consists of two parallel Josephson junctions (Fig. 3.4). Interference take place when external magnetic field change and the measured critical current is:[111]

$$I_c = 2i_c \left|\cos \pi \frac{\Phi_a}{\Phi_0}\right|$$

Where i_c is the critical current, Φ_a is the flux within the ring and Φ_0 is the flux quantum. A bias current is applied to the junction and the current signal can be converted to voltage signal. One period of the voltage variation corresponds to an increase of flux quantum.

Magnetization – magnetic field (*M-H*) hysteresis loops and zero field cooling/field cooling curves (ZFC/FC) were measured using superconducting quantum interference device magnetometer (Quantum Design, a model MPMS (SQUID) VSM).

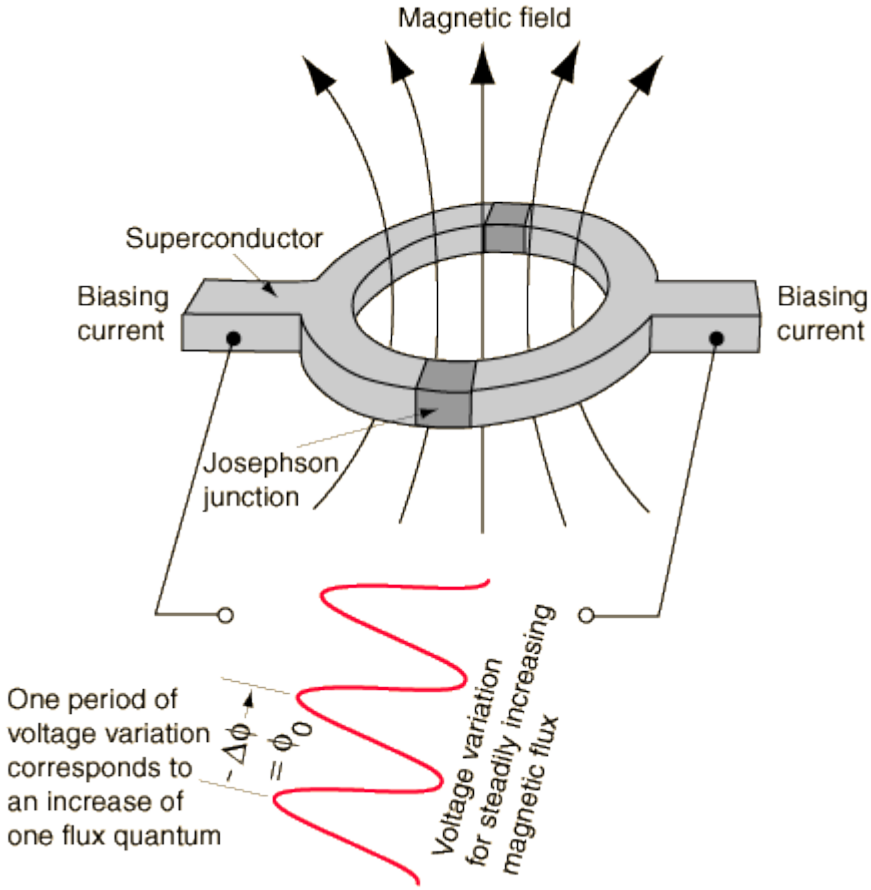

Fig. 3.4 Schematic diagram of DC SQUID.[111]

Chapter IV Investigation of Aurivillius compounds $Bi_3Nb_{1+2x}Fe_xCo_xTi_{1-2x}O_9$

4.1. Introduction

Aurivillius phase materials have potential applications in high-temperature electro-mechanical transducing devices due to the high Curie temperature, low dielectric dissipation factor and high anisotropy.[84,100,112] In addition, Aurivillius phase materials with $m \geqslant 4$ have been reported to be multiferroics such $Bi_5FeTi_3O_{15}$, $Bi_6Fe_2Ti_3O_{18}$ et al. However, there are few researches about the multiferroic properties of Aurivillius materials with $m<4$. Bi_3NbTiO_9 (BNT) is a member of the BLSF family with two layered structure ($m = 2$). The restriction of polarization of Aurivillius materials with two layered structure in a-b plane caused the low piezoelectric activity and low remnant polarization.[113] Ferroelectric properties have been reported to be greatly improved in grain-oriented BLSF ceramics by using spark plasma sintering (SPS).[14,84,100]

In this work, $Bi_3Nb_{1+2x}Fe_xCo_xTi_{1-2x}O_9$ ($x = 0.125$ and 0.25) powders were prepared by solid state reaction. The magnetic cations Fe^{3+} and Co^{3+} are used to replace parts of B-site Ti^{4+} to introduce magnetic property. SPS has been employed to produce grain-oriented BNT ceramics in order to improve the ferroelectric and dielectric properties of BNT.

4.2 Experiment

The $Bi_3Nb_{1+x}Fe_xCo_xTi_{1-2x}O_9$ (BNFCT) powders were obtained by a conventional solid state reaction route. BNT powders were mixed using Bi_2O_3, Nb_2O_5, Fe_2O_3, Co_3O_4 and TiO_2 according to the stoichiometry of BNFCT1 (x = 0.125) and BNFCT2 (x = 0.25). The mixed powders were calcined at 900 ℃ for 4 h. The textured ceramics were obtained in a two-step process by SPS, the powders were consolidated at 1000 ℃ for 5 min under a uniaxial pressure of 80 MPa in a graphite die with an inner diameter of 20 mm. Then this dense sample was superplastically deformed at 1080 ℃ for 5 min under a pressure of 50 MPa in a graphite die with a lager inner diameter of 30 mm. In order to remove carbon in SPSed ceramics, sintered samples were annealed at 950 ℃ for 10 h in air. The bulk ceramics were cut perpendicular and parallel to the SPS pressure direction. The crystal structures of the obtained ceramics were determined with XRD using Cu Kα radiation at RT (X'Pert Pro, PANalytical, Almelo, The Netherlands). The surface morphology of the grain orientated ceramics was studied using a scanning electron microscopy (SEM) (FEI Inspect-F, Hillsboro, OR, USA). The ferroelectric I−E (current–electric field) and P−E (polarization–electric field) hysteresis loops were measured using a ferroelectric hysteresis measurement tester (NPL, UK)[114]. The temperature dependence of the dielectric permittivity and loss was measured at different frequencies using an LCR meter (Agilent, 4284A) and a purpose-made furnace. The temperature dependence of magnetization were measured by superconducting quantum interference device magnetometer (Quantum Design, a model MPMS (SQUID) VSM).

4.3 Results and discussions

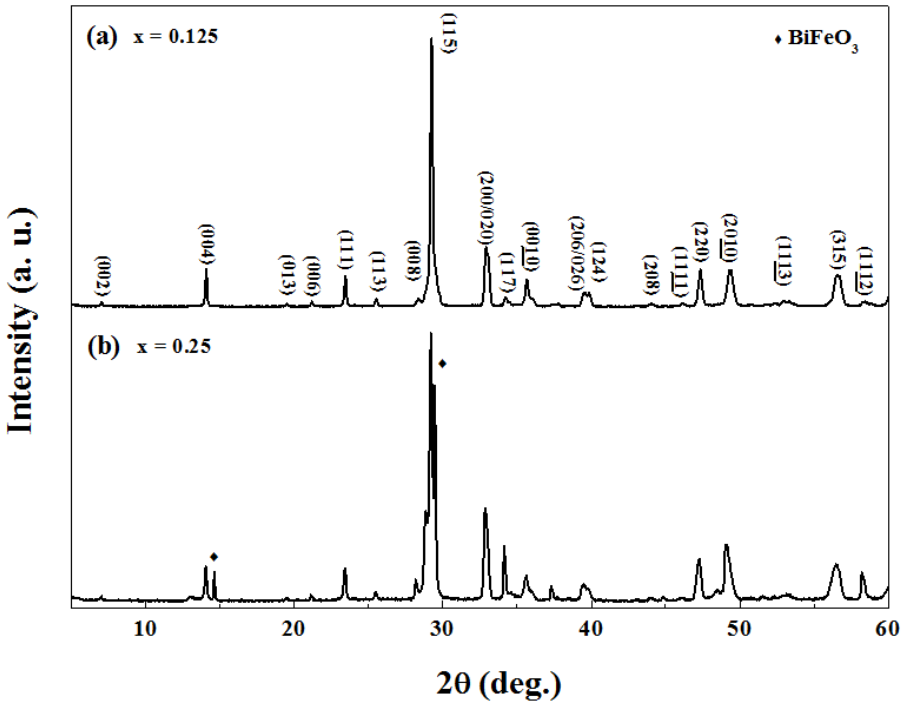

Fig. 4.1 XRD patterns of the BNFCT powders (a) x = 0.125, (b) x = 0.25.

Fig. 4.1 shows the XRD patterns of the BNFCT1 and BNFCT2. BNFCT1 is a single phase bismuth layer-structured Aurivillius compound with an orthorhombic lattice with the space group $A2_1am$ and all the peaks can be indexed by the standard diffraction data (JCPDS No.79-1550). The secondary phase $CoFe_2O_4$ appeared in BNFCT2 with increasing amount of magnetic atoms Fe/Co.

Fig. 4.2 shows the morphology of the textured BNFCT1 ceramics in two directions. The typical Aurivillius plate-like grains with their *a*-*b* axes orientated perpendicularly to the SPS pressure direction were observed in Fig. 4.2.

Fig. 4.3 shows the temperature dependence of the dielectric properties of BNFCT1 measured perpendicular to the SPS pressure direction at three different frequencies. The peak of the dielectric permittivity at about 1155 K corresponds to the ferroelectric Curie

temperature (FE T_c) of BNFCT1. The peak in the inset of Fig. 4.3 shows a dispersion character which is caused by the oxygen vacancy.[115]

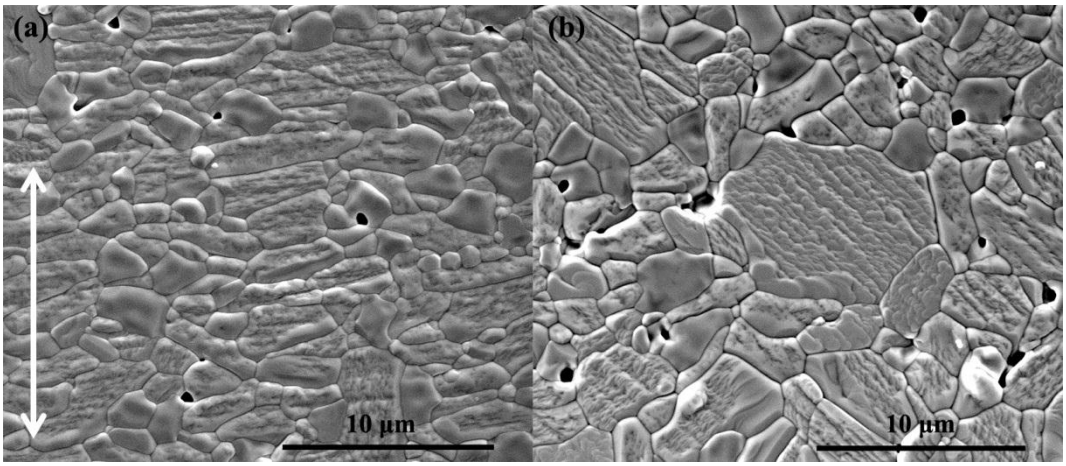

Fig. 4.2 SEM image of the textured BNFCT1ceramics (a) perpendicular to the SPS pressure direction [⊥] and (b) parallel to the SPS pressure direction [//]. The direction of SPS pressure is marked by white arrow.

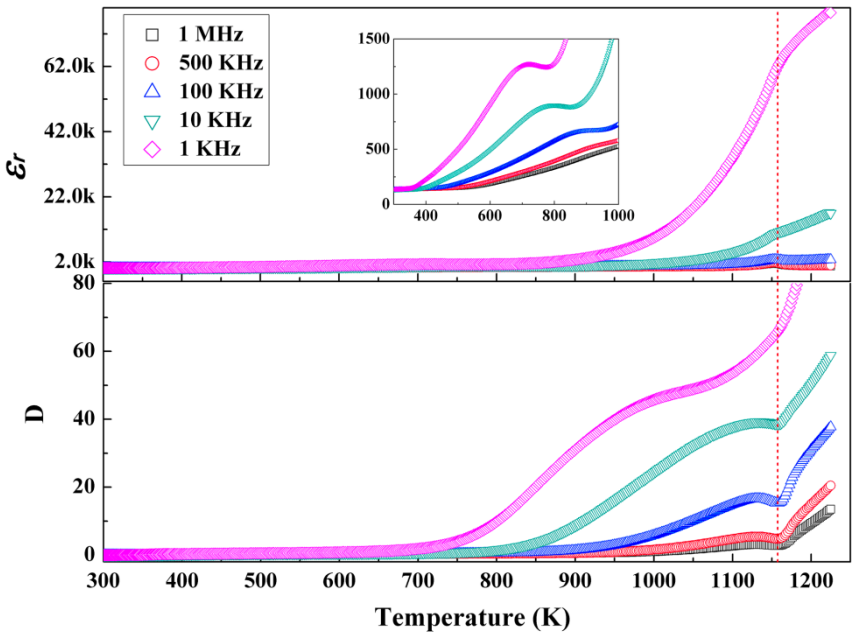

Fig. 4.3 Temperature dependence of the dielectric properties of the textured BNFCT1 ceramics along the direction perpendicular to SPS pressure direction. The inset shows the dielectric peak at about 650 K.

Fig. 4.4 shows the *I-E* and *P-E* hysteresis loops of the grain-oriented BNFCT1 ceramics measured in the direction perpendicular to the SPS pressure direction at RT. The remnant polarization is about 0.8 μC/cm^2. The measured d_{33} ~ 5.6 pC/N of BNFCT1 after polling confirms the ferroelectric character of BNFCT1.

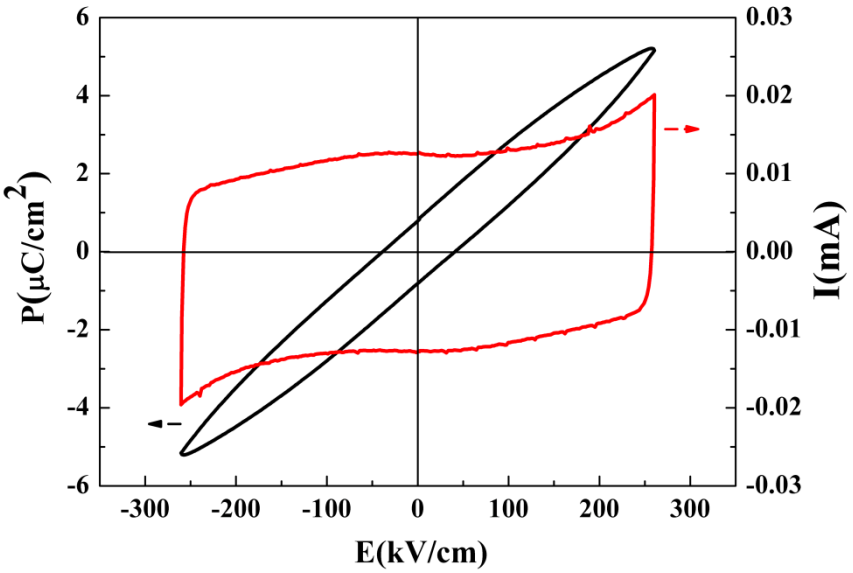

Fig. 4.4 Electric field dependant of polarization and current curves of textured BNFCT1 ceramics along the direction perpendicular to SPS pressure direction.

Fig. 4.5 shows the temperature dependence of the magnetization for BNFCT1 ceramics [⊥] in the zero field cooling (ZFC) and field cooling (FC) model. The ZFC and FC curves have few differences in the whole temperature range from 5 to 300 K, which indicate that BNFCT1 can be a paramagnetic or antiferromagnetic material. In order to make clear the nature of magnetic behaviour, the temperature dependence of the inverse susceptibility ($\chi^{-1} = H/M$) is fitted by the Curie-Weiss law to the magnetic susceptibility, i.e. $\chi_m = C/(T - T_c)$ (Fig. 4.6). The fitting consist with an antiferromagnetic character

which indicate that the superexchange interaction of Fe^{3+}-O-Fe^{3+} and Co^{3+}-O-Co^{3+} are in dominate and the Neel temperature is about 249 K. The magnetization of ZFC/FC curves in the low temperature significantly increased which indicate the existence of paramagnetic behaviour. The paramagnetism of BNFCT1 is caused by the separate magnetic cations Fe/Co with no magnetic interaction with each other due to the large distance between them.

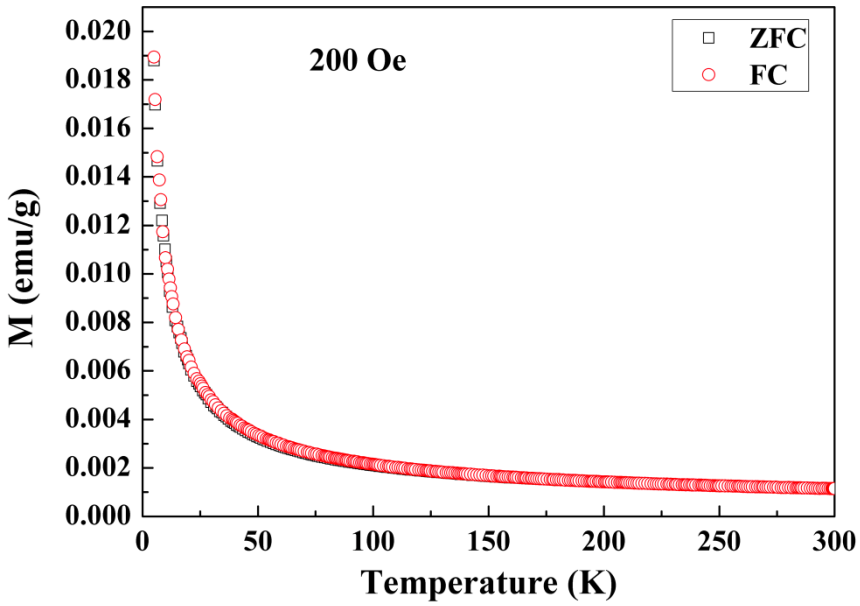

Fig. 4.5 Temperature dependence of the magnetization for BNFCT1 ceramics [⊥] in the ZFC/FC modes measured in H = 200 Oe.

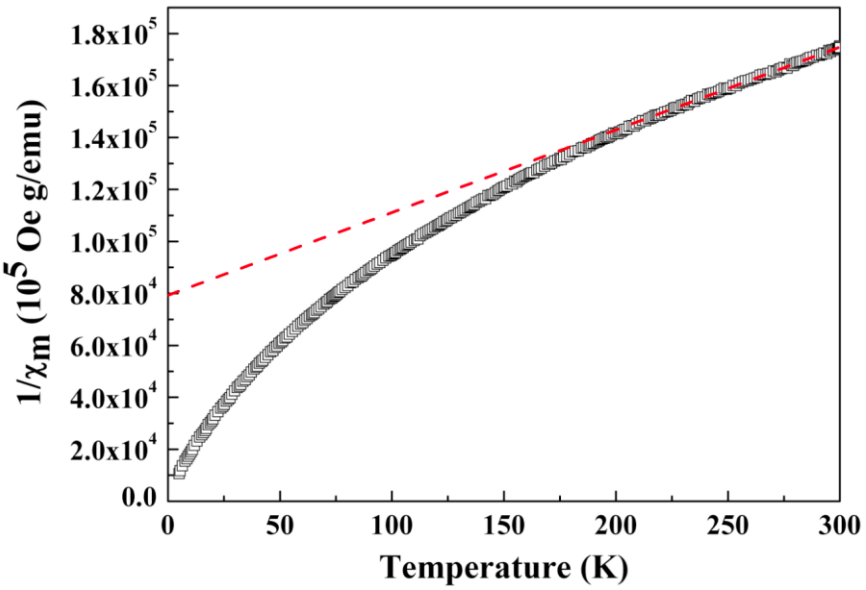

Fig. 4.6 Temperature dependent of inverse susceptibility of BNFCT1.

4.4 Conclusions

In conclusion, the Aurivillius phase $Bi_3Nb_{1.125}Fe_{0.125}Co_{0.125}Ti_{0.75}O_9$ is ferroelectric and paramagnetic at room temperature. The ferroelectric properties were confirmed by the *P-I-E* and temperature dependant of dielectric and loss curves. The T_c is about 1155 K. Paramagnetism is suggested to originate from the separate Fe^{3+}/Co^{3+} ions due to the low concentration of magnetic atoms.

Chapter V Magnetoelectric coupling in single phase Aurivillius material $Bi_{3.25}La_{0.75}Fe_xCo_xTi_{3-2x}Nb_xO_{12}$

5.1 Introduction

Multiferroics, the potential material of the next generation of novel memory device, have attracted much attention of researchers due to the coexistence of ferroelectric and magnetic ordering and magnetoelectric coupling.[6,67,116] Recently, ferroelectric random access memories [FRAM] have achieved fast access speed (5ns) and high density (64 Mb),[117] but they are limited by the need for destructive read and reset operation. Multiferroic (MF) materials offer multistate memory with fast low-power electrical write operation and non-destructive magnetic read operation.[118]

Aside from the potential applications, the fundamental physics of multiferroic materials is rich and fascinating. At present there are very limited single phase MF. The reason is that the conventional mechanism, for cation off-centring in ferroelectrics (which requires formally empty d-orbitals) and the formation of magnetic moments (which usually results from partially filled d-orbitals) are counteracting[5]. Furthermore, all known single phase multiferroic materials are still far beyond practical applications since they exhibit multiferroic properties only at very low temperature, while at room temperature the magnetoelectric effect becomes weak.[65,67,119,120] $BiFeO_3$ is still the only well-known single phase room temperature multiferroic materials.[121] However, even $BiFeO_3$ is far from the application of memory device due to limitation of high electrical conduction.[47]

Therefore, researches on new materials are a pressing need.

In single phase multiferroics, the simultaneous presence of electric and magnetic dipoles does not guarantee strong magnetoelectric (ME) coupling due to the different microscopic mechanisms of ferroelectricity and magnetism and relatively weak interaction with each other. Strong ME coefficients were expected in single phase multiferroics when the same magnetic atoms contribute to ferroelectric polarization and magnetic moment at the same time.[122] Recently, Aurivillius layer structured materials with general formula $(Bi_2O_2)^{2+}(A_{m-1}B_mO_{3m+1})^{2-}$ (m is the number of octahedral layers in the perovskite slab) have attracted many attentions.[11,12,123] These materials are ferroelectric at room temperature and usually have high Curie points.[123] In Aurivillius materials the spontaneous polarization (P_s) originates from the off-centre movement of the ions along *a*-axis. The switching of P_s is mainly restricted in *a*-*b* plane.[14,84] The transition metal elements such as Fe, Cr, Co, and Mn can be accommodated at B-site.[10,124] In this case, the magnetic atoms in B-site are responsible for the both ferroelectricity and magnetism and the magnetoelectric coupling will be probably achieved. $Bi_{3.25}La_{0.75}Ti_3O_{12}$ (BLT), a candidate for non-volatile ferroelectric random access memory (FRAM) because of its good fatigue resistance and large spontaneous polarizations along *a*-axis,[125,126] was selected as our base material. The compositions $Bi_{3.25}La_{0.75}Fe_xCo_xTi_{3-2x}Nb_xO_{12}$ (BFCT100x, x = 0.05, 0.25 and 0.35) were designed based on the following criteria: i) rare-earth La substitution reduces oxygen vacancies in BIT,[21,100] ii) donor Nb substitution can decrease conductivity and balance the charge in presence of Fe/Co substitution.[113]

In this thesis, single phase BFCT25 textured ferroelectric ceramic was prepared using Spark Plasma Sintering. The observed ferromagnetic behaviour was supported by the first principle modelling. Ferroelectric domain switching under magnetic field was observed locally in PFM test at room temperature, which shows magnetoelectric coupling at room temperature in an intrinsic MF single phase Aurivillius material.

5.2 Experiment

Samples preparation.

Raw materials Bi_2O_3 (99.975%), La_2O_3(99.9%), Fe_2O_3(99.9%), Co_3O_4 (99.9%), Nb_2O_5 (99.9%) and TiO_2 (99.8%) were weighed according to the stoichiometric formulae of $Bi_{3.25}La_{0.75}Nb_xFe_xCo_xTi_{3-2x}O_{12}$ (BFCT100x, x = 0.05, 0.25 and 0.35) and then mixed by ball milling for 4 h. The mixed powders were calcined at 900 ℃ for 4 h. The textured ceramics were obtained in a two-step process using SPS. The BFCT powders were consolidated at 825-850 ℃ for 5 min under a uniaxial pressure of 80 MPa in a graphite die with an inner diameter of 20 mm. The dense samples were superplastically deformed at 925-950 ℃ for 5 min under a pressure of 50 MPa in a lager graphite die with an inner diameter of 30 mm. In order to remove carbon in SPSed ceramics, sintered samples were annealed at 800 ℃ for 10 h in air.

Crystal structure characterization.

The bulk ceramics were cut perpendicular to the SPS pressure direction. The crystal

structures of the obtained ceramics were determined with XRD using Cu Kα radiation at RT (X'Pert Pro, PANalytical, Almelo, The Netherlands). The neutron diffraction of the BFCT25 was performed on the Wish instrument at the ISIS facility, Rutherford Appleton Laboratory, UK. The XRD refinement was performed by the collaborator I. Abrahams from the school of chemistry, Queen Mary University of London. The surface morphology of the grain orientated ceramics was studied using a scanning electron microscopy (SEM) (FEI Inspect-F, Hillsboro, OR, USA).

Ferroelectricity characterization.

The ferroelectric $I-E$ (current–electric field) and $P-E$ (polarization–electric field) hysteresis loops were measured using a ferroelectric hysteresis measurement tester (NPL, UK).[114] The temperature dependence of the dielectric permittivity and loss was measured at different frequencies using an LCR meter (Agilent, 4284A) and a purpose-made furnace. The ferroelectric domain morphology was obtained by PFM (NT-MDT Ntegra systems) at 70 kHz with a 10 V AC electric field.

Magnetization characterization.

The magnetization hysteresis loops and temperature dependence of magnetization were measured by superconducting quantum interference device magnetometer (Quantum Design, a model MPMS (SQUID) VSM) at temperature 1.8 K $\leq T \leq$ 1000 K in magnetic field -1 T $\leq H \leq$ 1 T. The magnetic hysteresis loops are corrected to eliminate the paramagnetic background of the separate magnetic atoms with no magnetic interaction.

FMR measurements were performed in a JEOL, JES-FA 300 (X-band at ω=8.969GHz with the power 1mW) spectrometer at room temperature. Magnetoelectric coupling were measured by magnetoelectric measurement system (Quantum Design, Super-ME-II).[127] The samples were measured in a DC magnetic field (*H*) changing linearly with time (0 - 3 kOe), with a superimposed AC magnetic field (H_{ac}) of 5.6 Oe at 1 kHz.

First principle modeling of magnetization.

The first principle modeling was performed by the collaborator Prof. C.L. Jia from Lanzhou University. Our calculations are based on the density functional theory (DFT) as implemented in the Vienna ab initio simulation package (VASP) code with the projector augmented wave (PAW) potentials and the generalized gradient approximation (GGA) due to Perdew, Burke, and Ernzerhof (PBE). The basis set contained plane waves with a kinetic energy cutoff of 500 eV and the total energy was converged to 10^{-6} eV. The geometry of the cluster was optimized without any symmetry constraint until all residual forces on each atom were less than 0.01 eV/Å. A 2*1 supercell is employed in all calculations, which contains 31 Bi atoms (with one substitution La atom), 22 Ti atoms (with two additional Ti atoms were substituted by one Fe and one Co atom) and 96 O atoms. Total energy of the system with two Ti atoms at different sites was substituted by one Fe and one Co atom was calculated to determine the position of the Fe and Co atoms. According to our results (Table 5.1), the Fe and the Co atom was connected through the O atom. The GGA+U method was introduced to take into account the strong correlation. Agreement with experiment was reached once effective U = 2.0 eV and U = 3.0 eV for Fe

and Co atoms, respectively. Based on the correction (U_{Fe} = 2.0 eV and U_{Co} = 3.0 eV), the energy difference between FM and AFM state of the system and exchange parameter between two transition metal sites (L, R) of Fe-O-Fe, Co-O-Co and Fe-O-Co were calculated (Table 5.1).

Table 5.1 Magnetic exchange interactions based on the GGA+U calculations. M_L and M_R are the magnetizations of the two transition metals neighbored to oxygen, respectively. U_L and U_R are the Hubbard corrections of the two transition metals neighbored to oxygen, respectively. DE is the energy difference between FM and AFM state of the system. J is exchange parameter between two transition metals neighbored to oxygen.

M_L-O-M_R	U_L(eV)	U_R(eV)	$M_L(\mu_B)$	$M_L(\mu_B)$	DE (meV)	J(meV)
Fe-O-Fe	1	1	3.216	3.201	137.85	15.08
	2	2	2.840	3.863	84.66	16.38
	2.5	2.5	3.323	-3.310	-13.65	-2.42
	3.5	3.5	3.150	4.010	109.75	18.11
	4.5	4.5	4.105	3.438	63.78	9.20
	5	5	4.279	-4.250	-102.41	-12.46
	6	6	4.362	-4.364	-219.49	-27.39
Co-O-Co	1	1	0.682	-0.701	-168	-344
	2	2	0.818	0.823	7.7	23.13
	3	3	0.982	0.984	45.3	59.89
	4	4	1.266	1.970	52.6	46.01
	5	5	1.552	2.117	16.2	5.02
	6	6	3.187	-3.192	-267.3	-51.73
Fe-O-Co	1	1	2.359	0.037	86.37	120.59
	1	2	3.101	1.024	23.76	13.56

	1	3	2.394	1.890	7.7	2.75
	2	2	2.665	2.845	30.99	10.41
	2	3	2.604	1.868	68.25	29.09

5.3 Results and discussions

Characterization of BFCT

Both BFCT5 and BFCT25 powders except BFCT35 are single phase with an Aurivillius structure (XRD PDF 89-7500). Fig. 5.1 shows the XRD patterns of BFCT5 and BFCT25. Secondary phase BiFeO3 is found in BFCT35 (Figure 5.2). The structure parameters refined by GSAS software can be indexed with an orthorhombic structure (space group B2cb) with lattice constant and the refinement parameters are showed in table 5.2 and table 5.3. The low R_p, R_{wp} and χ^2 values of XRD refinement parameters reveal the good fitting between the experimental and calculated XRD patterns.[108]

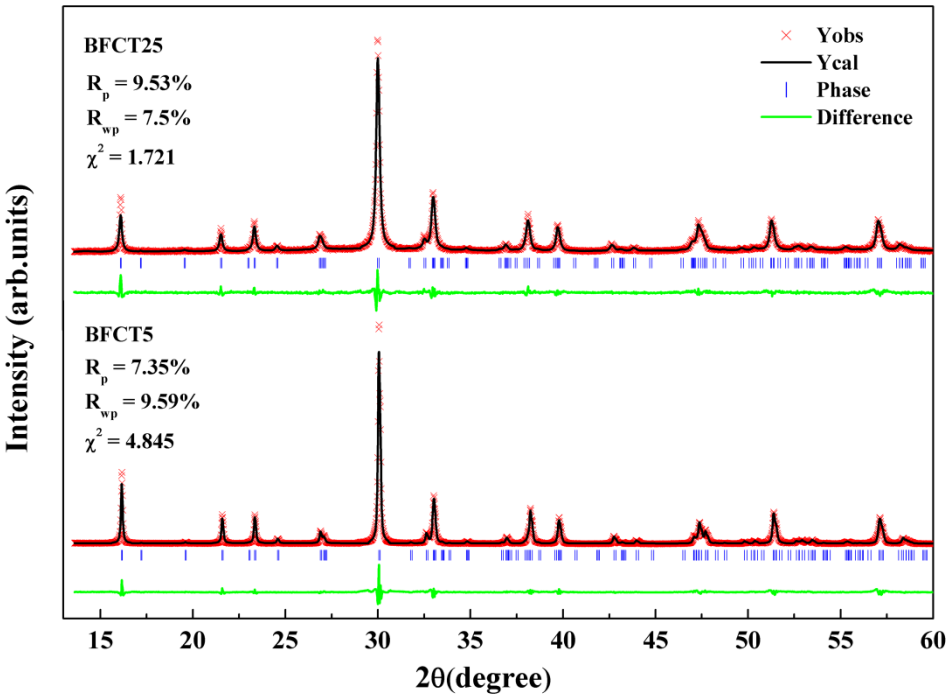

Fig. 5.1 XRD refinement of BFCT5 and BFCT 25 powders.

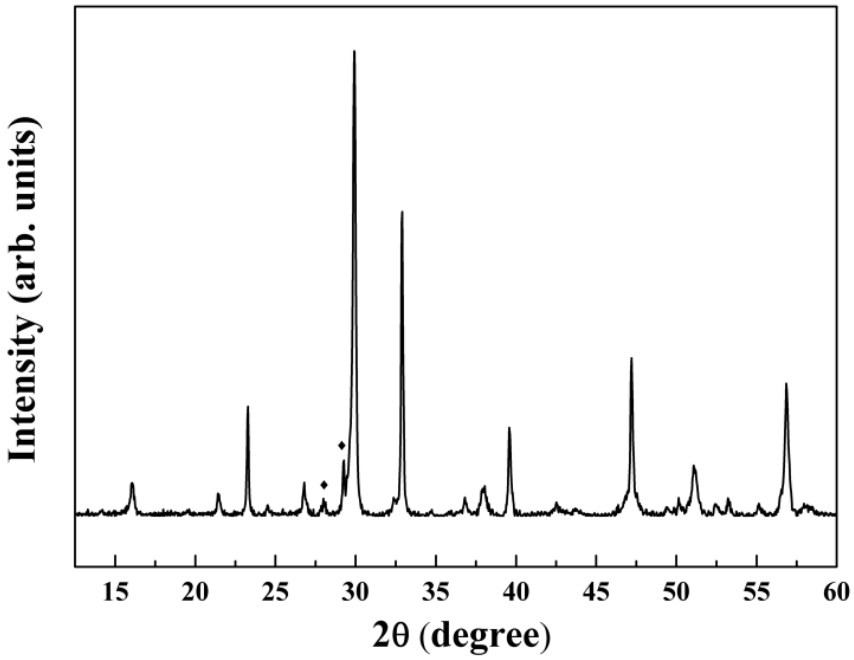

Fig. 5.2 X-ray diffraction pattern of BFCT 35 powder. Secondary phase $BiFeO_3$ is marked by diamond symbol.

Table 5.2 Crystal and refinement parameters of BFCT5 and BFCT25 powers

	BFCT5	**BFCT25**
a (Å)	5.4212	5.4276
b (Å)	5.4289	5.4356
c (Å)	32.9351	33.0482
Volume ($Å^3$)	969.3(2)	975.0(1)
R_p	0.0735	0.0953
R_{wp}	0.0959	0.075
χ^2	0.04845	0.01721

Table 5.3 Refined structural parameters of BFCT5 and BFCT25

Atom	Site	x	y	z	Occ.	U_{iso} ($Å^2$)
BFCT5						
Bi1	8b	0.28865	0.9780(61)	0.06702(5)	0.625	0.028(56)
La1	8b	0.28865	0.9780(61)	0.06702(5)	0.375	0.028(56)
Bi2	8b	0.283(21)	0.0042(5)	0.21145(4)	1	0.025(60)
Ti1	4a	0.2461(3)	0.00000	0.50000	0.9333	0.017(7)
Nb1	4a	0.2461(3)	0.00000	0.50000	0.0167	0.017(7)
Fe1	4a	0.2461(3)	0.00000	0.50000	0.0167	0.017(7)
Co1	4a	0.2461(3)	0.00000	0.50000	0.0333	0.017(7)
Ti2	8b	0.2539(7)	0.983(1)	0.37083(4)	0.9333	0.01775

Nb2	8b	0.2539(7)	0.983(1)	0.37083(4)	0.0167	0.034(4)
Fe2	8b	0.2539(7)	0.983(1)	0.37083(4)	0.0167	0.034(4)
Co2	8b	0.2539(7)	0.983(1)	0.37083(4)	0.0333	0.034(4)
O1	8b	0.5062(78)	0.2252(27)	0.0109(26)	1	0.017(2)
O2	8b	0.5647(68)	0.2443(73)	0.2535(3)	1	0.017(2)
O3	8b	0.3657(68)	0.0295(27)	0.4419(72)	1	0.017(2)
O4	8b	0.3359(53)	1.0157(96)	0.3186(14)	1	0.017(2)
O5	8b	0.5484(86)	0.2118(54)	0.1153(02)	1	0.017(2)
O6	8b	0.5978(51)	0.2489(14)	0.8863(76)	1	0.017(2)
BFCT25						
Bi1	8b	0.13511	0.9765(14)	0.06692(9)	0.625	0.0384(12)
La1	8b	0.13511	0.9765(14)	0.06692(9)	0.375	0.0384(12)
Bi2	8b	0.128(7)	0.0068(18)	0.21135(6)	1	0.0404(10
Ti1	4a	0.099(8)	0.00000	0.50000	0.83333	0.034(4)
Nb1	4a	0.099(8)	0.00000	0.50000	0.08333	0.034(4)
Fe1	4a	0.099(8)	0.00000	0.50000	0.04167	0.034(4)
Co1	4a	0.099(8)	0.00000	0.50000	0.04167	0.034(4)
Ti2	8b	0.112(10)	0.996(5)	0.37108(24)	0.83333	0.034(4)
Nb2	8b	0.112(10)	0.996(5)	0.37108(24)	0.08333	0.034(4)
Fe2	8b	0.112(10)	0.996(5)	0.37108(24)	0.04167	0.034(4)
Co2	8b	0.112(10)	0.996(5)	0.37108(24)	0.04167	0.034(4)

O1	8b	0.418(25)	0.276(27)	0.0079(12)	1	0.019(7)
O2	8b	0.375(33)	0.25(4)	0.2602(10)	1	0.019(7)
O3	8b	0.160(28)	0.093(9)	0.4413(8)	1	0.019(7)
O4	8b	0.106(21)	1.035(14)	0.3179(9)	1	0.019(7)
O5	8b	0.402(33)	0.26(4)	0.1137(16)	1	0.019(7)
O6	8b	0.332(17)	0.164(17)	0.8841(16)	1	0.019(7)

Fig. 5.3 shows the morphology of the BFCT5 and BFCT25 textured ceramics. Plate-like grains oriented perpendicularly to the SPS pressure direction are observed. The high Lotgering orientation factor of BFCT5 (f = 0.72) and BFCT25 (f =0.75) indicate the highly grain-oriented structure. In order to research the Fe/Co substitution in B-site, energy dispersive X-ray analysis (EDX) was employed to scan the grains. According to the results of EDX, magnetic atoms Fe/Co were found in the BFCT grain areas; this suggests that parts of Ti were substituted by Fe/Co.

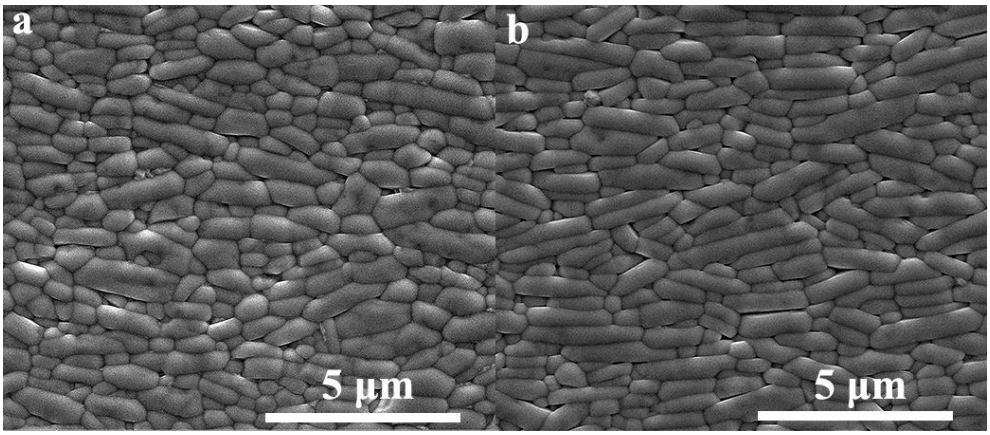

Fig. 5.3 SEM images of (a) BLFCT5 and (b) BLFCT25

Characterization of ferroelectric properties

Fig. 5.4a and 5.4b display the I-E and P-E hysteresis loops of the grain-orientated BFCT5 and BFCT25 ceramics measured at RT in a direction perpendicular to the SPS pressure direction. The occurrence of current peaks in I-E loops implies the ferroelectric domain switching upon field reversal.[128] The maximum value of the remanent polarization (P_r) decreased as the magnetic atoms increasing. The P_r of BFCT5 and BFCT25 are 14.08 μC/cm^2 and 12.43 μC/cm^2 respectively.

Fig. 5.4c and 5.4d show the temperature dependent dielectric properties of BFCT5 and BFCT25 ceramics measured perpendicularly to the SPS pressure. The Curie point (FE T_c) of BFCT5 and BFCT25, as determined from the dielectric peak position, is 638 K and 556 K, respectively. The FE T_c decreases with an increasing amount of the added magnetic atoms. Such behaviour has been observed in other substitutionally modified Aurivillius phase multiferroic and reflects the fact that the trivalent Fe/Co ions replace Ti^{4+} ions at B-sites. The broadening of the T_c peaks is likely caused by the existence of local Fe/Co-rich regions in the structure.

In order to calculate the spontaneous polarization of BFCT25, neutron diffraction was performed (Fig. 5.5). According to the refinement parameters of neutron data in Table 5.5, the value of P_s along an *a*-axis of the ferroelectric BFCT25 was calculated using the AKJ relationship,[129]

$$P_s = \sum_i \frac{m_i \Delta x_i Q_i e}{V} \quad (1)$$

where m_i is the site multiplicity, x_i is the atomic displacement along the *a*-axis from the corresponding position in the paraelectric phase structure, $Q_i e$ is the ionic charge of the

*i*th constitute ion and *V* is the volume of the unit cell. The contribution of each ion to the P_s is illustrated in Fig. 5.6. The total P_s obtained from the model is 34 μC/cm^2.

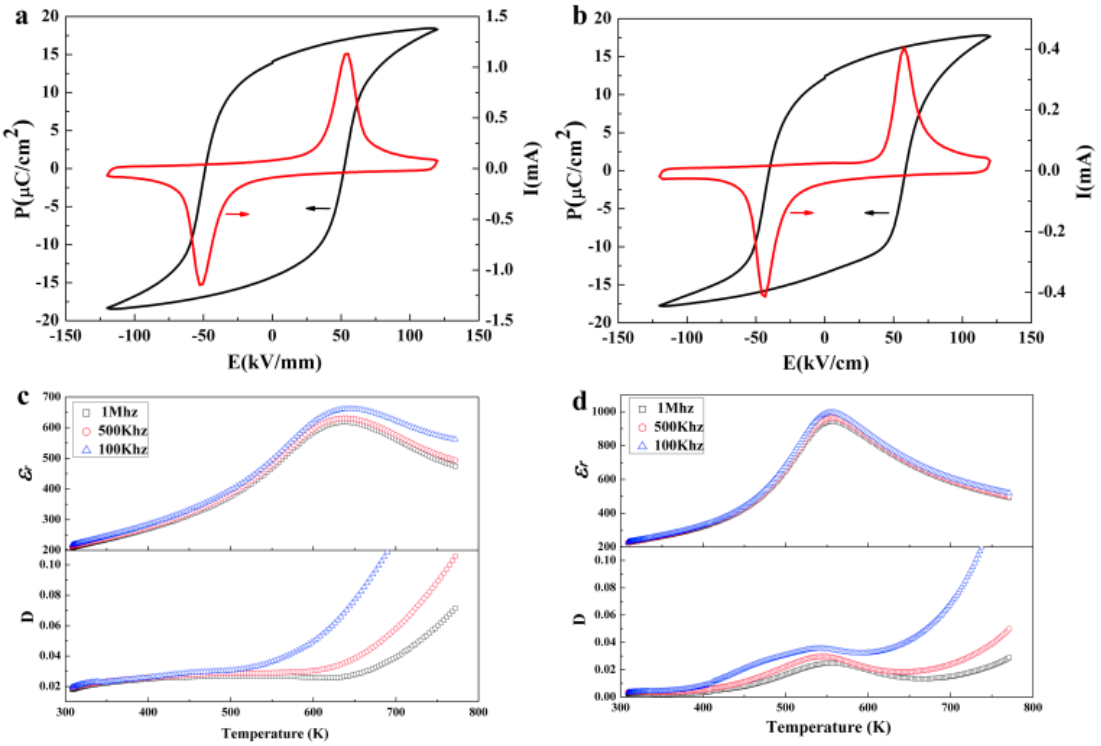

Fig. 5.4 P-I-E loops of BFCT5; (b) P-I-E loops of BFCT25; (c) temperature dependence of dielectric constant and loss of BFCT5; (d) temperature dependence of dielectric constant and loss of BFCT25

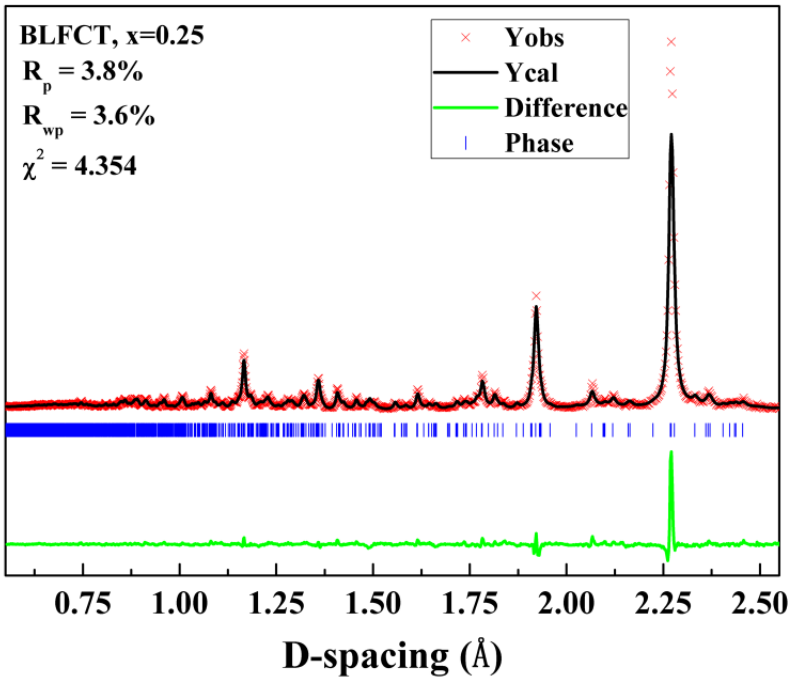

Fig. 5.5 Neutron diffraction refinement of BFCT-0.25 at room temperature

Table 5.4 Neutron diffraction refined structural parameters of BFCT25

Atom	Site	x	y	z	Occ.	U_{iso} (Å^2)
Bi1	8b	0.13511	0.9928(9)	0.06657(4)	0.625	0.0337 (6)
La1	8b	0.13511	0.9928(9)	0.06657(4)	0.375	0.0335 (6)
Bi2	8b	0.1348(20)	0.0187(8)	0.21140(3)	1	0.0294(5)
Ti1	4a	0.105(4)	0.00000	0.50000	0.83333	0.0182(17)
Nb1	4a	0.105(4)	0.00000	0.50000	0.08333	0.0182(17)
Fe1	4a	0.105(4)	0.00000	0.50000	0.04167	0.0182(17)
Co1	4a	0.105(4)	0.00000	0.50000	0.04167	0.0182(17)
Ti2	8b	0.111(4)	0.9931(34)	0.37219(11)	0.83333	0.0182(17)
Nb2	8b	0.111(4)	0.9931(34)	0.37219(11)	0.08333	0.0182(17)

Fe2	8b	0.111(4)	0.9931(34)	0.37219(11)	0.04167	0.0182(17)
Co2	8b	0.111(4)	0.9931(34)	0.37219(11)	0.04167	0.0182(17)
O1	8b	0.4326(27)	0.2648(16)	0.00557(32)	1	0.0209(8)
O2	8b	0.3739(21)	0.2624(20)	0.2498(4)	1	0.0209(8)
O3	8b	0.0951(25)	0.0634(17)	0.44072(21)	1	0.0209(8)
O4	8b	0.0854(25)	0.9755(18)	0.31617(26)	1	0.0209(8)
O5	8b	0.3923(21)	0.2685(22)	0.11215(26)	1	0.0209(8)
O6	8b	0.3473(24)	0.2071(25)	0.87981(26)	1	0.0209(8)

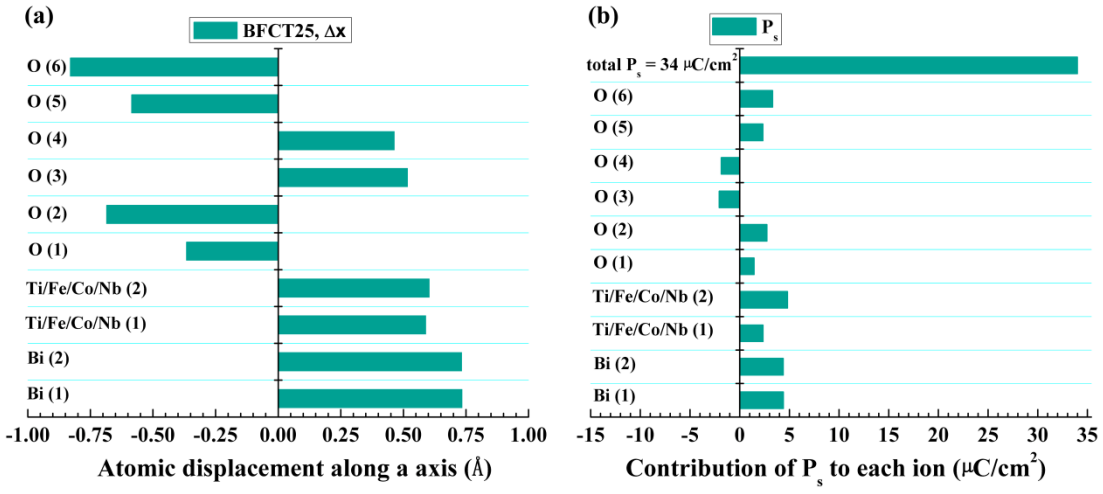

Fig. 5.6 The ionic displacements and (b) the individual contributions of each ion to the total spontaneous polarization to Ps of BFCT25.

Characterization of ferromagnetic properties

Fig. 5.7a shows the magnetization of BFCT5 and BFCT25 ceramics as a function of temperature under a magnetic field of 200 Oe. For the low-doped BFCT5, *M-T* curve

resembles a typical paramagnetic behaviour because of the random substitution of magnetic Fe/Co ions in the ceramics. However, several small humps beyond the paramagnetic background are clearly shown in BFCT25, which implies that certain magnetic ordering develops between (adjacent) transition metal ions in the emerged Fe/Co-rich areas with increasing the doping level.

A clear split between the zero-field-cooled (ZFC) and the field-cooled (FC) modes demonstrates further the ferromagnetic nature of BFCT25 (cf. Fig. 5.8). By fitting the temperature dependence of inverse magnetic susceptibility ($1/\chi_m=H/M$) with the Curie-Weiss law, i.e. $\chi_m = C/(T - T_c)$, three ferromagnetic transitions are found around

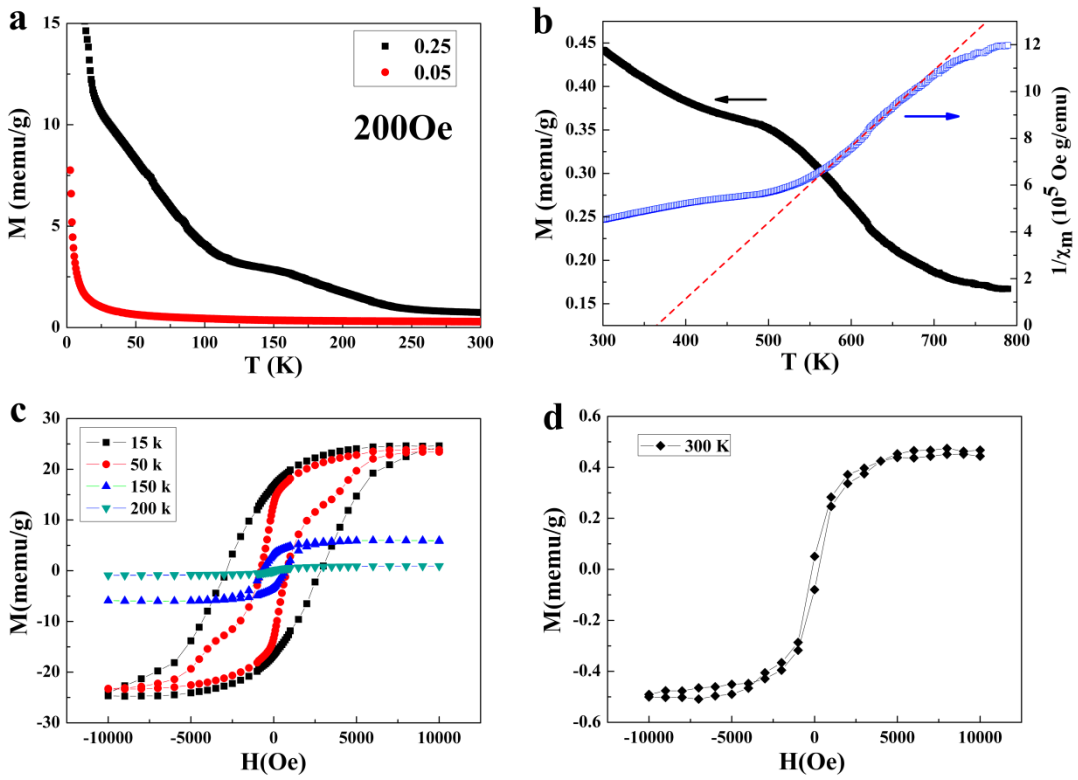

Fig. 5.7 (a) Temperature dependence of magnetization BFCT5 and BFCT25 (5-300 K), (b) temperature dependent of magnetization and inverse susceptibility of BFCT25 (300-800 K), (c) field dependence of magnetization in BFCT25 at 15 K, 50 K, 150 K, 200 K and (d) 300 K

50 K, 160 K and 380 K (FM T_c), respectively (c.f. Fig. 5.7b and Fig. 5.9). Such ferromagnetic features of BFCT25 are confirmed by the magnetic hysteresis loops extracted from the linear M-H paramagnetic background at the temperature between 15 and 300 K, as shown in Fig. 5.7c and 5.7d. The increase in remanence and coercivity with decrease in temperature strengthens the evidences for BFCT25 being ferromagnetic (cf. also the ferromagnetic resonance (FMR) spectroscopy at room temperature in Fig. 5.10). Moreover, a rapid increase in magnetization at low magnetic field in Fig. 5.7d suggests a random distribution of ferromagnetically ordered Fe/Co rich areas at 300 K, which is consistent with the following observations of the piezoelectric force microscope (PFM) scans under applied magnetic field.

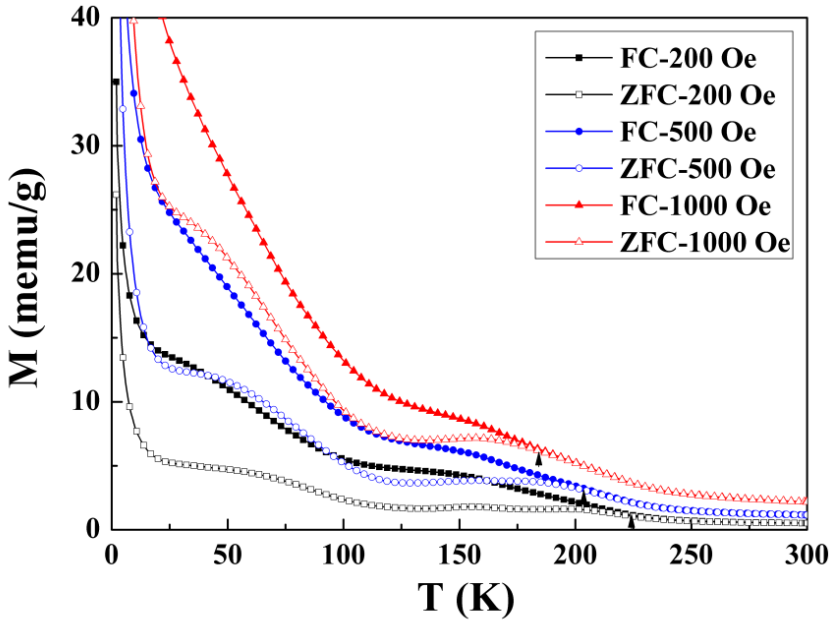

Fig. 5.8 ZFC-FC curves of BFCT25 measured under different magnetic fields

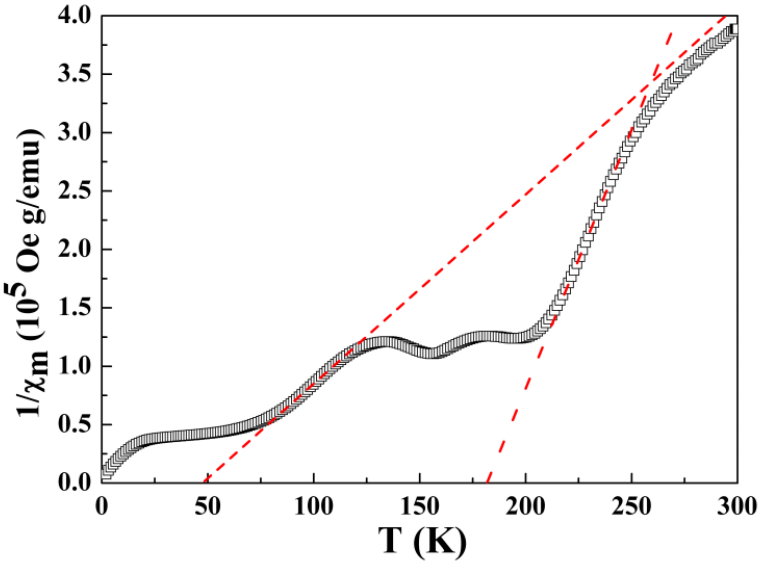

Fig. 5.9 Temperature dependence of reverse magnetic susceptibilities of BFCT25.

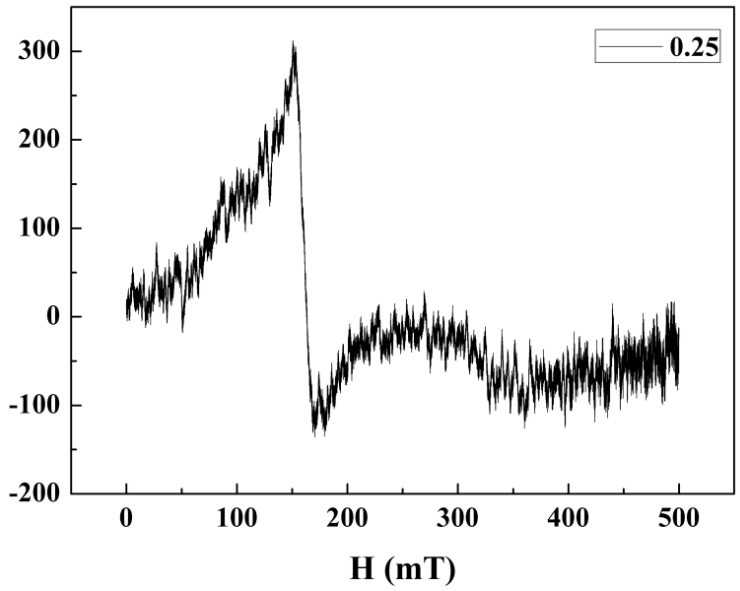

Fig. 5.10 Ferromagnetic resonance spectroscopy of BFCT25

First principle modeling of magnetization.

In order to understand the nature of ferromagnetic property of BFCT25, the density functional theory calculations were performed (see Methods). It is expected that there is

Fe^{3+}-O-Fe^{3+}, Fe^{3+}-O-Co^{3+} and Co^{3+}-O-Co^{3+} exchange interactions present in BFCT25. Whereas, since the ceramic contains equal proportion of Fe and Co ions, one would expect further a dominant Fe^{3+}-O-Co^{3+} interaction. Fig. 5.11 shows the exchange properties between the adjacent titled FeO_6 and CoO_6 octahedra with the Hubbard U corrections U_{Fe} = 2 eV and U_{Co} = 3 eV, respectively. It can be seen from Fig. 5.11a that the magnetism of the system is mainly originated from the substituted Co(Fe) atoms (2.604 μ_B for Fe and 1.868 μ_B for Co), and their surrounding O atoms also have small contribution (less than $0.1\mu_B$/atom). This coincides with the Fig. 5.11b that Fe and Co atom has strong minority peaks near the Fermi level and O atom only has weak peaks. With a closer look at Fig. 5.11b, it can be found that for the majority part two small peaks appear at the Fermi level, which means that the Fe d_{xy} orbital hybridize with the Co d_z^2 through the O p_y/p_z orbital, resulting in ferromagnetic coupling between Fe^{3+} and intermediate-spin state of Co^{3+}. This is insofar important, as the calculations show that the exchange interactions in Fe^{3+}-O-Fe^{3+} with U_{Fe} = 2 eV and Co^{3+}-O-Co^{3+} with U_{Co} = 3 eV are all of ferromagnetic as well. Consequently, in principle, we have thus ferromagnetically ordered Fe/Co rich areas with the nearest-neighbour ferromagnetic coupling in Fe^{3+}-O-Fe^{3+}, Fe^{3+}-O-Co^{3+} and Co^{3+}-O-Co^{3+} being respectively 16.38 meV, 29.09 meV and 59.89 meV (Table 5.1), which give rise to three ferromagnetic transitions of BFCT25, agreeing with the experimental observations qualitatively.

Given that the magnetic Fe/Co ions are responsible for the magnetism and parts of ferroelectricity of BFCT25, the higher local concentration of Fe/Co with ferromagnetic ordering is expected to be of multiferroic as well.

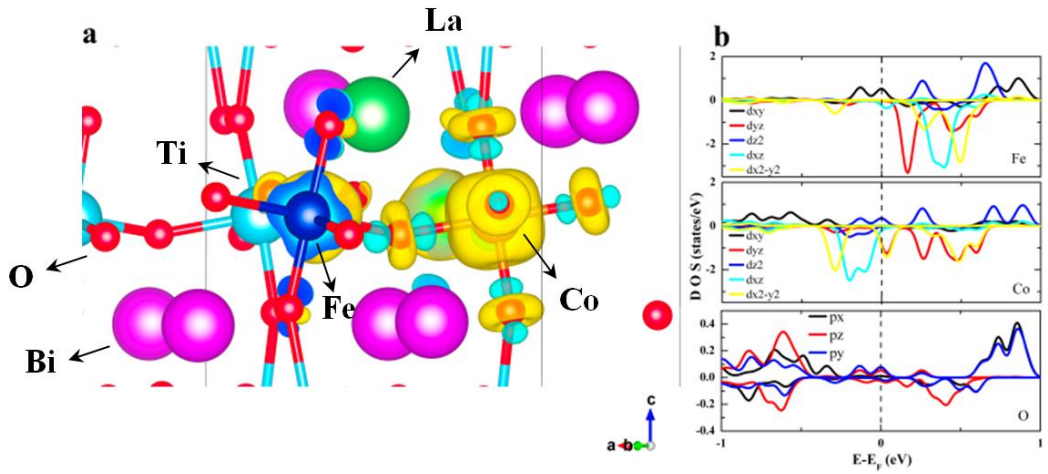

Fig. 5.11 (a) Spin density of BFCT25, red atom – O, pink atom – Bi, green atom – La, light blue atom – Ti, dark blue atom – Co, brown atom – Fe and (b) density of state of BFCT25.

Furthermore, as suggested by the rapidly changing of magnetization in Fig. 5.7d at the room temperature, these multiferroic areas should also distribute randomly in BFCT25 and exhibit a magnetic response by applying magnetic fields. In order to confirm the magnetoelectric coupling at room temperature, the ferroelectric domains was imaged using PFM under an in-plane magnetic field (Fig. 5.12). The sample in Fig.6 has the same microstructure and observed direction as in Fig. 5.3b SEM. After applying a positive magnetic field parallel to the sample surface (Fig. 5.12b and 5.12c) the direction of polarization in the marked areas turn to out of plane. Clearly, the sizes over hundreds of nanometers (nm) multiferroic areas are revealed. The symmetric changes of the FE polarization when inverting the magnetic field direction might be due to a stress-strain-mediated magnetoelectric coupling mechanism via magnetostriction and piezoelectricity. The ME coupling was measured at 100 K through the measurement of

magnetic field induced electric field (Fig. 5.13). The value of maximum ME efficient is 0.57 mV $cm^{-1}Oe^{-1}$.

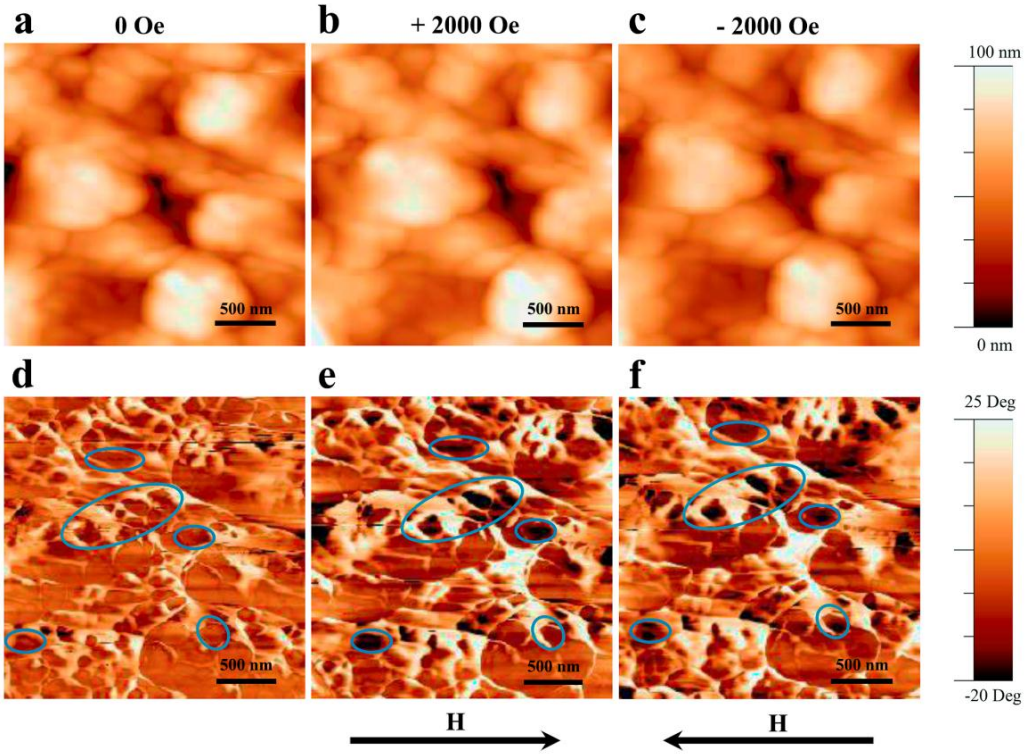

Fig. 5.12 Ferroelectric domain switches under magnetic field of BFCT25 (a) topography and (d) vertical PFM phase under 0 Oe H field; (b) topography and (e) vertical PFM phase under +2000 Oe H field; (c) topography and (f) vertical PFM phase under -2000 Oe H field. The applied in-plane magnetic field is marked by arrow. The regions of domain switching are marked by blue circles.

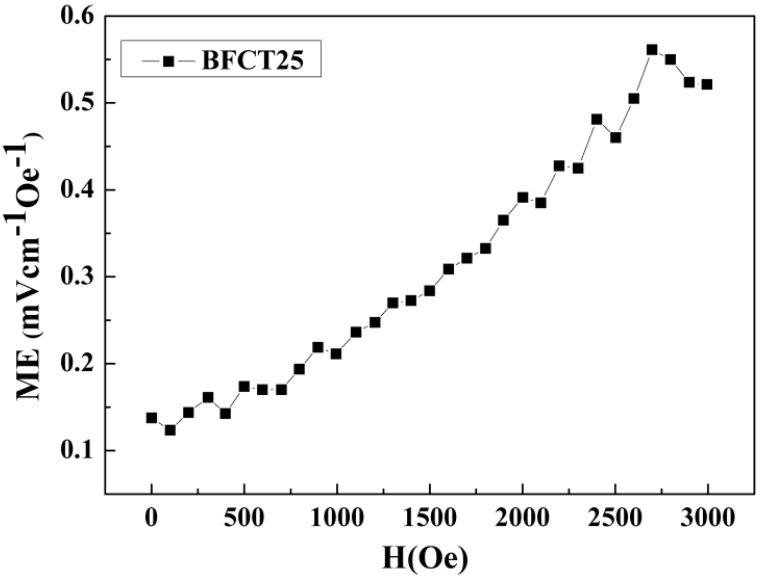

Fig. 5.13 ME coupling versus magnetic field of BFCT25 at 100 K.

5.4 Conclusions

No second phase was detected in XRD, neutron diffraction and SEM, which demonstrates that BFCT25 are single phase Aurivillius layer structured materials. Magnetic atoms Fe/Co were found to be contained in the grains by EDX. This is further proved by the shift of FE T_c with increasing the content of magnetic atoms. These observations confirmed the successful substitution of Ti with Fe/Co at B-site. Weak ferromagnetism which originates from the exchange interaction of Fe^{3+}-O-Co^{3+} was detected by FRM at room temperature. Moreover, the first principle modeling confirmed the magnetic coupling of the local Fe and Co cations through media of oxygen atom. The magnetism of BFCT can be therefore considered from the long-range magnetic ordering in the local Fe/Co rich regions. This is consistent with the magnetic order size from 100 to

200 nm in Fig. 5.12. The Co^{3+} changes from high spin to low spin state with decreasing temperature. Therefore, it is envisaged that other magnetic transitions should take place below 300 K. Two magnetic transitions were observed in M-H loops from 5 to 300 K. The in-situ PFM measurements showed clear changes in ferroelectric domain configurations during the application of the magnetic field, unambiguously proving multiferroic behavior at room temperature. The magnetism and parts of the ferroelectricity are related to the magnetic atoms in BFCT.

The present results clearly prove the existence of multiferroic activity at room temperature in BFCT Aurivillius ceramics; they are expected to pave the way for further composition refinements aimed at tailoring desired multiferroic properties.

Chapter VI Multiferroic behaviour of $Bi_{4.25}La_{0.75}Fe_{0.5}Co_{0.5}Ti_3O_{15}$

6.1 Introduction

Aurivillius compound $Bi_4Ti_3O_{12}$ (BTO) was previously researched as a candidate for non-volatile ferroelectric random access memory because of its good fatigue resistance and large spontaneous polarizations along a axis.[14,130] By inserting $BiMO_3$ (M=Fe, Co, Mn, etc.) into BTO, a typical $Bi_5MTi_3O_{15}$ Aurivillius phase with a four layered structure can be formed. The phase showed FE and weak FM at room temperature.[11,131]

In this work 4-layer Aurivillius phase material $Bi_{4.25}La_{0.75}Fe_{0.5}Co_{0.5}Ti_3O_{15}$ (BLFCT) were prepared, La substitution is thought to decrease the conductivity and ferroelectric coercive field, while as the Co and Fe co-substitution would increase the magnetization.[11,100] Although BLFCT was reported to exhibit obvious FM and FE at room temperature,[103] there are still debates on the origin of the magnetic properties in BLFCT because they may originate from the secondary phases, often not detected by laboratory XRD diffractometers.[107] In order to study the origin of the magnetic properties, highly grain-oriented BLFCT ceramics are proposed. As a consequence of the anisotropy of microstructure of Aurivillius phase material, textured BLFCT ceramic is supposed to show anisotropic FE and FM properties in a single phase. Spark plasma sintering(SPS) is an efficient sintering process to fabricate high-density and textured materials.[132] In this work, SPS has been employed to produce highly grain-oriented BLFCT ceramic in order

to study the possible anisotropy of ferroelectric and magnetic properties in Aurivillius phase materials.

6.2 Experiment

The BLFCT powders were obtained using a conventional solid state reaction route. First, $Bi_{3.25}La_{0.75}Ti_3O_{12}$ powders were synthesized using Bi_2O_3, La_2O_5 and TiO_2. They were calcined at 800 °C for 4 h. Then $Bi_{3.25}La_{0.75}Ti_3O_{12}$ powders were mixed together with Bi_2O_3, Fe_2O_3 and Co_3O_4 according to the stoichiometric formulae of BLFCT. The mixture was calcined at 950 °C for 4 h. The textured ceramics were obtained in a two-step process using SPS. The BLFCT powders were consolidated at 825 °C for 5 min under a uniaxial pressure of 80 MPa in a graphite die with an inner diameter of 20 mm. The dense samples were superplastically deformed at 950 °C for 5 min under a pressure of 50 MPa in a lager graphite die with an inner diameter of 30 mm. In order to remove carbon in SPSed ceramics, sintered samples were annealed at 800 °C for 10 h in air. The relative density of the textured sample was 95%. The bulk ceramics were cut perpendicular and parallel to the SPS pressure direction. The crystal structures of the obtained ceramics were determined with XRD using Cu Kα radiation at RT (X'Pert Pro, PANalytical, Almelo, The Netherlands). The surface morphology of the grain orientated ceramics was studied using a scanning electron microscopy (SEM) (FEI Inspect-F, Hillsboro, OR, USA). The ferroelectric $I-E$ (current–electric field) and $P-E$ (polarization–electric field) hysteresis loops were measured using a ferroelectric hysteresis measurement tester (NPL,

UK)[114]. The temperature dependence of the dielectric permittivity and loss was measured at different frequencies using an LCR meter (Agilent, 4284A) and a purpose-made furnace. The magnetization hysteresis loops and temperature dependence of magnetization were measured by superconducting quantum interference device magnetometer (Quantum Design, a model MPMS (SQUID) VSM) at temperature 1.8 K $\leq T \leq$ 500 K in magnetic field -1 T $\leq H \leq$ 1 T.

6.3 Results and discussions

Fig. 6.1(a) and Fig. 6.1(b) show X-ray diffraction patterns of BLFCT powders and textured ceramics. Both materials are single phase with an Aurivillius structure (XRD PDF 89-8545). Fig. 6.1(b) exhibits strong diffraction peaks in (*0k0*) crystallographic planes, which indicates that the sample is highly grain-oriented. To estimate the degree of orientation, the Lotgering factor[109] *f* was calculated using XRD data. For the textured BLFCT ceramics *f* = 0.64, which confirms a high degree of grain alignment in ceramic samples.

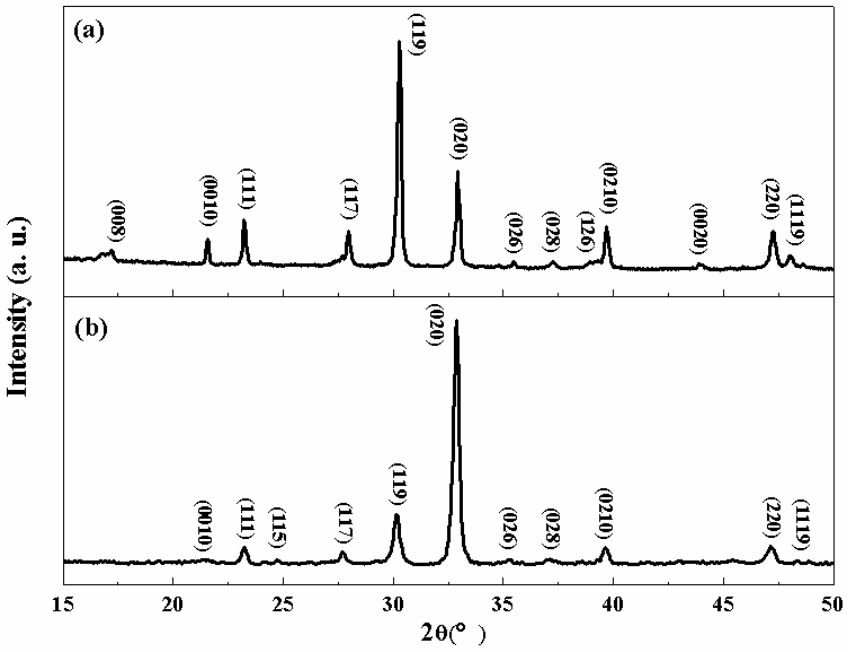

Fig. 6.1 X-ray diffraction patterns of BLFCT (a) powder and (b) textured ceramic.

BLFCT textured ceramic with high density (95%) was prepared by SPS. Fig. 6.2 shows the morphology of the BLFCT textured ceramic oriented parallel [//] and perpendicular [⊥] to SPS pressure direction. The grains are plate-like with their a-b axes orientation

perpendicular to the SPS pressure direction. A small amount of second phase about 1.7 Vol.% (calculated based on the area of secondary phase using the grid area calculation) (octahedral-like shape grains marked by the red circle in in Fig. 6.2) has been observed by SEM.

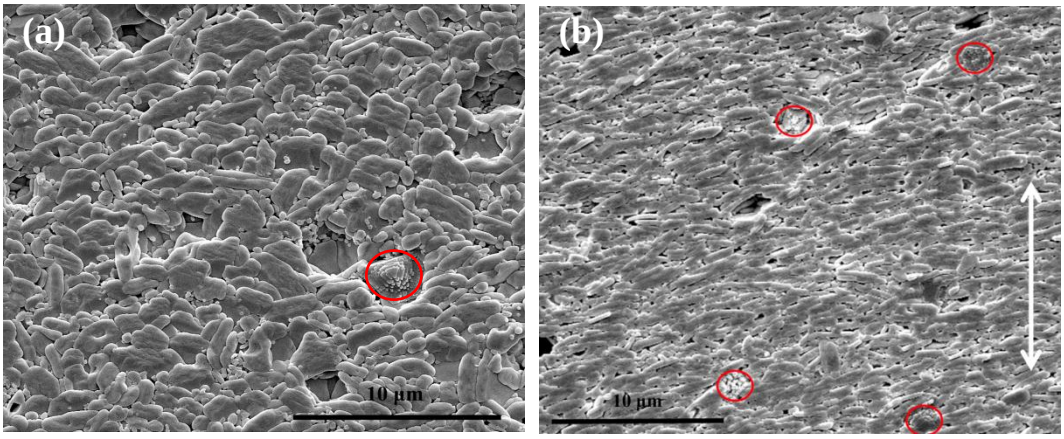

Fig. 6.2 SEM micrographs taken on the polished and thermally etched surfaces of grain-orientated BLFCT ceramics with normal of the plane: (a) parallel [//] and (b) perpendicular [⊥] to the SPS pressure directions. Pressure direction is marked by white arrow. Secondary phases are marked by red circles.

According to the EDS analysis (Fig. 6.3), the secondary phase consists of Fe, Co and O, in addition to Ti at a low concentration. To quantitatively determine the composition of the secondary phase, EDS data (spot scan) from different areas of the octahedral particles were collected and analysed. The results show that the atomic ratio Co/(Fe + Ti) is about 1. This suggests that the impurity particles are supposed to be Ti mixed Co2FeO4 or CoFe2O4 spinel ferrites. Similar observations on the presence of spinel-type impurities have been reported for Aurivillius phase multiferroics.[107,133,134]

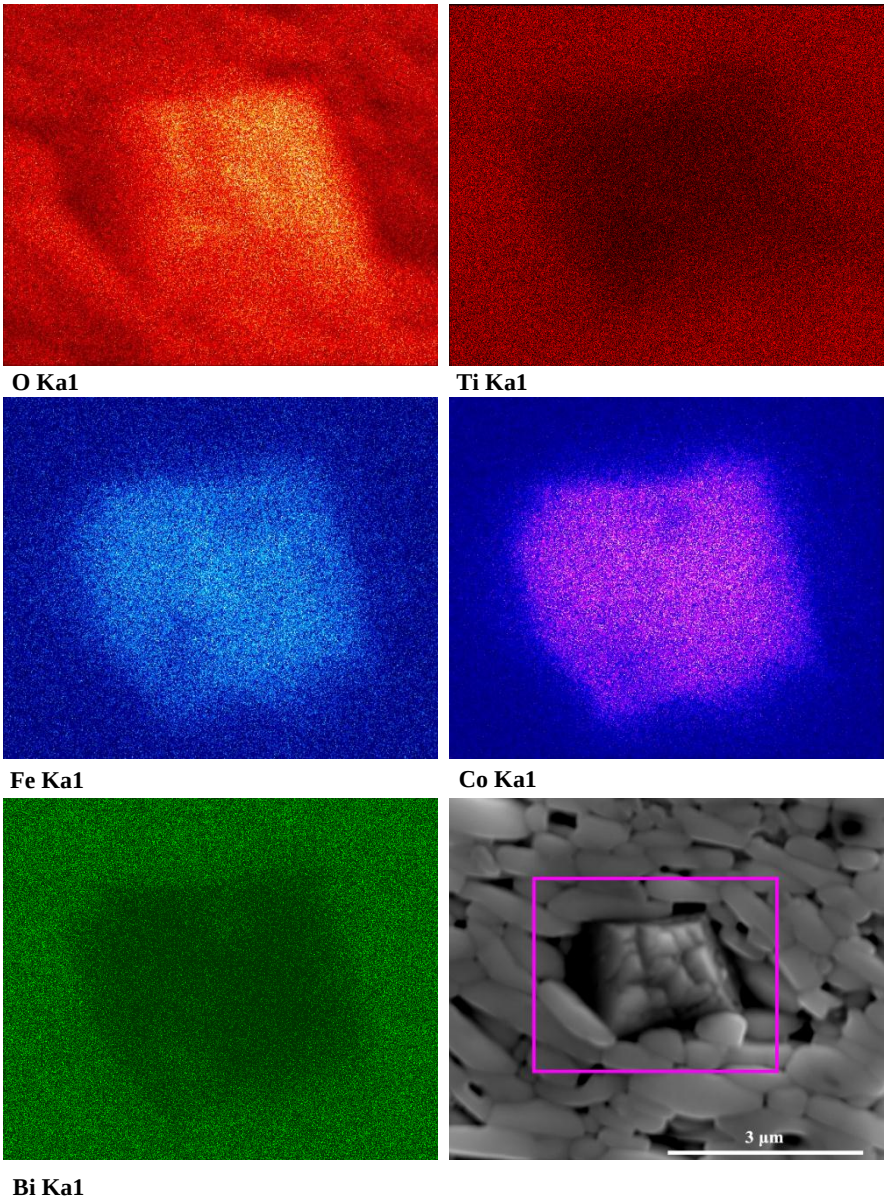

Fig. 6.3 EDX mapping of the secondary phase

Fig. 6.4 shows the temperature dependence of the dielectric properties of BLFCT measured perpendicular to the SPS pressure direction at different frequencies. The peak of the dielectric permittivity at about 1100 K corresponds to the FE T_c of $Bi_{4.25}La_{0.75}Fe_{0.5}Co_{0.5}\ Ti_3O_{15}$.

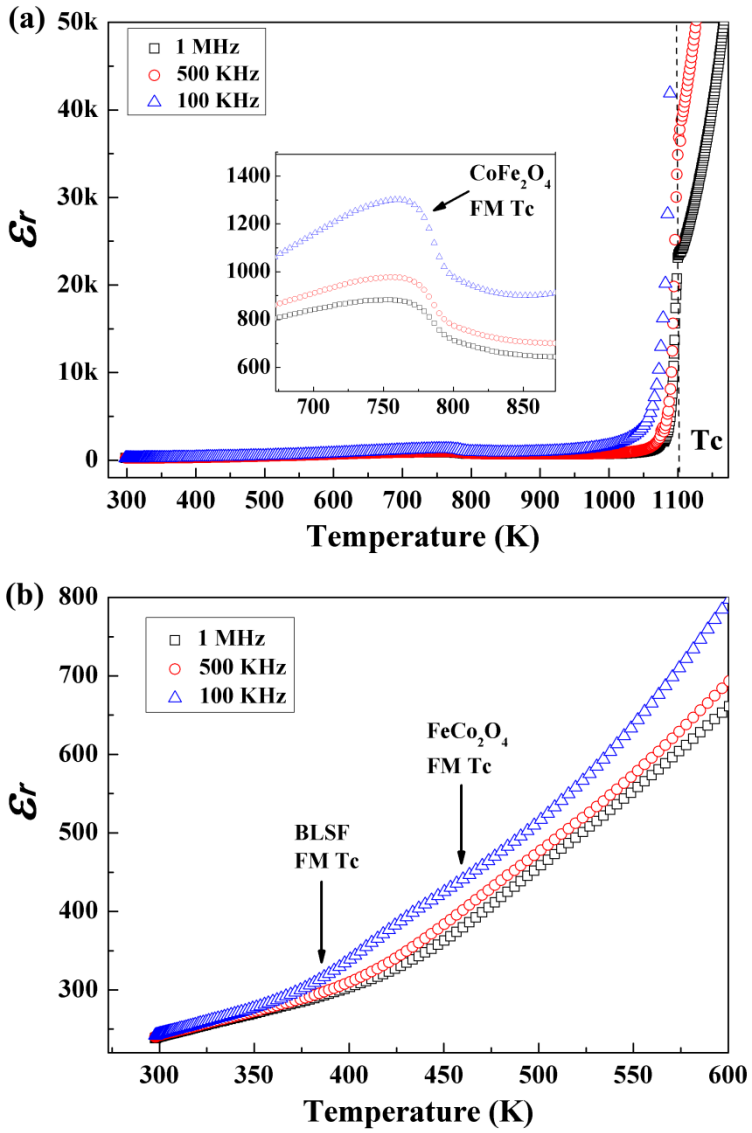

Fig. 6.4 Temperature dependence of the dielectric properties of BLFCT ceramics measured perpendicularly [⊥] to the SPS pressure direction (a) 300 - 1100 K, the inset shows the enlargement of the peak in 775 K, (b) 300 - 600 K.

It is higher than that of Aurivillius $Bi_5Ti_3FeO_{15}$ phase (at 1023 K).[131,135] The inset of Fig. 6.4(a) shows a frequency independent peak in permittivity at about 775 K, which could be likely related to the ferromagnetic transition of spinel oxide $CoFe_2O_4$ (T_c ~ 793K).[136,137] The two anomalies at about 460 K and 380 K in Fig. 6.4(b) can be possibly connected to

the ferromagnetic transition of spinel oxide Co_2FeO_4 (T_c ~ 460 K)[138] and BLFCT respectively.

Fig. 6.5(a) shows the zero field cooling (ZFC) and field cooling (FC) magnetization of BLFCT measured perpendicular [⊥] to the SPS pressure direction in temperature intervals of 5 - 300 K and 300 – 500 K at 200 Oe. The discontinuity of the FC data in the figure originates from that the measurements were done using two different furnaces (low and high temperature units). The BLFCT sample undergoes a ferromagnetic to paramagnetic transition at about 395 K (defined as the temperature of the peak of dM/dT) which is corresponds to the ferromagnetic transition of BLFCT as observed in Fig. 6.5 (b) The overlapping of ZFC/FC curves above 460 K indicates that the main ferromagnetic contribution is not from $CoFe_2O_4$. The split point (375 K) of ZFC and FC curves is slightly below the transition temperature of Co_2FeO_4 and BLFCT, which suggest that the ferromagnetic state originates predominantly from Co_2FeO_4 and/or BLFCT. The spontaneous magnetization of Co_2FeO_4 is about 16 – 23.5 emu/g.[139] Therefore the spontaneous magnetization of 1.7 Vol. % Co_2FeO_4 is about 0.27 – 0.4 emu/g which is much smaller than the saturated magnetization of BLFCT at high magnetic field (Ms = 0.8 emu/g) in the inset of Fig. 6.5 (b). This indicates that the dominating contribution to the ferromagnetic moment of BLFCT comes from the main Aurivillius phase. Moreover, the textured structure barely affects the magnetization of Co_2FeO_4 in different directions because it is a cubic phase material at room temperature and disorder distribution in

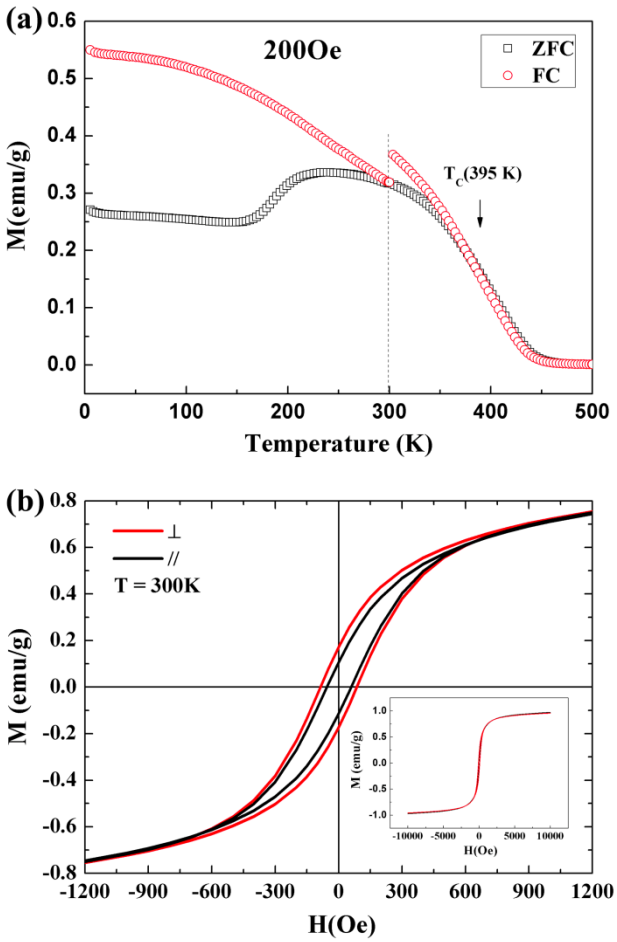

Fig. 6.5 (a) Temperature dependence of the magnetization for BLFCT ceramics [⊥] in the ZFC/FC modes measured in H = 200 Oe (measure in two different furnace units). (b) Field dependence of magnetization at 300K for the grain-orientated BLFCT samples in perpendicular [⊥] and parallel [//]. The inset shows saturated MH loops at high magnetic field.

ceramics.[140] In Fig. 6.5 (b), the measured FM coercivities are approximately $H_c[\,//\,] = 55$ Oe and $H_c[\,\perp\,] = 85$ Oe. The FM remnant magnetization $M_r[\,//\,] = 0.1$ emu/g and $M_r[\,\perp\,] = 0.17$ emu/g. The larger value of $M_r[\,\perp\,]$ than that of $M_r[\,//\,]$, is most likely due to the magnetic anisotropy of the Aurivillius phase structure of $Bi_{4.25}La_{0.75}Ti_3Fe_{0.5}Co_{0.5}O_{15}$, which can be explained by the ferromagnetic order, induced by the superexchange of

Fe^{3+}-O-Co^{3+}. Based on first principle calculations in Aurivillius phase materials,[141] magnetic ions prefer to occupy B-site in the two middle layers of the perovskite slab, which induces a magnetic order in the a-b plane. Due to AFM/FM interactions between two adjacent Fe/Co-O octahedra, the Bi_2O_2 layer will supress any coupling between two pseudo-perovskite blocks layers along c-axis,[141] resulting in the observed anisotropy of magnetization in Aurivillius phase $Bi_{4.25}La_{0.75}Fe_{0.5}Co_{0.5}$ Ti_3O_{15}.

Fig. 6.6 shows the *I-E* and *P-E* hysteresis loops of the grain-orientated BLFCT ceramics perpendicular to SPS pressure direction at room temperature. Although the ferroelectric hysteresis loops could not be saturated due to the dielectric breakdown under high electric field, the current peaks in *I-E* loops indicates the ferroelectric domain switching[128] in the *a-b* plane of the Aurivillius phase $Bi_{4.25}La_{0.75}Fe_{0.5}Co_{0.5}Ti_3O_{15}$. To investigate a magnetoelectric coupling in the textured BLFCT ceramics, PFM of the samples under an external magnetic field was performed (Fig. 6.7). The vertical PFM scanning was performed on etched surface of [⊥] plane with roughness of about 260 nm. Some FE domains (yellow circles in Fig. 6.7) emerged under a positive magnetic field (+2000 Oe) applied in parallel direction to sample surface. Under the negative magnetic field of -2000 Oe, the areas of these domains decreased.

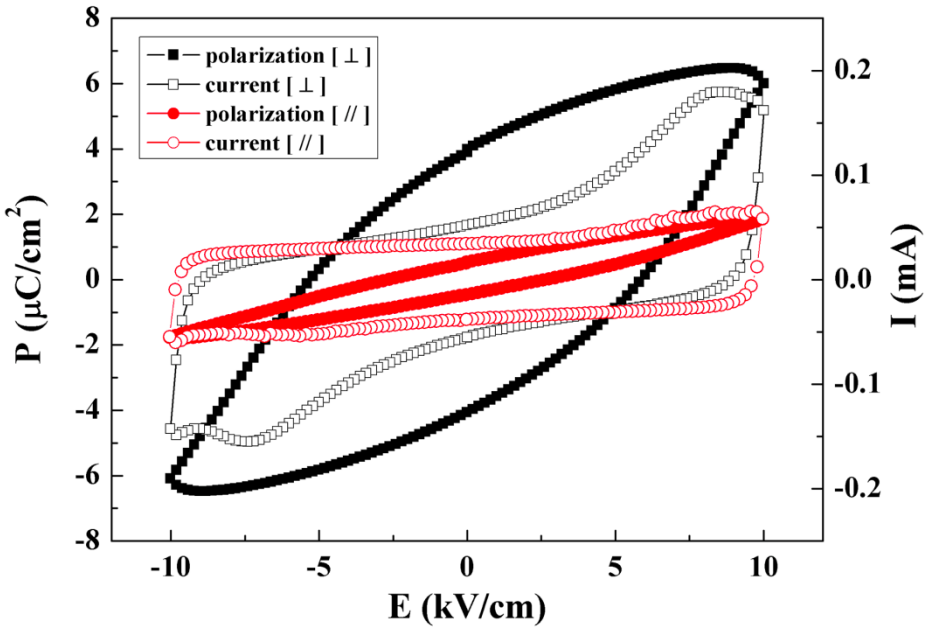

Fig. 6.6 P-E and I-E hysteresis loops of the textured BLFCT ceramics measured in the perpendicular and parallel direction to the SPS pressure direction.

The secondary phases Co_2FeO_4/$CoFe_2O_4$ are nonpolar ferromagnets showing no piezoelectric response. Therefore, the FE domain switching observed upon magnetic field reversal is believed to occur indeed in the main Aurivillius phase. Additionally, it should be noted that the density of secondary phase impurities is low and they appear on scale larger than 10 μm (Fig. 6.2). These factors rules out a magnetostriction effect and magnetic dipole-dipole interaction of the secondary phase on the observed magnetoelectric coupling. Thus, the presence of magnetic impurities has no influence on the main results and conclusions of this work. The areas where the ferroelectric domain switching takes part are proposed to be the grains with highest concentrations of Fe/Co due to the random distribution of

Fe/Co at B-site in Aurivillius phase.[12] Such a magnetoelectric coupling confirms the intrinsic multiferroelectic character of the Aurivillius phase BLFCT.

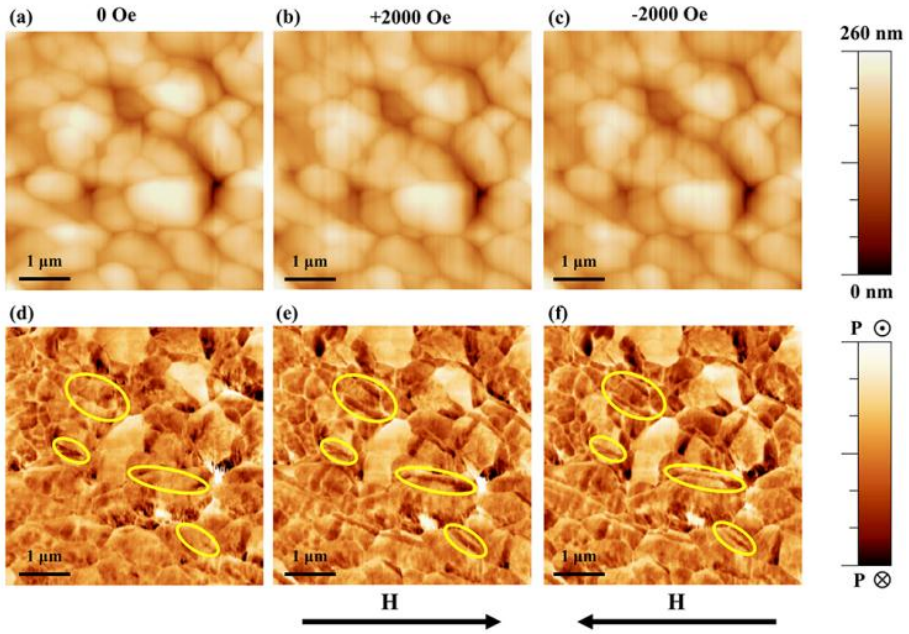

Fig. 6.7 Ferroelectric domain switches under magnetic field of BFCT (a) topography and (d) vertical PFM phase under 0 Oe *H* field; (b) topography and (e) vertical PFM phase under +2000 Oe *H* field; (c) topography and (f) vertical PFM phase under -2000 Oe *H* field. The applied in-plane magnetic field is marked by arrow. The regions of domain switching are marked by yellow circles.

6.4 Conclusions

In conclusion, the Aurivillius phase $Bi_{4.25}La_{0.75}Fe_{0.5}Co_{0.5}Ti_3O_{15}$ is ferroelectric and ferromagnetic active at room temperature. Ferromagnetism is suggested to originate predominantly from the exchange interactions between neighbouring Fe^{3+}-O-Co^{3+} ions. The textured Aurivillius phase ceramic was demonstrated to be an intrinsic room-temperature multiferroic material, where the B-site Co/Fe cations contribute simultaneously to the ferroelectric polarization and ferromagnetic moment.

Chapter VII Multiferroic behaviour of $Bi_{5.25}La_{0.75}FeCoTi_3O_{18}$

7.1 Introduction

The Aurivillius phase materials $Bi_5FeTi_3O_{15}$ (m=4) and $Bi_6Fe_2Ti_3O_{18}$ (m=5) which can be considered as inserting one and two mole of $BiFeO_3$ into $Bi_4Ti_3O_{12}$ showed coexistence of FE and FM.[135,141] The Aurivillius ferroelectric $Bi_4Ti_3O_{12}$ (m=3) was previously researched as candidates for non-volatile ferroelectric random access memory (FRAM) because of its good fatigue resistance and large FE spontaneous polarizations along the a-axis.[21] By substituting Co of Fe at B-site, the ferromagnetism of $Bi_5Fe_{0.5}Co_{0.5}Ti_3O_{15}$ (m=4) and $Bi_6FeCoTi_3O_{18}$ (m=5) were remarkably improved and showed multiferroic property at room temperature.[11,106] However, the origin of its magnetic properties is still under debate because the net magnetization may originate from the presence of secondary phases which are not easily detected by laboratory XRD diffractmeters.[107] Therefore, more researches are needed to focus on the origin of multiferroic property of Aurivillius. In this study, textured Aurivillius phase $Bi_{5.25}La_{0.75}FeCoTi_3O_{18}$ (BLFCT) ceramics was prepared by Spark plasma sintering (SPS). La substitution is thought to reduce the electrical conductivity and decrease the ferroelectric coercive field. Due to the structural anisotropy of Aurivillius phase materials and ferroelectric polarization in a-b plane, textured BLFCT ceramic is expected to show higher spontaneous polarization compare to conventional sintering. The neutron diffraction and Piezoresponse Force Microscopy (PFM) measurement were performed under various magnetic fields to investigate the

multiferroic property in the main phase.

7.2 Experiment

The BLFCT powders were obtained using a conventional solid state reaction route. The raw powders were mixed using Bi_2O_3, La_2O_3, TiO_2, Fe_2O_3 and Co_3O_4 according to the stoichiometric formulae. The mixture was calcined at 850 °C for 20 h. The textured ceramics were obtained in a two-step process using a SPS furnace. The BLFCT powders were consolidated at 825 °C for 5 min under a uniaxial pressure of 80 MPa in a graphite die with an inner diameter of 20 mm. The dense samples were superplastically deformed at 950 °C for 5 min under a pressure of 50 MPa in a lager graphite die with an inner diameter of 30 mm. In order to remove carbon from the SPS processed ceramics, sintered samples were annealed at 800 °C for 10 h in air. The relative density of the ceramic samples, as measured by Archimedes` method, was about 97%. The bulk ceramics were cut parallel to the SPS pressure direction. The crystal structures of the obtained ceramics were determined by the X-ray diffraction using Cu Kα radiation at RT (X'Pert Pro, PANalytical, Almelo, The Netherlands). The surface morphology of the grain orientated ceramics was observed using a scanning electron microscopy (SEM) (FEI Inspect-F, Hillsboro, OR, USA). The ferroelectric $I-E$ (current–electric field) and $P-E$ (polarization–electric field) hysteresis loops were measured using a ferroelectric hysteresis measurement tester (NPL, UK). The

temperature dependence of the dielectric permittivity and loss was measured at different frequencies using an LCR meter (Agijent, a model 4284A) and a purpose-made furnace. The magnetization hysteresis loops and temperature dependence of magnetization were measured by vibrating sample magnetometer (VSM) over the temperature interval 300 - 800 K. The ferroelectric domain morphology was obtained by PFM (NT-MDT Ntegra systems) at 70 kHz with a 10 V AC electric field under a DC magnetic field +/- 2000 Oe.

7.3 Results and discussions

Figure 7.1a shows the X-ray diffraction (XRD) pattern of the BLFCT powder. In XRD pattern, all the peaks were indexed by an orthorhombic lattice and space group B2cb, which is consist to the reported five-layered Aurivillius phase.[142,143] No detectable secondary phases were found here. Fig. 7.1b shows the SEM morphology of the textured

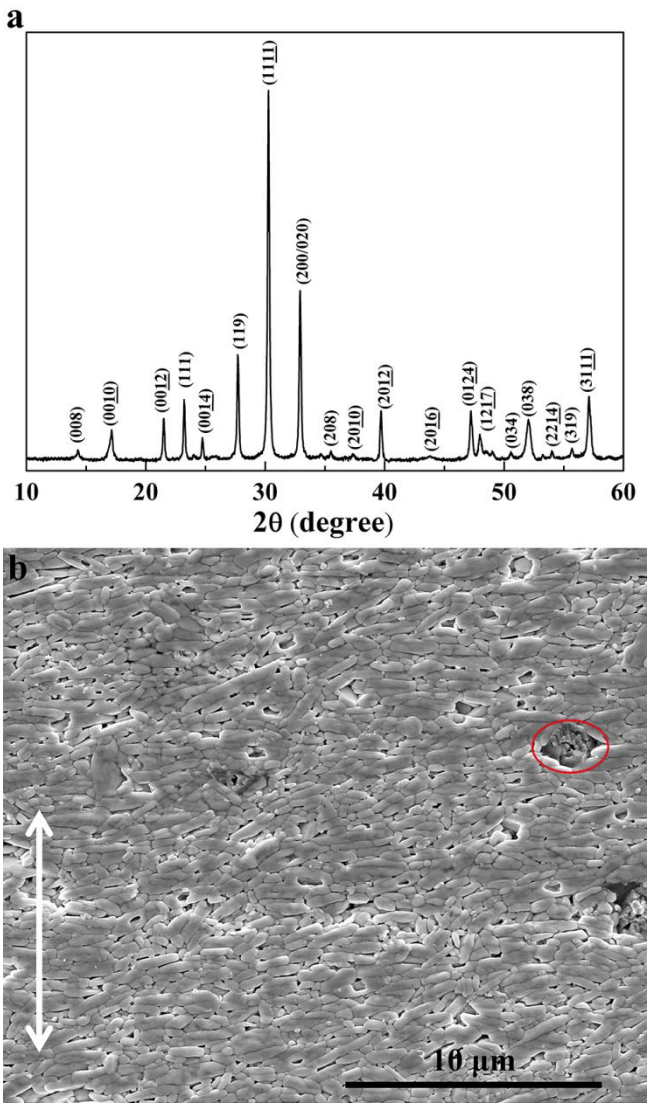

Fig. 7.1 X-ray diffraction patterns of (a) the BLFCT powder (b) textured ceramic sample prepared by SPS. Pressure direction is marked as an arrow. Secondary phase is marked by red circle.

BLFCT ceramic sample. The plate-like grains aligned in the direction with their a-b axes perpendicular to the SPS pressure direction. A small amount of secondary phase marked by the red circle in Fig. 7.1b was observed. The amount of secondary phase is approximately 1.4 vol. % (estimated from SEM micrographs) which is below the trace level of XRD. According to the EDX line scanning results secondary phase (Fig. 7.2), the secondary phase mainly consists of Fe, Co, O and Ti. The details of the element percentage is showed in table 7.1 based on the average of the EDX spot scans. Thus the secondary phase is supposed to be Co_2FeO_4 spinel ferrite with partial titanium substitution of iron ($Co_2Fe_{1-x}Ti_xO_4$) which is reported in the four-layered Aurivillius compound $Bi_5Fe_{0.5}Co_{0.5}Ti_3O_{15}$.[107]

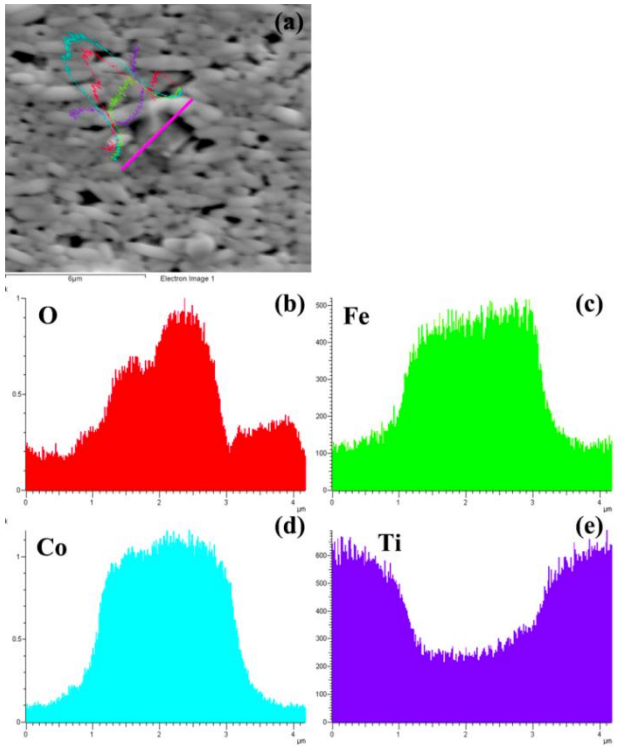

Fig. 7.2 EDX elemental line scanning across the secondary phase. (a) SEM images of the secondary phase, (b-e) the elements in the secondary phase.

Table 7.1 EDX data from secondary phase area

Elements	O	Co	Fe	Ti
At. %	68.95	17.43	9.83	3.8

Figure 7.3a shows the temperature dependence of dielectric constant and loss of BLFCT measured perpendicular to the SPS pressure direction at different frequencies. The peak of the dielectric permittivity at about 1060 K corresponds to the FE T_c of BLFCT. It is higher than that of $Bi_5Ti_3Fe_2O_{18}$ phase (at 973 K).[135] Fig. 7.3b shows the P-E and I-E hysteresis loops of the textured BLFCT ceramics measured in perpendicular direction to the SPS pressure direction at RT. The current peaks in I-E loops confirm the ferroelectric domain switching. The maximum value of the polarization of BLFCT is 10μC/cm^2.

Fig. 7.4a shows the temperature dependence of zero-field-cooled (ZFC) and the field-cooled (FC) magnetization under an applied magnetic field of 200 Oe for BLFCT. It is reported that the magnetic Curie temperature (T_{mc}) of $Bi_6Fe_{2-x}Co_xTi_3O_{18}$ decrease with the increase of cobalt percentage.[144] The BLFCT undergoes a paramagnetic to ferromagnetic transition at T_{c1}~494 K (defined as the temperature corresponding to the peak of dM/dT) which is higher than that of $Bi_6FeCoTi_3O_{18}$ (466 K). The ferromagnetism of BLFCT is induced by the superexchange interactions between neighboring Fe^{3+}-O-Fe^{3+}, Co^{3+}-O-Co^{3+} and Fe^{3+}-O-Co^{3+}. This consists with the EDX result of the main phase. Another transition was found at T_{c2}~353 K which should be the T_{mc} of the secondary phase $Co_2Fe_{1-x}Ti_xO_4$.

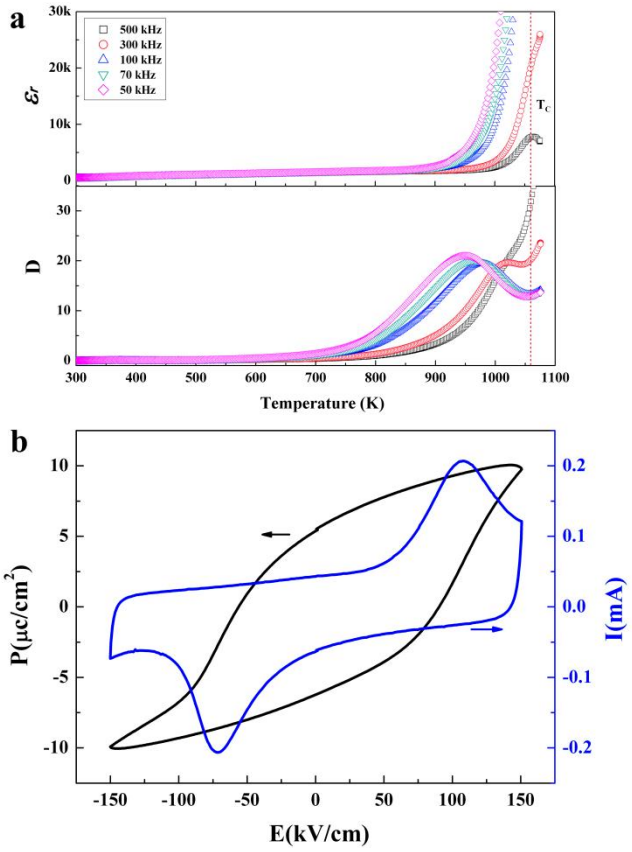

Fig. 7.3 (a) Temperature dependence of the dielectric properties of BLFCT ceramics measured perpendicularly [⊥] to the SPS pressure direction, (b) P-E and I-E hysteresis loops of the textured BLFCT ceramics measured in the perpendicular to the SPS pressure direction.

The T_{c2} is lower than T_{mc} of Co_2FeO_4 is 460 K which could be caused by the partial substitution of Fe by Ti.[107,139]

The spontaneous magnetization of Co_2FeO_4 is about 16 - 23.5 emu/g.[139] Therefore spontaneous magnetization of 1.4 vol.% $Co_2Fe_{1-x}Ti_xO_4$ is about 0.22 - 0.32 emu/g which is much smaller than the saturated magnetization of BLFCT at high magnetic field (M_s = 2 emu/g) in Fig. 7.4b. This indicates that the main ferromagnetism of BLFCT is from the main phase.

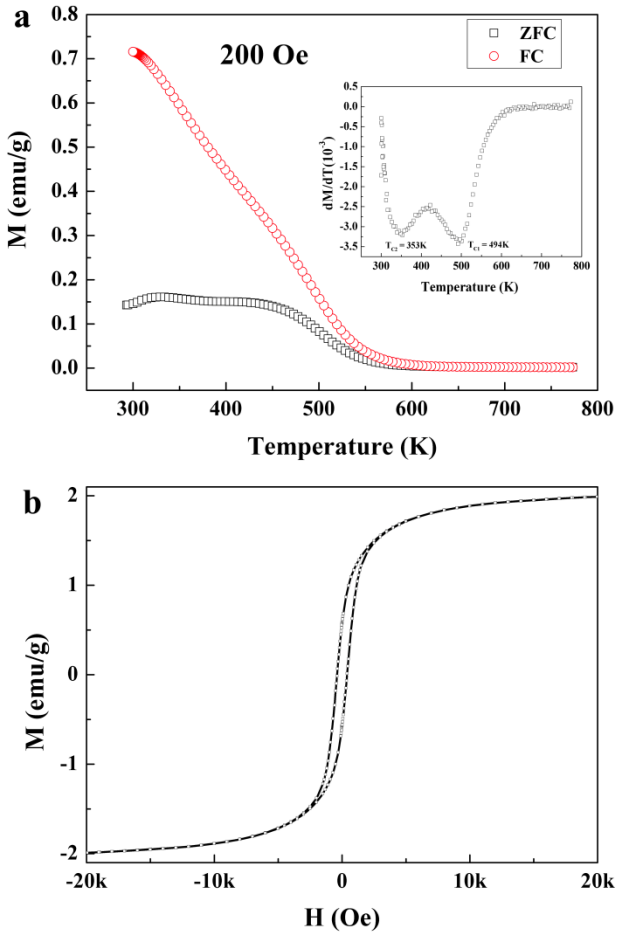

Fig. 7.4 (a) Temperature dependence of the magnetization for BLFCT ceramics [⊥] in the ZFC/FC modes measured in H = 200 Oe. The inset shows saturated temperature dependence dM/dT curves, (b) Field dependence of magnetization at 300K for BLFCT samples.

Fig. 7.5 shows the neutron diffraction of BLFCT ceramic under different magnetic field. It is found that the intensity of one peak changed with magnetic field. The peak is identified as $(01\overline{2}0)$ which is not belonging to the secondary phase. The intensity of peak $(01\overline{2}0)$ increases under an external 2T magnetic field. The intensity of the peak keeps the same when the magnetic field increased to 5T, which indicates the material is already saturated at 2T magnetic field.

Fig. 7.6 shows the magnetoelectric coupling using PFM under varies magnetic field. Vertical PFM was performed on BLFCT sample as shown in Fig. 7.6d. Partial ferroelectric domain switching (marked by the red circles) was observed by applying an in-plane magnetic field of +2000 Oe (Fig.7.6e), which is due to the local rich regions of Fe and Co.

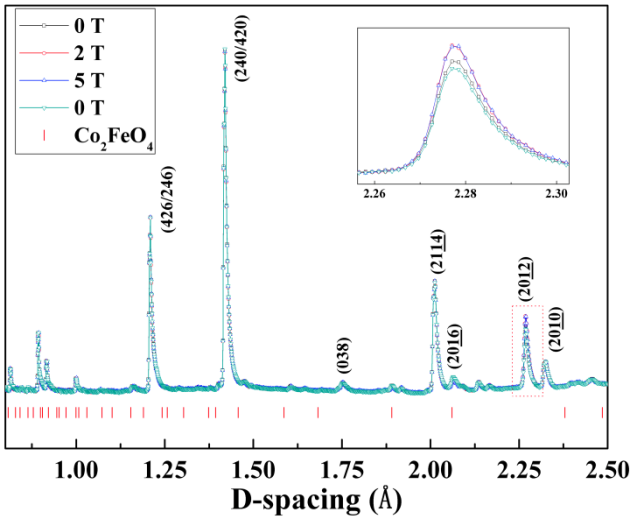

Fig. 7.5 Neutron diffraction of BLFCT ceramic at 300K under various magnetic fields.

When a magnetic field of -2000 Oe was applied in the opposite direction, parts of the ferroelectric domains switched back (Fig. 7.6f). The non-ferroelectric character and low volume percentage of the secondary $Co_2Fe_{1-x}Ti_xO_4$ can rarely induce all of these magnetoelectric responses. Therefore, these ferroelectric domains changes indicate the intrinsic multiferroelectric property of the main phase.

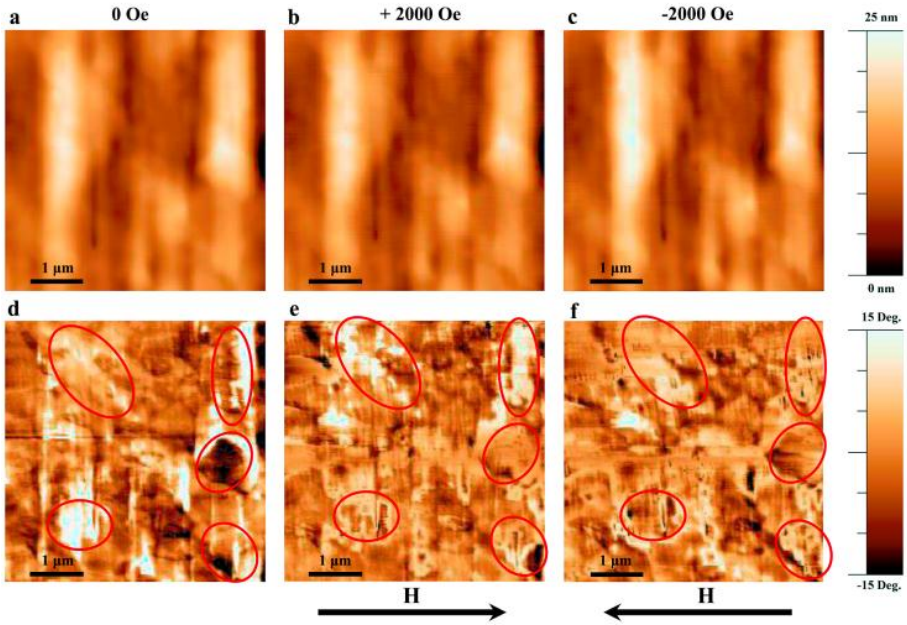

Fig. 7.6 Ferroelectric domain switches under magnetic field of BLFCT (a) topography and (d) vertical PFM phase under 0 Oe *H* field; (b) topography and (e) vertical PFM phase under +2000 Oe *H* field; (c) topography and (f) vertical PFM phase under -2000 Oe *H* field. The applied in-plane magnetic field is marked by arrow. The regions of domain switching are marked by red circles.

7.4 Conclusions

The Aurivillius phase $Bi_6La_{0.75}FeCoTi_3O_{18}$ is ferroelectric and ferromagnetic active at room temperature. Ferromagnetism is suggested to mainly originated from the superexchange interactions between neighboring Fe^{3+}-O-Fe^{3+}, Co^{3+}-O-Co^{3+} and Fe^{3+}-O-Co^{3+} in the main phase. Magnetic controlled ferroelectric domain switching has been observed at room temperature. The Aurivillius phase ceramics, with Co/Fe contributing to magnetization and polarization at the same time, can be considered an intrinsic multiferroic at room temperature.

Chapter VIII Conclusions and future work

8.1 Conclusions

In this project, high dense and textured ceramics of Aurivillius materials (m = 2, 3, 4 and 5) were fabricated by a two-step spark plasma sintering (SPS) method. The multiferroic properties of Aurivillius materials with different octahedral layers (m=2, 3, 4 and 5) were investigated (Table. 8.1). The substitution of Ti by Fe/Co atoms did not destroy the ferroelectricity of Aurivillius materials. All the Aurivillius materials showed ferroelectric activity at room temperature. The substitution of Ti by Fe/Co atoms induced the ferromagnetism of the all Aurivillius materials except the material with m =2 in this project. Clear ME couplings were observed in Aurivillius phase materials (m = 3, 4 and 5) where the magnetic atoms Fe/Co contributed to ferroelectric polarization and magnetic moment at the same time. This discovery could guide the design of room temperature single phase MFs with strong ME coupling for sensors and memories applications.

$Bi_3Nb_{1.125}Fe_{0.125}Co_{0.125}Ti_{0.75}O_9$ (m = 2)

Single phase and textured $Bi_3Nb_{1.125}Fe_{0.125}Co_{0.125}Ti_{0.75}O_9$ ceramics were prepared. It showed ferroelectricity at room temperature and the ferroelectric Curie point was 1155 K (Fig. 4.3). Paramagnetic behaviour was observed in domination due to the low amount of magnetic atoms (Fig. 4.5).

$Bi_{3.25}La_{0.75}Nb_{0.25}Fe_{0.125}Co_{0.125}Ti_{2.5}O_{12}$ (m = 3)

Single phase and textured $Bi_{3.25}La_{0.75}Nb_{0.25}Fe_{0.125}Co_{0.125}Ti_{2.5}O_{12}$ ceramic were prepared. It simultaneously showed ferroelectric and ferromagnetic properties at room temperature. The ferroelectric Curie point was about 556 K (Fig. 4.5). Three magnetic transitions were found at 50 K, 160 K and 380 K, respectively (Fig. 4.5). These three magnetic transitions were proposed to be caused by the ferromagnetic coupling of Fe^{3+}-O-Fe^{3+}, Fe^{3+}-O-Co^{3+} and Co^{3+}-O-Co^{3+} based on the first principle calculation (Table 5.1). The magnetoelectric coupling was confirmed by the magnetic field controlled ferroelectric domain switching at room temperature using PFM (Fig. 5.12).

$Bi_{4.25}La_{0.75}Fe_{0.5}Co_{0.5}Ti_3O_{15}$ (m = 4)

High dense and textured ceramics $Bi_{4.25}La_{0.75}Fe_{0.5}Co_{0.5}Ti_3O_{15}$ were prepared. The $Bi_{4.25}La_{0.75}Fe_{0.5}Co_{0.5}Ti_3O_{15}$ ceramics showed ferroelectric and ferromagnetic activities at room temperature. The ferroelectric and ferromagnetic Curie point was about 1100 K and 395 K, respectively (Fig. 4.5). A small amount of magnetic secondary phase which was below the resolution of XRD was observed by SEM. Furthermore, the magnetic contribution of the main phase was supported by the anisotropic M-H curves (Fig. 6.5) and magnetic field controlled ferroelectric domain switching at room temperature (Fig. 6.6).

$Bi_{5.25}La_{0.75}FeCoTi_3O_{18}$ (m = 5)

High dense and textured $Bi_{5.25}La_{0.75}FeCoTi_3O_{18}$ ceramics were prepared. The

$Bi_{5.25}La_{0.75}FeCoTi_3O_{18}$ ceramics showed ferroelectricity at room temperature with a ferroelectric Curie temperature about 1060 K (Fig. 4.5). Two magnetic transitions were found at 353 K and 494 K which are ferromagnetic Curie temperature of the secondary phase and the main phase, respectively. The magnetic contribution of the main phase was confirmed by the peak $(01\overline{2}0)$ intensity changes of neutron diffraction of $Bi_{5.25}La_{0.75}FeCoTi_3O_{18}$ (Fig. 7.5) and magnetic field controlled ferroelectric domain switching at room temperature (Fig. 7.6).

Table 8.1Multiferroic character of four Aurivillius compounds

Materials	Multiferroic properties
$Bi_3Nb_{1.125}Fe_{0.125}Co_{0.125}Ti_{0.75}O_9$	Paramagnetic and ferroelectric
$Bi_{3.25}La_{0.75}Nb_{0.25}Fe_{0.125}Co_{0.125}Ti_{2.5}O_{12}$	1.Single phase material 2.Ferromagnetic and ferroelectric order at room temperature 3. Magnetic field controlled ferroelectric domain switching at room temperature. 4. Magnetic field induced electric voltage changes at 100 K
$Bi_{4.25}La_{0.75}Fe_{0.5}Co_{0.5}Ti_3O_{15}$	1.Ferromagnetic and ferroelectric order at room temperature 2. Magnetic field controlled ferroelectric domain

	switching at room temperature. 3. Anisotropic ferroelectric and ferromagnetic properties originate from the main phase.
$Bi_{5.25}La_{0.75}FeCoTi_3O_{18}$	1.Ferromagnetic and ferroelectric order at room temperature 2. Magnetic field controlled ferroelectric domain switching at room temperature.

8.2 Future work

8.2.1 Optimization of powder preparation

In this project, we proved the magnetic contribution of the main Aurivillius phase. However, the magnetic secondary phase still obviously affects the magnetic properties of the Aurivillius phase ceramics (m = 4 and 5). Therefore, the solid state method should be improved by extending the calcination time of the powder preparing (>20h) and increasing reaction cycle number of times (2 or 3 times).

8.2.2 PFM on single crystal (single grain)

The PFM is sensitive to the sample surface and the applied electric field. The bulk samples are difficult to fulfil the requirement of PFM. Large and smooth grains can be

prepared by melt salt method. The large disk-like grain can be selected as single crystal used for PFM measurement. High electric field can be applied to the samples to achieve high quality of domain signal. Therefore, melt salt reaction would be used to prepare large grains of BLSF materials with m = 3, 4 and 5.

8.2.3 Investigation of Aurivillius phase material with different octahedral layers (m = 6)

$Bi_{5.25}La_{0.75}Fe_xCo_{3-x}Ti_3O_{18}$ ($1<x<3$) are selected as the next candidate. The soluble doping amount of magnetic atoms in the lattice increases with more octahedral layers in Aurivillius. Therefore, the increasing amount of magnetic coupling of Fe^{3+}-O-Fe^{3+}, Fe^{3+}-O-Co^{3+} and Co^{3+}-O-Co^{3+} will lead to the improvement of magnetization.

List of Publications

1. **Zheng Li**, Jing Ma, Zhipeng Gao, Giuseppe Viola, Vladimir Koval, Amit Mahajan, Xuan Li, Chenglong Jia, Cewen Nan and Haixue Yan. Room temperature magnetoelectric coupling in intrinsic multiferroic Aurivillius phase textured ceramics, Dalton Transactions, 2016, 10.1039/C6DT02703B.

2. Yanhui Sun, **Zheng Li***, Hangfeng Zhang, Chuying Yu, Giuseppe Viola, Shuai Fu, Vladimir Koval, Haixue Yan, Lead free, Bi3TaTiO9 ferroelectric ceramics with high Curie point, Materials Letters, 2016, 175:79–81. (* corresponding author)

3. Jian Liu, **Zheng Li**, Haixue Yan, Kyle Jiang, Spark Plasma Sintering of Alumina Composites with Graphene Platelets and Silicon Carbide Nanoparticles, Advanced Engineering Materials 2014, 16, No. 9.

References

1 Anderson, J. Ferroelectric storage elements for digital computers and switching systems. *Electrical Engineering* **71**, 916-922 (1952).

2 Scott, J. The physics of ferroelectric ceramic thin films for memory applications. *Ferroelectrics Review* **1**, 1-129 (1998).

3 Gajek, M., Bibes, M., Fusil, S., Bouzehouane, K., Fontcuberta, J., Barthelemy, A. & Fert, A. Tunnel junctions with multiferroic barriers. *Nature Materials* **6**, 296-302 (2007).

4 Scott, J. Data storage: Multiferroic memories. *Nature Materials* **6**, 256-257 (2007).

5 Hill, N. A. Why are there so few magnetic ferroelectrics? *The Journal of Physical Chemistry B* **104**, 6694-6709 (2000).

6 Eerenstein, W., Mathur, N. D. & Scott, J. F. Multiferroic and magnetoelectric materials. *Nature* **442**, 759-765, doi:10.1038/nature05023 (2006).

7 Wang, J., Neaton, J., Zheng, H., Nagarajan, V., Ogale, S., Liu, B., Viehland, D., Vaithyanathan, V., Schlom, D. & Waghmare, U. Epitaxial BiFeO3 multiferroic thin film heterostructures. *Science* **299**, 1719-1722 (2003).

8 Kubel, F. & Schmid, H. X-ray room temperature structure from single crystal data, powder diffraction measurements and optical studies of the Aurivillius phase $Bi_5(Ti_3Fe)O_{15}$. *Ferroelectrics* **129**, 101-112 (1992).

9 Scott, J. F. Room-temperature multiferroic magnetoelectrics. *NPG Asia Materials*

5, e72, doi:10.1038/am.2013.58 (2013).

10 Srinivas, A., Suryanarayana, S., Kumar, G. & Kumar, M. M. Magnetoelectric measurements on $Bi_5FeTi_3O_{15}$ and $Bi_6Fe_2Ti_3O_{18}$. *Journal of Physics: Condensed Matter* **11**, 3335 (1999).

11 Mao, X., Wang, W., Chen, X. & Lu, Y. Multiferroic properties of layer-structured $Bi_5Fe_{0.5}Co_{0.5}Ti_3O_{15}$ ceramics. *Applied Physics Letters* **95**, 082901, doi:10.1063/1.3213344 (2009).

12 Keeney, L., Maity, T., Schmidt, M., Amann, A., Deepak, N., Petkov, N., Roy, S., Pemble, M. E., Whatmore, R. W. & Johnson, D. Magnetic Field-Induced Ferroelectric Switching in Multiferroic Aurivillius Phase Thin Films at Room Temperature. *Journal of the American Ceramic Society* **96**, 2339-2357, doi:10.1111/jace.12467 (2013).

13 Jiang, Q., Liu, F., Yan, H., Ning, H., Libor, Z., Zhang, Q., Cain, M., Reece, M. J. & Nan, C. W. Magneto-Electric Properties of Multiferroic $Pb(Zr_{0.52}Ti_{0.48})O_3$-$NiFe_2O_4$ Nanoceramic Composites. *Journal of the American Ceramic Society* **94**, 2311-2314, doi:10.1111/j.1551-2916.2011.04665.x (2011).

14 Shen, Z., Liu, J., Grins, J., Nygren, M., Wang, P., Kan, Y., Yan, H. & Sutter, U. Effective Grain Alignment in $Bi_4Ti_3O_{12}$ Ceramics by Superplastic‐Deformation‐Induced Directional Dynamic Ripening. *Advanced Materials* **17**, 676-680 (2005).

15 Rabe, K. M., Dawber, M., Lichtensteiger, C., Ahn, C. H. & Triscone, J.-M. *Modern Physics of Ferroelectrics: essential background*. (Springer, 2007).

16 Zheludev, I. Ferroelectricity and symmetry. *Solid State Physics* **26**, 429-464 (1971).

17 Fesenko, E., Gavrilyatchenko, V. & Semenchev, A. Domain structure of multiaxial ferroelectric crystals. *Ferroelectrics* **100**, 195-207 (1989).

18 Lines, M. E. & Glass, A. M. *Principles and applications of ferroelectrics and related materials*. (Oxford university press, 1977).

19 Damjanovic, D., Muralt, P. & Setter, N. Ferroelectric sensors. *IEEE Sensors Journal* **1**, 191-206 (2001).

20 De Araujo, C.-P., Cuchiaro, J., McMillan, L., Scott, M. & Scott, J. Fatigue-free ferroelectric capacitors with platinum electrodes. *Nature* **374**, 627-629 (1995).

21 Lee, H. N., Hesse, D., Zakharov, N. & Gösele, U. Ferroelectric $Bi_{3.25}La_{0.75}Ti_3O_{12}$ films of uniform a-axis orientation on silicon substrates. *Science* **296**, 2006-2009 (2002).

22 Damjanovic, D. Ferroelectric, dielectric and piezoelectric properties of ferroelectric thin films and ceramics. *Reports on Progress in Physics* **61**, 1267 (1998).

23 Fu, D. & Itoh, M. Role of Ca off-centering in tuning the ferroelectric phase transitions in $Ba(Zr,Ti)O_3$ system. *arXiv preprint arXiv:1503.00406* (2015).

24 Jia, C.-L., Urban, K. W., Alexe, M., Hesse, D. & Vrejoiu, I. Direct observation of continuous electric dipole rotation in flux-closure domains in ferroelectric $Pb(Zr, Ti)O_3$. *Science* **331**, 1420-1423 (2011).

25 Callister, W. D. & Rethwisch, D. G. *Materials Science and Engineering: an*

introduction. Vol. 7 (Wiley New York, 2007).

26 Smit, J. *Magnetic Properties of Materials*. Vol. 13 (McGraw-Hill, 1971).

27 Coey, J. M. *Magnetism and Magnetic Materials*. (Cambridge University Press, 2010).

28 Li, Y.-Y. Superexchange interactions and magnetic lattices of the rhombohedral sesquioxides of the transition elements and their solid solutions. *Physical Review* **102**, 1015 (1956).

29 Goodenough, J. B. Theory of the Role of Covalence in the Perovskite-Type Manganites [La,M(II)]MnO_3. *Physical Review* **100**, 564 (1955).

30 Kanamori, J. Superexchange interaction and symmetry properties of electron orbitals. *Journal of Physics and Chemistry of Solids* **10**, 87-98 (1959).

31 戴道生 & 钱昆明. *铁磁学: 上册*. 科学出版社, (1987). Daosheng, D and Kunmin, Q. Theory of Ferroelectrics. Science Press, (1987).

32 Zener, C. Interaction between the d-shells in the transition metals. II. Ferromagnetic compounds of manganese with perovskite structure. *Physical Review* **82**, 403 (1951).

33 Spaldin, N. A. & Fiebig, M. The renaissance of magnetoelectric multiferroics. *Science* **309**, 391-392 (2005).

34 Khomskii, D. Trend: Classifying multiferroics: Mechanisms and effects. *Physics* **2**, 20 (2009).

35 Dang, N., Nguyen, H. M., Chuang, P.-Y., Zhang, J.-H., Thanh, T., Hu, C.-W., Chen, T.-Y., Yang, H.-D., Lam, V. & Lee, C.-H. Structure and magnetism of

$BaTi_{1-x}Fe_xO_{3-\delta}$ multiferroics. *Journal of Applied Physics* **111**, 07D915 (2012).

36 Nomura, S., Takabayashi, H. & Nakagawa, T. Dielectric and magnetic properties of $Pb(Fe_{1/2}Ta_{1/2})\ O_3$. *Japanese Journal of Applied Physics* **7**, 600 (1968).

37 Uchino, K. & Nomura, S. Dielectric and magnetic properties in the solid solution system $Pb(Fe_{2/3}W_{1/3})O_3$-$Pb(Co_{1/2}W_{1/2})O_3$. *Ferroelectrics* **17**, 505-510 (1977).

38 Henson, R., Zeyfang, R. & Linhart, E. Pyroelectric properties of Pb(Ti, Zr,$[Fe_{1/2}Ta_{1/2}]$)O_3 polycrystalline solid solutions. *Physica Status Solidi (a)* **46**, 511-515 (1978).

39 Uchino, K. & Nomura, S. Crystallographic and dielectric properties in the solid solution systems $Pb(Fe_{2/3}W_{1/3})O_3$-$Pb(Mg_{1/3}Ta_{2/3})O_3$ and $Pb(MgW)_{1/2}O_3$-Pb $(FeTa)_{1/2}O_3$. *Journal of the Physical Society of Japan* **41**, 542-547 (1976).

40 Kumar, A., Katiyar, R. & Scott, J. Fabrication and characterization of the multiferroic birelaxor lead–iron–tungstate/lead–zirconate–titanate. *J. Appl. Phys* **108**, 064105 (2010).

41 Evans, D., Schilling, A., Kumar, A., Sanchez, D., Ortega, N., Arredondo, M., Katiyar, R., Gregg, J. & Scott, J. Magnetic switching of ferroelectric domains at room temperature in multiferroic PZTFT. *Nature Communications* **4**, 1534 (2013).

42 Sanchez, D. A., Kumar, A., Ortega, N., Katiyar, R. & Scott, J. Near-room temperature relaxor multiferroic. *Applied Physics Letters* **97**, 202910 (2010).

43 Oka, K., Azuma, M., Hirai, S., Belik, A. A., Kojitani, H., Akaogi, M., Takano, M. & Shimakawa, Y. Pressure-Induced transformation of 6H hexagonal to 3C

perovskite structure in PbMnO3. *Inorganic Chemistry* **48**, 2285-2288 (2009).

44 Tsuchiya, T., Saito, H., Yoshida, M., Katsumata, T., Ohba, T., Inaguma, Y., Tsurui, T. & Shikano, M. in *MRS Proceedings.* 0988-QQ0909-0916 (Cambridge Univ Press).

45 Kimura, T., Kawamoto, S., Yamada, I., Azuma, M., Takano, M. & Tokura, Y. Magnetocapacitance effect in multiferroic $BiMnO_3$. *Physical Review B* **67**, 180401 (2003).

46 Kumar, M. M., Palkar, V., Srinivas, K. & Suryanarayana, S. Ferroelectricity in a pure $BiFeO_3$ ceramic. *Applied Physics Letters* **76**, 2764-2766 (2000).

47 Catalan, G. & Scott, J. F. Physics and applications of bismuth ferrite. *Advanced Materials* **21**, 2463-2485 (2009).

48 Lebeugle, D., Colson, D., Forget, A. & Viret, M. Very large spontaneous electric polarization in $BiFeO_3$ single crystals at room temperature and its evolution under cycling fields. *Applied Physics Letters* **91**, 022907 (2007).

49 Lebeugle, D., Colson, D., Forget, A., Viret, M., Bataille, A. & Gukasov, A. Electric-field-induced spin flop in $BiFeO_3$ single crystals at room temperature. *Physical Review Letters* **100**, 227602 (2008).

50 Henrichs, L. F., Cespedes, O., Bennett, J., Landers, J., Salamon, S., Heuser, C., Hansen, T., Helbig, T., Gutfleisch, O., Lupascu, D. C., Wende, H., Kleemann, W. & Bell, A. J. Multiferroic Clusters: A New Perspective for Relaxor-Type Room-Temperature Multiferroics. *Advanced Functional Materials*, n/a-n/a, doi:10.1002/adfm.201503335 (2016).

51 Van Aken, B. B., Palstra, T. T., Filippetti, A. & Spaldin, N. A. The origin of ferroelectricity in magnetoelectric $YMnO_3$. *Nature Materials* **3**, 164-170 (2004).

52 Fennie, C. J. & Rabe, K. M. Ferroelectric transition in $YMnO_3$ from first principles. *Physical Review B* **72**, 100103 (2005).

53 Lee, S., Pirogov, A., Kang, M., Jang, K.-H., Yonemura, M., Kamiyama, T., Cheong, S.-W., Gozzo, F., Shin, N. & Kimura, H. Giant magneto-elastic coupling in multiferroic hexagonal manganites. *Nature* **451**, 805-808 (2008).

54 Benedek, N. A. & Fennie, C. J. Hybrid improper ferroelectricity: a mechanism for controllable polarization-magnetization coupling. *Physical Review Letters* **106**, 107204 (2011).

55 Lawes, G. Viewpoint: Twisting and turning towards new multiferroics. *Physics* **4**, 18 (2011).

56 Yamauchi, K., Fukushima, T. & Picozzi, S. Ferroelectricity in multiferroic magnetite Fe_3O_4 driven by noncentrosymmetric Fe^{2+}/Fe^{3+} charge-ordering: first-principles study. *Physical Review B* **79**, 212404 (2009).

57 Efremov, D. V., Van Den Brink, J. & Khomskii, D. I. Bond-versus site-centred ordering and possible ferroelectricity in manganites. *Nature Materials* **3**, 853-856 (2004).

58 Ederer, C. & Spaldin, N. A. Magnetoelectrics: A new route to magnetic ferroelectrics. *Nature Materials* **3**, 849-851 (2004).

59 Giovannetti, G., Kumar, S., Khomskii, D., Picozzi, S. & van den Brink, J. Multiferroicity in Rare-Earth Nickelates $RNiO_3$. *Physical Review Letters* **103**,

156401 (2009).

60 Giovannetti, G., Kumar, S., van den Brink, J. & Picozzi, S. Magnetically induced electronic ferroelectricity in half-doped manganites. *Physical Review Letters* **103**, 037601 (2009).

61 Lopes, A., Araújo, J., Amaral, V., Correia, J., Tomioka, Y. & Tokura, Y. New phase transition in the $Pr_{1-x}Ca_xMnO_3$ system: evidence for electrical polarization in charge ordered manganites. *Physical Review Letters* **100**, 155702 (2008).

62 Ko, K.-T., Noh, H.-J., Kim, J.-Y., Park, B.-G., Park, J.-H., Tanaka, A., Kim, S., Zhang, C. & Cheong, S. Electronic origin of giant magnetic anisotropy in multiferroic $LuFe_2O_4$. *Physical Review Letters* **103**, 207202 (2009).

63 Choi, Y., Yi, H., Lee, S., Huang, Q., Kiryukhin, V. & Cheong, S.-W. Ferroelectricity in an Ising chain magnet. *Physical Review Letters* **100**, 047601 (2008).

64 Senff, D., Aliouane, N., Argyriou, D., Hiess, A., Regnault, L., Link, P., Hradil, K., Sidis, Y. & Braden, M. Magnetic excitations in a cycloidal magnet: the magnon spectrum of multiferroic $TbMnO_3$. *Journal of Physics: Condensed Matter* **20**, 434212 (2008).

65 Kimura, T., Goto, T., Shintani, H., Ishizaka, K., Arima, T. & Tokura, Y. Magnetic control of ferroelectric polarization. *Nature* **426**, 55-58 (2003).

66 Prokhnenko, O., Feyerherm, R., Dudzik, E., Landsgesell, S., Aliouane, N., Chapon, L. & Argyriou, D. Enhanced ferroelectric polarization by induced Dy spin order in multiferroic $DyMnO_3$. *Physical Review Letters* **98**, 057206 (2007).

67 Hur, N., Park, S., Sharma, P., Ahn, J., Guha, S. & Cheong, S. Electric polarization reversal and memory in a multiferroic material induced by magnetic fields. *Nature* **429**, 392-395 (2004).

68 Katsura, H., Nagaosa, N. & Balatsky, A. V. Spin current and magnetoelectric effect in noncollinear magnets. *Physical Review Letters* **95**, 057205 (2005).

69 Sergienko, I. A. & Dagotto, E. Role of the Dzyaloshinskii-Moriya interaction in multiferroic perovskites. *Physical Review B* **73**, 094434 (2006).

70 Cheong, S., Thompson, J. & Fisk, Z. Metamagnetism In La_2CuO_4. *Physical Review B* **39**, 4395 (1989).

71 Cheong, S.-W. & Mostovoy, M. Multiferroics: a magnetic twist for ferroelectricity. *Nature Materials* **6**, 13-20 (2007).

72 Yan, H., Zhang, H., Reece, M. J. & Dong, X. Thermal depoling of high Curie point Aurivillius phase ferroelectric ceramics. *Applied Physics Letters* **87**, 2911 (2005).

73 Kasap, S. & Capper, P. *Springer handbook of electronic and photonic materials*. (Springer Science & Business Media, 2006).

74 Machado, R., Stachiotti, M., Migoni, R. & Tera, A. H. First-principles determination of ferroelectric instabilities in Aurivillius compounds. *Physical Review B* **70**, 214112 (2004).

75 Frit, B. & Mercurio, J. The crystal chemistry and dielectric properties of the Aurivillius family of complex bismuth oxides with perovskite-like layered structures. *Journal of Alloys and Compounds* **188**, 27-35 (1992).

76 Suárez, D. Y., Reaney, I. M. & Lee, W. E. Relation between tolerance factor and T c in Aurivillius compounds. *Journal of Materials Research* **16**, 3139-3149 (2001).

77 Reaney, I., Roulin, M., Shulman, H. & Setter, N. In situ observations of octahedral tilt transitions in strontium bismuth titanate layered perovskites. *Ferroelectrics* **165**, 295-305 (1995).

78 Rae, A. D., Thompson, J. G., Withers, R. & Willis, A. C. Structure refinement of commensurately modulated bismuth titanate, $Bi_4Ti_3O_{12}$. *Acta Crystallographica Section B: Structural Science* **46**, 474-487 (1990).

79 Withers, R., Thompson, J. & Rae, A. The crystal chemistry underlying ferroelectricity in $Bi_4Ti_3O_{12}$, Bi_3TiNbO_9, and Bi_2WO_6. *Journal of Solid State Chemistry* **94**, 404-417 (1991).

80 Amanuma, K., Hase, T. & Miyasaka, Y. Preparation and ferroelectric properties of $SrBi_2Ta_2O_9$ thin films. *Applied Physics Letters* **66**, 221-223 (1995).

81 Shimakawa, Y., Kubo, Y., Nakagawa, Y., Kamiyama, T., Asano, H. & Izumi, F. Crystal structures and ferroelectric properties of $SrBi_2Ta_2O_9$ and $Sr_{0.8}Bi_{2.2}Ta_2O_9$. *Applied Physics Letters* **74**, 1904 (1999).

82 Irie, H., Miyayama, M. & Kudo, T. Structure dependence of ferroelectric properties of bismuth layer-structured ferroelectric single crystals. *Journal of Applied Physics* **90**, 4089-4094 (2001).

83 Withers, R., Thompson, J. & Rae, A. The crystal chemistry underlying ferroelectricity in $Bi_4Ti_3O_{12}$, Bi_3TiNbO_9, and Bi_2WO_6. *Journal of Solid State Chemistry* **94**, 404-417 (1991).

84 Yan, H., Zhang, H., Ubic, R., Reece, M. J., Liu, J., Shen, Z. & Zhang, Z. A Lead‐Free High‐Curie‐Point Ferroelectric Ceramic, $CaBi_2Nb_2O_9$. *Advanced Materials* **17**, 1261-1265 (2005).

85 Yan, H., Zhang, H., Zhang, Z., Ubic, R. & Reece, M. J. B-site donor and acceptor doped Aurivillius phase Bi_3NbTiO_9 ceramics. *Journal of the European Ceramic Society* **26**, 2785-2792 (2006).

86 Yan, H., Zhang, H., Ubic, R., Reece, M., Liu, J. & Shen, Z. Orientation dependence of dielectric and relaxor behaviour in Aurivillius phase $BaBi_2Nb_2O_9$ ceramics prepared by spark plasma sintering. *Journal of Materials Science: Materials in Electronics* **17**, 657-661, doi:10.1007/s10854-006-0017-0 (2006).

87 Subbarao, E. A family of ferroelectric bismuth compounds. *Journal of Physics and Chemistry of Solids* **23**, 665-676 (1962).

88 Ding, Y., Liu, J. & Wang, Y. Transmission electron microscopy study on ferroelectric domain structure in $SrBi_2Ta_2O_9$ ceramics. *Applied Physics Letters* **76**, 103-105 (2000).

89 Cummins, S. & Cross, L. Electrical and optical properties of ferroelectric $Bi_4Ti_3O_{12}$ single crystals. *Journal of Applied Physics* **39**, 2268-2274 (1968).

90 Katayama, S., Noguchi, Y. & Miyayama, M. 3D domain structure in $Bi_4Ti_3O_{12}$ crystals observed by using piezoresponse force microscopy. *Advanced Materials* **19**, 2552-2555 (2007).

91 Akbas, M. A. & Davies, P. K. Domain growth in $Pb(Mg_{1/3}Ta_{2/3})O_3$ perovskite relaxor ferroelectric oxides. *Journal of the American Ceramic Society* **80**,

2933-2936 (1997).

92 Cross, L. E. Relaxorferroelectrics: an overview. *Ferroelectrics* **151**, 305-320 (1994).

93 Cross, L. E. Relaxor ferroelectrics. *Ferroelectrics* **76**, 241-267 (1987).

94 Smolenskii, G., Isupov, V. & Agranovskaya, A. Ferroelectrics of the oxygen-octahedral type with layered structure. *Soviet Physics-Solid State* **3**, 651-655 (1961).

95 Blake, S. M., Falconer, M. J., McCreedy, M. & Lightfoot, P. Cation disorder in ferroelectric Aurivillius phases of the type $Bi_2ANb_2O_9$ (A= Ba, Sr, Ca). *Journal of Materials Chemistry* **7**, 1609-1613 (1997).

96 Hunter, B. A. & Kennedy, B. J. Cation disorder in the ferroelectric Aurivillius phase $PbBi_2Nb_2O_9$: an anamolous dispersion X-ray diffraction study. *Solid State Ionics* **112**, 281-289 (1998).

97 Miranda, C., Costa, M., Avdeev, M., Kholkin, A. & Baptista, J. Relaxor properties of Ba-based layered perovskites. *Journal of the European Ceramic Society* **21**, 1303-1306 (2001).

98 Kim, S.-K., Miyayama, M. & Yanagida, H. Electrical anisotropy of $BaBi_4Ti_4O_{15}$ single crystal. *Nippon Seramikkusu Kyokai Gakujutsu Ronbunshi* **102**, 722-726 (1994).

99 Irie, H., Miyayama, M. & Kudo, T. Electrical Properties of a Bismuth Layer - Structured $Ba_2Bi_4Ti_5O_{18}$ Single Crystal. *Journal of the American Ceramic Society* **83**, 2699-2704 (2000).

100 Liu, J., Shen, Z., Yan, H., Reece, M. J., Kan, Y. & Wang, P. Dielectric, piezoelectric, and ferroelectric properties of grain-orientated $Bi_{3.25}La_{0.75}Ti_3O_{12}$ ceramics. *Journal of Applied Physics* **102**, 104107, doi:10.1063/1.2812697 (2007).

101 IG, I., VI, N., Mirishli, F. & Rustamov, P. X-ray and electrical studies of system $Bi_4Ti_3O_{12}$-$BiFeO_3$. *Soviet Physics Crystallography, USSR* **12**, 400-& (1967).

102 Singh, R. *Structure–property correlations in some magnetically ordered Aurivillius phases*, Ph. D. Thesis, Osmania University, Hyderabad, (1996).

103 Mao, X., Sun, H., Wang, W., Chen, X. & Lu, Y. Ferromagnetic, ferroelectric properties, and magneto-dielectric effect of $Bi_{4.25}La_{0.75}Fe_{0.5}Co_{0.5}Ti_3O_{15}$ ceramics. *Applied Physics Letters* **102**, 072904, doi:10.1063/1.4793305 (2013).

104 Liu, J., Bai, W., Yang, J., Xu, W., Zhang, Y., Lin, T., Meng, X., Duan, C.-G., Tang, X. & Chu, J. The Cr-substitution concentration dependence of the structural, electric and magnetic behaviors for Aurivillius $Bi_5Ti_3FeO_{15}$ multiferroic ceramics. *Journal of Applied Physics* **114**, 234101 (2013).

105 Keeney, L., Groh, C., Kulkarni, S., Roy, S., Pemble, M. E. & Whatmore, R. W. Room temperature electromechanical and magnetic investigations of ferroelectric Aurivillius phase $Bi_5Ti_3(Fe_xMn_{1-x})O_{15}$ (x= 1 and 0.7) chemical solution deposited thin films. *Journal of Applied Physics* **112**, 024101 (2012).

106 Liu, Z., Yang, J., Tang, X., Yin, L., Zhu, X., Dai, J. & Sun, Y. Multiferroic properties of Aurivillius phase $Bi_6Fe_{2-x}Co_xTi_3O_{18}$ thin films prepared by a chemical solution deposition route. *Applied Physics Letters* **101** (2012).

107 Palizdar, M., Comyn, T. P., Ward, M. B., Brown, A. P., Harrington, J. P., Kulkarni, S., Keeney, L., Roy, S., Pemble, M., Whatmore, R., Quinn, C., Kilcoyne, S. H. & Bell, A. J. Crystallographic and magnetic identification of secondary phase in orientated $Bi_5Fe_{0.5}Co_{0.5}Ti_3O_{15}$ ceramics. *Journal of Applied Physics* **112**, 073919, doi:10.1063/1.4754562 (2012).

108 Toby, B. H. EXPGUI, a graphical user interface for GSAS. *Journal of Applied Crystallography* **34**, 210-213 (2001).

109 Dollase, W. Correction of intensities for preferred orientation in powder diffractometry: application of the March model. *Journal of Applied Crystallography* **19**, 267-272 (1986).

110 German, R. *Sintering: from empirical observations to scientific principles*. (Butterworth-Heinemann, 2014).

111 Clarke, J. SQUIDs. *Scientific American* **271**, 46-53 (1994).

112 Gelfuso, M. V., Thomazini, D. & Eiras, J. A. Synthesis and structural, ferroelectric, and piezoelectric properties of $SrBi_4Ti_4O_{15}$ ceramics. *Journal of the American Ceramic Society* **82**, 2368-2372 (1999).

113 Shulman, H. S., Testorf, M., Damjanovic, D. & Setter, N. Microstructure, electrical conductivity, and piezoelectric properties of bismuth titanate. *Journal of the American Ceramic Society* **79**, 3124-3128 (1996).

114 Viola, G., Saunders, T., Wei, X., Chong, K. B., Luo, H., Reece, M. J. & Yan, H. Contribution of piezoelectric effect, electrostriction and ferroelectric/ferroelastic switching to strain-electric field response of dielectrics. *Journal of Advanced*

Dielectrics **03**, 1350007, doi:10.1142/s2010135x13500070 (2013).

115 Ang, C., Yu, Z. & Cross, L. Oxygen-vacancy-related low-frequency dielectric relaxation and electrical conduction in Bi:$SrTiO_3$. *Physical Review B* **62**, 228 (2000).

116 Roy, A., Gupta, R. & Garg, A. Multiferroic Memories. *Advances in Condensed Matter Physics* **2012**, 1-12, doi:10.1155/2012/926290 (2012).

117 Takashima, D. & Kunishima, I. High-density chain ferroelectric random access memory (chain FRAM). *Solid-State Circuits, IEEE Journal of* **33**, 787-792 (1998).

118 Pyatakov, A. P. & Zvezdin, A. K. Magnetoelectric and multiferroic media. *Physics-Uspekhi* **55**, 557-581 (2012).

119 Kimura, T., Sekio, Y., Nakamura, H., Siegrist, T. & Ramirez, A. Cupric oxide as an induced-multiferroic with high-TC. *Nature Materials* **7**, 291-294 (2008).

120 Wu, H., Burnus, T., Hu, Z., Martin, C., Maignan, A., Cezar, J., Tanaka, A., Brookes, N., Khomskii, D. & Tjeng, L. Ising Magnetism and Ferroelectricity in Ca_3CoMnO_6. *Physical Review Letters* **102**, 026404 (2009).

121 Spaldin, N. A., Cheong, S.-W. & Ramesh, R. Multiferroics: Past, present, and future. *Physics Today* **63**, 38-43, doi:10.1063/1.3502547 (2010).

122 Fiebig, M. Revival of the magnetoelectric effect. *Journal of Physics D: Applied Physics* **38**, R123 (2005).

123 Turner, R., Fuierer, P. A., Newnham, R. & Shrout, T. Materials for high temperature acoustic and vibration sensors: a review. *Applied Acoustics* **41**,

299-324 (1994).

124 Newnham, R., Wolfe, R. & Dorrian, J. Structural basis of ferroelectricity in the bismuth titanate family. *Materials Research Bulletin* **6**, 1029-1039 (1971).

125 Viola, G., Boon Chong, K., Eriksson, M., Shen, Z., Zeng, J., Yin, Q., Kan, Y., Wang, P., Ning, H., Zhang, H., Fitzpatrick, M. E., Reece, M. J. & Yan, H. Effect of grain size on domain structures, dielectric and thermal depoling of Nd-substituted bismuth titanate ceramics. *Applied Physics Letters* **103**, 182903, doi:10.1063/1.4827537 (2013).

126 Chon, U., Jang, H. M., Kim, M. & Chang, C. Layered perovskites with giant spontaneous polarizations for nonvolatile memories. *Physical Review Letters* **89**, 087601 (2002).

127 Mahesh Kumar, M., Srinivas, A., Suryanarayana, S., Kumar, G. & Bhimasankaram, T. An experimental setup for dynamic measurement of magnetoelectric effect. *Bulletin of Materials Science* **21**, 251-255 (1998).

128 Yan, H., Inam, F., Viola, G., Ning, H., Zhang, H., Jiang, Q., Zeng, T. A. O., Gao, Z. & Reece, M. J. The contribution of electrical conductivity, dielectric permittivity and domain switching in ferroelectric hysteresis loops. *Journal of Advanced Dielectrics* **01**, 107-118, doi:10.1142/s2010135x11000148 (2011).

129 Abrahams, S. & Keve, E. Structural basis of ferroelectricity and ferroelastcity. *Ferroelectrics* **2**, 129-154 (1971).

130 Joshi, P. C. & Desu, S. B. Structural and electrical characteristics of rapid thermally processed ferroelectric $Bi_4Ti_3O_{12}$ thin films prepared by metalorganic

solution deposition technique. *Journal of Applied Physics* **80**, 2349, doi:10.1063/1.363069 (1996).

131 Singh, R., Bhimasankaram, T., Kumar, G. & Suryanarayana, S. Dielectric and magnetoelectric properties of $Bi_5FeTi_3O_{15}$. *Solid State Communications* **91**, 567-569 (1994).

132 Shen, Z., Peng, H. & Nygren, M. Formidable increase in the superplasticity of ceramics in the presence of an electric field. *Advanced Materials* **15**, 1006-1009 (2003).

133 Ji, G., Lin, X., Sun, Y., Ali Trimizi, S. A., Su, H. & Du, Y. Molten salt growth and magnetic properties of octahedral $CoFe_2O_4$ crystals: effects of synthesis conditions. *CrystEngComm* **13**, 6451, doi:10.1039/c1ce05459g (2011).

134 Sun, S., Huang, Y., Wang, G., Wang, J., Fu, Z., Peng, R., Knize, R. J. & Lu, Y. Nanoscale structural modulation and enhanced room-temperature multiferroic properties. *Nanoscale* **6**, 13494-13500, doi:10.1039/c4nr03542a (2014).

135 Li, J. B., Huang, Y. P., Rao, G. H., Liu, G. Y., Luo, J., Chen, J. R. & Liang, J. K. Ferroelectric transition of Aurivillius compounds $Bi_5Ti_3FeO_{15}$ and $Bi_6Ti_3Fe_2O_{18}$. *Applied Physics Letters* **96**, 222903, doi:10.1063/1.3447372 (2010).

136 Franco, A. & e Silva, F. C. High temperature magnetic properties of cobalt ferrite nanoparticles. *Applied Physics Letters* **96**, 172505, doi:10.1063/1.3422478 (2010).

137 Tsymbal, E. Y. & Zutic, I. *Handbook of Spin Transport and Magnetism*. (CRC press, 2011).

138 Kawano, S., Achiwa, N., Yamamoto, N. & Higashi, S.-n. Metal-ion distribution and magnetic structure of Fe-substituted cobaltite spinel: $FeCo_2O_4$. *Materials Research Bulletin* **11**, 911-916 (1976).

139 Muthuselvam, I. P. & Bhowmik, R. N. Structural phase stability and magnetism in Co_2FeO_4 spinel oxide. *Solid State Sciences* **11**, 719-725, doi:10.1016/j.solidstatesciences.2008.10.012 (2009).

140 Monz, S., Tschope, A. & Birringer, R. Magnetic properties of isotropic and anisotropic $CoFe_2O_4$-based ferrogels and their application as torsional and rotational actuators. *Physical review. E, Statistical, nonlinear, and soft matter physics* **78**, 021404, doi:10.1103/PhysRevE.78.021404 (2008).

141 Birenbaum, A. Y. & Ederer, C. Potentially multiferroic Aurivillius phase $Bi_5FeTi_3O_{15}$: Cation site preference, electric polarization, and magnetic coupling from first principles. *Physical Review B* **90**, doi:10.1103/PhysRevB.90.214109 (2014).

142 Yang, J., Yin, L., Liu, Z., Zhu, X., Song, W., Dai, J., Yang, Z. & Sun, Y. Magnetic and dielectric properties of Aurivillius phase $Bi_6Fe_2Ti_3O_{18}$ and the doped compounds. *Applied Physics Letters* **101**, 012402 (2012).

143 Zuo, X., Yang, J., Song, D., Yuan, B., Tang, X., Zhang, K., Zhu, X., Song, W., Dai, J. & Sun, Y. Magnetic, dielectric, and magneto-dielectric properties of rare-earth-substituted Aurivillius phase $Bi_6Fe_{1.4}Co_{0.6}Ti_3O_{18}$. *Journal of Applied Physics* **116**, 154102 (2014).

144 Xiang-Yu, M., Bao-Wen, Z., Hui, S., Chun-Yan, C. & Xiao-Bing, C. Effects of

Co-doping on multiferroic properties of $Bi_6Fe_{2-x}Co_xTi_3O_{18}$ ceramics. *Acta Physica Sinica* **64** (2015).